

Micro and Nanostructures of Au and Ag: Unusual Morphologies, Crystal Structures and Properties

A thesis

Submitted for the degree of

Doctor of Philosophy

by

Gangaiah Mettela



**Chemistry and Physics of Materials Unit
JAWAHARLAL NEHRU CENTRE FOR ADVANCED
SCIENTIFIC RESEARCH
(A Deemed University)
BANGALORE, INDIA
July 2015**

DECLARATION

I hereby declare that the thesis entitled “*Micro and Nanostructures of Au and Ag: Unusual Morphologies, Crystal Structures and Properties*” is an authentic record of research work carried out by me at the Chemistry and Physics of Materials Unit, Jawaharlal Nehru Centre for Advanced Scientific Research, Bangalore, India under the supervision of *Professor G. U. Kulkarni* and that it has not been submitted elsewhere for the award of any degree or diploma.

In keeping with the general practice in reporting scientific observations, due acknowledgment has been made whenever the work described is based on the findings of other investigators. Any omission that might have occurred due to oversight or error in judgment is regretted.

(Gangaiah Mettela)

CERTIFICATE

Certified that the work described in this thesis titled “*Micro and Nanostructures of Au and Ag: Unusual Morphologies, Crystal Structures and Properties*” has been carried out by Mr. Gangaiah Mettela at the Chemistry and Physics of Materials Unit, Jawaharlal Nehru Centre for Advanced Scientific Research, Bangalore, India under my supervision and that it has not been submitted elsewhere for the award of any degree or diploma.

Professor G. U. Kulkarni
(Research Supervisor)

Acknowledgements

I express my deep sense of gratitude to **Professor G. U. Kulkarni**, for being my research supervisor and guiding me in a right direction to approach and solve scientific problems. I am very grateful to him for suggesting such an interesting project and rejuvenating me with new explorations. His vision of science and problem solving approach is very inspiring. His simple way of thinking and reasoning is astounding. Imagining myself in his shoes, I wonder how he deals with such multi disciplinary fields of physics and chemistry. He always remains as a reference to me in choosing a research problem in the upcoming field to remain as a forefront researcher.

Professor C. N. R. Rao is a great source of inspiration and encouragement to me. I learned more about him through my research supervisor, who himself is a great disciple of him. My mentor used to take his example, saying how different as an individual he is to be so great and used to motivate us in doing a better science. His scientific lectures are appealing and encouraging to young scientists.

It is a pleasure to thank all my collaborators; Prof. Umesh Waghmare, Prof. Chandrabhas, Dr. Pavan Kumar, Dr. Radha, Dr. Ritu, Dr. Soumik, Mr. Danveer Singh and Ms. Meha

I thank all the faculty members of CPMU and NCU for their cordiality, especially my teachers, Professor. N. Chandrabhas, Umesh Waghmare, Sundaresan, Eswaramoorthy, S. M. Shivaprasad, Drs. Subi, Govindraju, T. K. Maji and Prof. Guru Row (IISc) for their courses.

I thank Mrs. Indira Kulkarni, Teju and poorna for their warmth and hospitality.

I am grateful to my labmates, Dr. Radha, Dr. Narendra, Dr. Abhay, Dr. Ritu, Dr. Rashmi, Dr. Padma, Dr. Harish, Dr. Murali, Dr. Shubra, Dr. Mallik, Mogera, Kiruthika, Ankush, Dipa, Sunil, Chaitali, Karthik, Bharath, Rajashekhar, Tripura, Nikita, Suman, Govindan, Guratinder, Tripti, Aman and Abijit for their support and friendly nature.

Timely and ready assistance and also friendly attitude from technical staff, Mr. Srinath and Mr. Srinivas is acknowledged. I am very thankful to Mrs. Usha and Dr. Joy (TEM), Selvi (FESEM), Suma (Confocal microscopy), Dr. Basavaraj (AFM), Mr. Anil (XRD), Mr.

Mahesh (SEM), Mr. Kishore (XPS), Dr. Karthik (FIB), Mr. Vasu (UV) and Mr. A. Srinivasa Rao for their invaluable technical assistance. Ms. Vanitha and Mr. Sunil for their help in various lab activities.

It is a pleasure to thank Mrs. Indira Kulkarni, Teju and Poorna for their hospitality.

I thank Mrs. Aruna and Krithi Waghmare for their assistance in various cultural activities.

I thank Drs. Leela Srinivas, Dr. Neenu Vargheese, Dr. Rakesh, Dr. Srinu Bhadram, Dr. Subramanyam and Dr. Gopal for Raman measurements.

I thank Prof. Sampath, Prof. A.K. Shukla, Dr. Sridhar, Dr. Ranjan Datta, Dr. Sundraiah, Dr. Partho, Dr. Gayatri, Dr. Soumik, Dr. Dhanya and Rajaji for their useful discussion

I thank all my friends at JNCASR and IISc for their friendly nature.

I thank Dr. KKR Datta and Mrs. Datta for their hospitality and encouragement.

I thank the staff of academic and administrative section in JNC for their assistance, especially Dr. Princy and Mrs. Sukanya for their advices and friendly nature. I also thank the library staff for their help. I am thankful to the computer lab staff and purchase office staff.

I thank CSIR for financial assistance and DST for providing facilities.

I thank my M.Sc friends Sirisha, Arjun, Chandrababu naidu, Annapoorna, Kishore, Kalyan, Lakshmi, Venky, Giri, Srikanth, Subbu, Venkateswarlu, Manjula, Ramky, Tyson and Jaggu for making my M.Sc days memorable.

All this effort becomes futile without acknowledging my beloved parents, sister and my friends Srikanth, Anusha and Rama Lakshmi, at the same it is impossible to express my gratitude to them without whose support and wish, I would have not come thus far. They are always ready to share my grief and joy and encourage me to do better than the best.

Preface

The thesis work pertains to synthesis and characterization of Au and Ag microcrystallites exhibiting interesting crystal structures and optical properties. It is structured into seven chapters.

Chapter 1 introduces the concept of nanomaterials, their important properties and various synthetic routes. **Chapter 2** describes various tools that have been used for characterization. The thesis work relies on metal organic complexes as single source precursors obtained by phase transferring Au and Ag anions from aqueous phase to the organic layer using tetraoctylammonium bromide (ToABr). The M-ToABr (M=Au, Ag and AuAg) produces metal crystallites by thermolysis. **Chapter 3** deals with new etchants for anisotropic etching of Au microcrystallites obtained by the thermolysis of AuToABr. Au being noble bearing isotropic cubic crystal structure, anisotropic or facet selective etching is a challenge. AgToABr and CuCl₂ are found to be suitable etchants for selective oxidation of Au{100} and Au{111} facets respectively. The selective etching is shown to generate increased roughness containing high index nanofacets of high surface energies. **Chapter 4** presents a simple route to probe the local reactivities of various sites, corners, edges and planar sites, of Au microcrystallites by exposing them to Cu deposition from electroless plating. Detailed aspects related to Cu island growth on various planar surfaces, its dependency on inter planar angle and the size of crystallite have been examined. It has been observed that rapid deposition takes place at sharp corners followed by broad corners, edges and planar surfaces which has been attributed to the differences in Au-Au bond lengths at various sites. **Chapter 5** deals with the synthesis of tapered pentagonal Au bipyramids by thermalizing in air a mixture of ToABr complexes of Au and Ag. Here Ag acts of shape directing agent while not alloying with the former. The bipyramidal corrugated microstructures have been shown to serve for nano-focusing of light and also as SERS substrates. **Chapter 6** presents unique route to synthesize Au bipyramids hosting unconventional crystal structures distinctly different from the well-known FCC. Au bipyramids synthesized at ~ 220 °C exhibit body centered tetragonal (BCT) and body centered orthorhombic (BCO) crystal structures. The non-FCC phases are stable for years at room temperature, and convert to FCC by annealing

to higher temperature. **Chapter 7** describes the synthesis of nanocrystalline micronsized Ag flower like structures from AgBr obtained by thermal decomposition of AgToABr. They support wavelength independent SERS activity due to the interconnected Ag nanocrystallites. Microflowers are shown to be reusable SERS substrates in microfluidic devices to monitor chemical reactions carried out with microliters quantities of reactants.

In the final pages (**Chapter 8**), the summary of the thesis and an outlook are provided.

* * *

Table of Contents

Declaration.....	iii
Certificate	v
Acknowledgments	vii - viii
Preface.....	ix - x
Table of contents	xi – xiii
Abbreviations	xiv

Chapter 1 - Introduction to Nanomaterials

1.1 About the length scale.....	1-2
1.2 Shape dependent properties.....	3-7
1.3 Synthesis of metal nanocrystallites.....	8-11
1.4 Shape of metal nanocrystallites.....	12-14
1.5 Strain in metal nanocrystallites.....	15-16
1.6 Nanostructured surfaces.....	17-18
1.7 Physical methods.....	18
1.8 Biological methods.....	19
1.9 Lithography.....	19-21
1.10 Advantages of microcrystallites over nano.....	21
References.....	22-24

Chapter 2 - Characterization techniques.....25-26

Chapter 3 - Facet Selective Etching of Au Microcrystallites

Summary.....	27
3.1 Introduction.....	27-31
3.2 Scope of the investigation.....	31

3.3 Experimental details.....	31-33
3.4 Results and discussion	
3.4.1 Etching of {100} facets	34-39
3.4.2 Etching of {111} facets	40-44
3.5 Conclusion.....	45
References.....	45-48

Chapter 4 - Site Selective Cu Deposition on Au Microcrystallites: Corners, Edges versus Planar Surfaces

Summary.....	49
4.1 Introduction.....	49-50
4.2 Scope of the investigation.....	50-51
4.3 Experimental details.....	51
4.4 Results and discussion.....	52-61
4.5 Conclusion.....	61
References.....	62-63

Chapter 5 - Highly tapered pentagonal bipyramidal Au microcrystals with high index faceted corrugation: Synthesis and optical properties

Summary.....	64
5.1 Introduction.....	65-66
5.2 Scope of the investigation.....	66
5.3 Experimental details.....	66-67
5.4 Results and discussion	
5.4.1 Characterization of AuAgToABr.....	67-68
5.4.2 Optimization of synthesis conditions.....	68-72
5.4.3 Structure of μ -CPB.....	73-76
5.4.4 Growth mechanism.....	77-81
5.4.5 SERS, pick and probe measurements.....	81-83
5.4.6 Light propagation.....	83-85
5.5 Conclusion.....	85-86

References.....	86-89
Chapter 6 - Ambient Stable Tetragonal and Orthorhombic Phases in Penta-Twinned Bipyramidal Au Microcrystals	
Summary.....	90
6.1 Introduction.....	90-93
6.2 Scope of the investigation.....	93
6.3 Results and discussion	
6.3.1 Stabilizing the non-FCC phases.....	93-100
6.3.2 TEM characterization.....	101-108
6.4 Conclusion.....	108
References.....	109-111
Chapter 7 - Nanocrystalline Ag microflowers as versatile SERS platform	
Summary.....	112
7.1 Introduction.....	112-114
7.2 Scope of the investigation.....	114
7.3 Experimental details.....	114-116
7.4 Results and discussion	
7.4.1 Characterization of AgToABr.....	116-117
7.4.2 Growth of Ag microflowers.....	117-121
7.4.3 Ag microflowers as SERS substrate.....	121-131
7.5 Conclusion.....	131-132
References.....	132-134
Chapter 8 – Summary and Outlook	135-136
Publications	137

Abbreviations

ToABr	-	Tetraoctylammonium bromide
FESEM	-	Field emission scanning electron microscopy
AFM	-	Atomic force microscopy
XRD	-	X-ray diffraction
EBL	-	Electron beam lithography
FESEM	-	Field emission scanning electron microscopy
FTIR	-	Fourier transform infrared spectroscopy
SAED	-	Selected area electron diffraction
TGA	-	Thermal gravimetric analysis
CTAB	-	Cetyltrimethylammonium bromide
HOMO	-	Highest occupied molecular orbital
LUMO	-	Lowest occupied molecular orbital
TEM	-	Transmission electron microscopy
SWNT	-	Single walled carbon nanotube
SPR	-	Surface plasmon resonance
CPS	-	Counts per second
DAC	-	Diamond anvil cell
ADXRD	-	Angle dispersive synchrotron XRD
HESXRD	-	High energy synchrotron XRD
PVP	-	Polyvinylpyrrolidone
PVA	-	Poly(vinyl alcohol)
SDS	-	Sodiumdodecylsulfate

About the length scale

In material science, size of the systems is an important parameter, and commonly used terms are nano, micro, meso and macro where the characteristic length is 10^{-9} , 10^{-6} , 10^{-4} and 10^{-2} meters respectively. In some sense, every macroscopic system is made of micro/nanosystems. In daily life, we come across many such examples. For instance, size of a butterfly is about 4 cm and the wings comprise of micron structures separated by a submicron gap, and each microstructure is made of nanostructures (Figs. 1.1a and b) (1). Similarly talcum powder, used in cosmetics is made of fine nanocrystallites (Figs. 1.1c and d) (2).

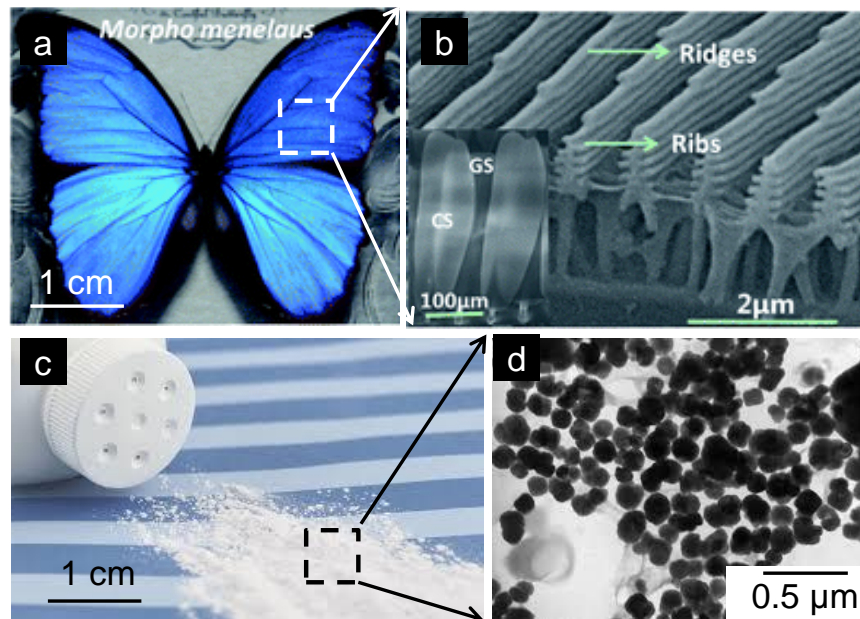


Figure 1.1 Micrographs of (a, b) butterfly and (c, d) talcum powder at different magnifications. (a and b) Reproduced with permission from ref (1).

Nanoparticles exhibit abnormal physical, chemical and magnetic properties due to their size confinement. For a nanomaterial, at least one of the dimensions has to be in nanometric regime and therefore, nanomaterials are classified as 0D, 1D and 2D depending on the number of degrees of freedom available for the bound electrons in the material. Example: Gold is generally

yellow in color, however gold nanoparticles due to size confinement exhibit pink/blue color depending on size (Fig. 1.2a) (3).

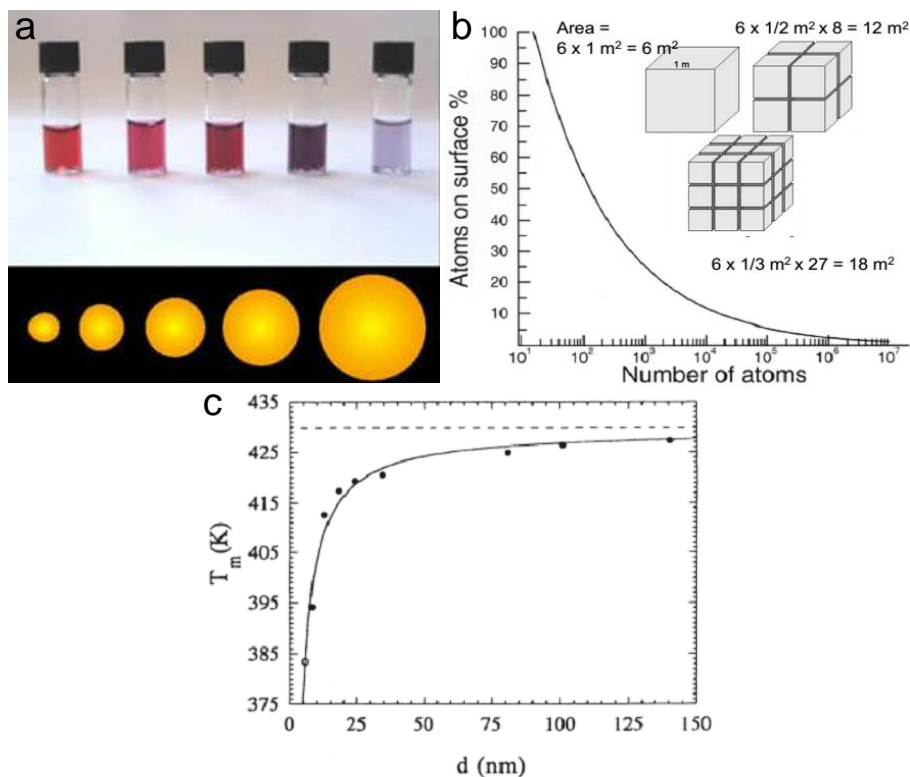


Figure 1.2 (a) Digital camera photos of various sizes of Au nanoparticles in solutions. Plot of (b) the number of atoms vs. the percentage of atoms located on the surface of a particle, and (c) melting point vs. diameter of the crystallite. (c) Reproduced with permission from ref (4).

Nanoparticles show thousand times of higher surface area than the bulk material of same mass. The fraction of surface atoms of a particle (P_s , percentage) can be estimated using the following equation,

$$P_s = 4N^{-1/3} * 100, N \text{ is the total number of atoms in a particle.}$$

Figure 1.2b depicts the dependency of surface fraction of atoms with total number of atoms in a particle. The contribution of surface atoms becomes trivial (<1%) only when size of the particle is about ~ 150 nm. Usually surface atoms have fewer coordination number than the bulk atoms. It leads to lower the stabilization energy; therefore the melting point of the surface layers comes down (Fig. 1.2c) (4).

1.2 Shape dependent properties

1.2a Optical properties of metal nanocrystallites

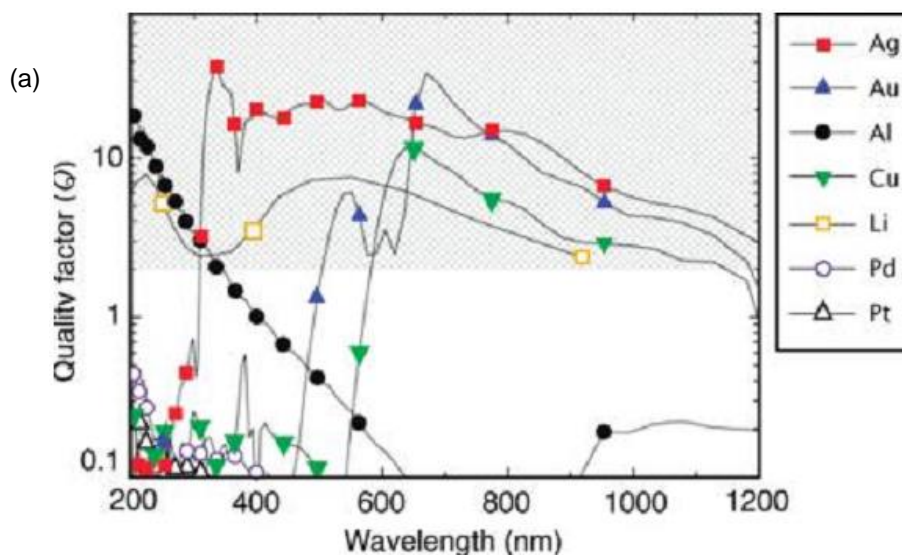


Figure 1.3 Quality factor (Q) of LSPR for a metal/air interface. Reproduced with permission from ref (5).

metal	plasmonic ability	chemical	nanostructure formation
aluminum (Al)	good in UV region	stable after surface passivation	very few nanostructures; used in lithographic patterning
copper (Cu)	interband transitions below 600 nm	easy oxidation	very few nanostructures
gold (Au)	interband transitions below 500 nm; high quality factor	very stable; biocompatible	many nanostructures
palladium (Pd)	low quality factor; not suitable for plasmonics	stable	many nanostructures
platinum (Pt)	low quality factor; not suitable for plasmonics	stable	many nanostructures
silver (Ag)	highest in quality factor	oxidation; biocompatibility issues	many nanostructures

Table 1.1 Comparison of noble metals for plasmonic applications. Reproduced with permission from ref (5).

The collective oscillation of conduction electrons is called localized surface plasmon resonance (LSPR). The conduction electrons of the metal nanocrystallite exhibit coherent oscillation under light irradiation (see Fig. 1.3). When it happens, an equal amount of restoring force generates due to the electrostatic interaction between electrons and nuclei. The oscillation frequency is determined by density of electrons, effective electron mass, and the shape and size of the charge distribution. The strength of surface plasmon is expressed by quality factor (Q) (5).

$$Q = \frac{\omega(d\varepsilon_r/d\omega)}{2(\varepsilon_i)^2}$$

ω = excitation frequency, ε = Dielectric constant, ε_i = imaginary dielectric constant and ε_r = real dielectric constant.

Among various interesting metals, Ag has the highest Q-factor from visible to near infrared (NIR) region (Fig. 1.3). In spite of highest Q-factor, chemical instability reduces the possible applications of Ag nanoparticles. Unlike Ag, Au shows extraordinary stability under various harsh conditions. Though it has lower Q-factor than Ag, stability makes Au a better plasmonic material (Table 1.1) (5).

Based on geometry, metal nanoparticles can be broadly classified as spherical and anisotropic crystallites. Spherical nanocrystallites exhibit a single absorption peak attributed to the dipolar surface plasmon. Ag nanoparticles exhibit 420 nm (Fig. 1.4a), while Au nanoparticles exhibit ~ 540 nm (Fig.1.4b) (6). Dipolar plasmon splits into transverse and longitudinal modes for anisotropic nanocrystallites. These modes are generated due to the oscillation of e-density along and perpendicular to the length of crystallites (Figs. 1.4c and d). Among all the possible nanoparticle morphologies, one-dimensional nanostructures like nanorods, nanowires and bipyramids have attracted significant interest due to their highly tunable localized surface plasmon resonance (LSPR). For instance, Au nanorods optical absorption can be tuned from visible to near infrared region by changing the aspect ratio (6). The Au nanorods with a pentagonal base and sharp apexes would lead to Au bipyramidal structures referred as nanorice. Both nanorods and bipyramids have two surface plasmon resonances namely transverse and longitudinal modes which arise due to the electron oscillations along the longitudinal and transverse directions. Since Au bipyramid tips are sharper than those of nanorods, the electric field enhancement is expected to be more at the tip of the Au bipyramids according to the lightning-rod effect (Fig. 1.4 e and f) (7). Due to this reason, Au bipyramids could be potential candidates for SERS.

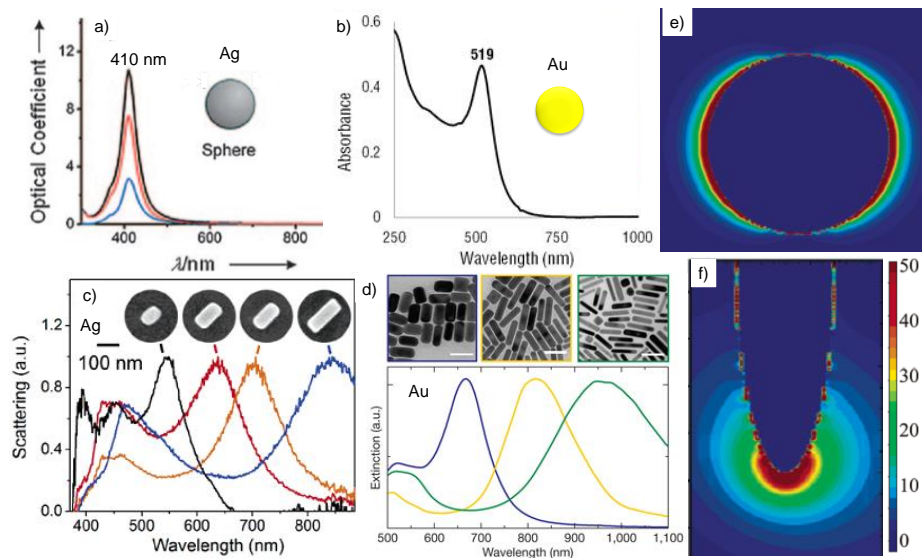


Figure 1.4 (a-d) Extinction spectra of Ag and Au nanocrystallites of various shapes. (e-f) E-field around the spherical and ellipsoid shaped crystallite. (a-f) Reproduced with permission from refs (6-9).

1.2b Catalytic properties

Noble metal nanocrystallites have been extensively used in catalysis application due to high surface area and stability under harsh chemical conditions. Size, shape and crystallographic orientation of surface influence the catalytic properties.

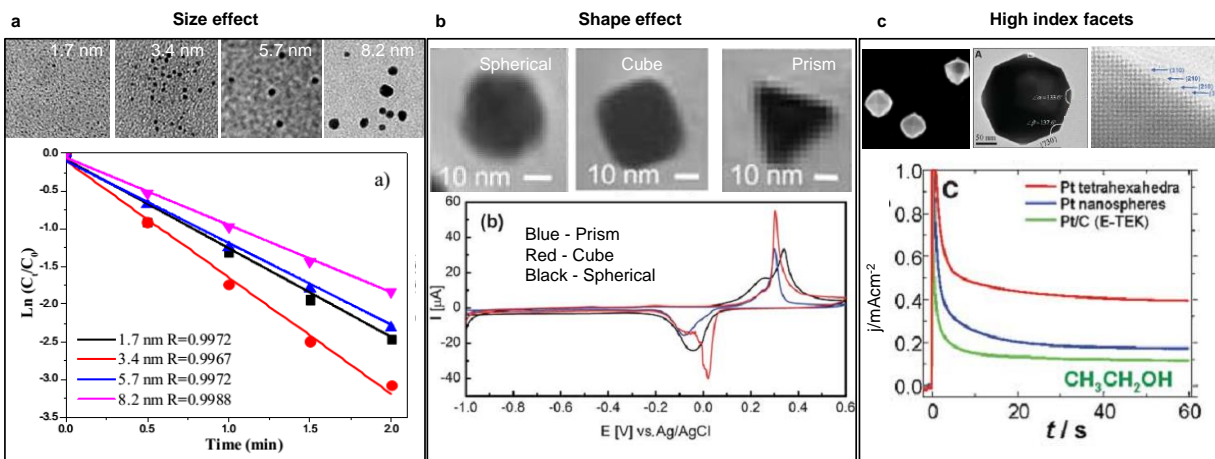


Figure 1.5 Effect of size (a), shape (b) and surface corrugations (c) on catalytic applications. (b, c) Reproduced with permission from refs (10, 11).

i. Size effect

It is known that smaller the size of particles higher is the catalytic activity. However, at sub 10 nm, size effects may alter; recently Zhou et al. mentioned that ~ 3.8 nm Au crystallites are apt for p-nitrophenol reduction, while lower (~ 1.7 nm) and higher (~ 8.2 nm) size crystallites exhibit lesser activity. Similarly Masel et al. have found that ~ 5 nm Ag particles have shown enhanced catalytic activity for CO₂ reduction as compared to bulk and 1 nm crystallites (Fig. 1.5a) (12).

ii. Shape effect

Shape of the crystallite influences catalytic activity to a great extent. For instance, Pd octahedrons show higher activity than cubes for the oxidation of CO. Bhargava et al. have compared the catalytic activity between spherical, cubic and triangular shaped Ag crystallites of nearly same size (10). The electrochemical reactivity order is nanocubes > nanospheres > nanoprisms (Fig. 1.5b) (10).

iii. Crystallographic orientation

Though bulk Au has high coordination number (12), situation at surface is different. Surface coordination number of low index planes such as {111}, {100} and {110} surfaces are 9, 8 and 7. Hence, the reactivity order is {110} > {100} > {111}. It is understood that catalytic activity of a surface can drastically increase by reducing the coordination number and the resultant surfaces are called high index facets. For these facets, one or more of miller indices are higher than one (h or k or $l \geq 2$), and these facets comprise of atoms with lowest coordination number (6). Wang et al. have prepared tetrahedral (THH) shaped submicron Pt crystallites enclosed with high index facets. These crystallites have shown 400% enhanced catalytic activity compared to conventional Pt/C electrodes (11). Further, synthesis of metal nanocrystallites exhibit high index surfaces and their possible catalytic applications have been explored (Fig. 1.5c) (13).

1.2c Surface Enhanced Raman Spectroscopy (SERS)

Raman spectroscopy is not ideal to probe vibration modes of analyte at low concentrations as the Raman cross section is much less. If a fluorescent dye analyte is under the study, there is a possibility that Raman signal being masked by the fluorescent back ground due to the high fluorescence cross section of analyte (10^{-17} cm² per molecule). However, the Raman cross

section can be improved by adsorbing the analyte on plasmonic metal (Au and Ag) nanocrystallites. Metals like Ag, Au and Cu exhibit SERS properties.

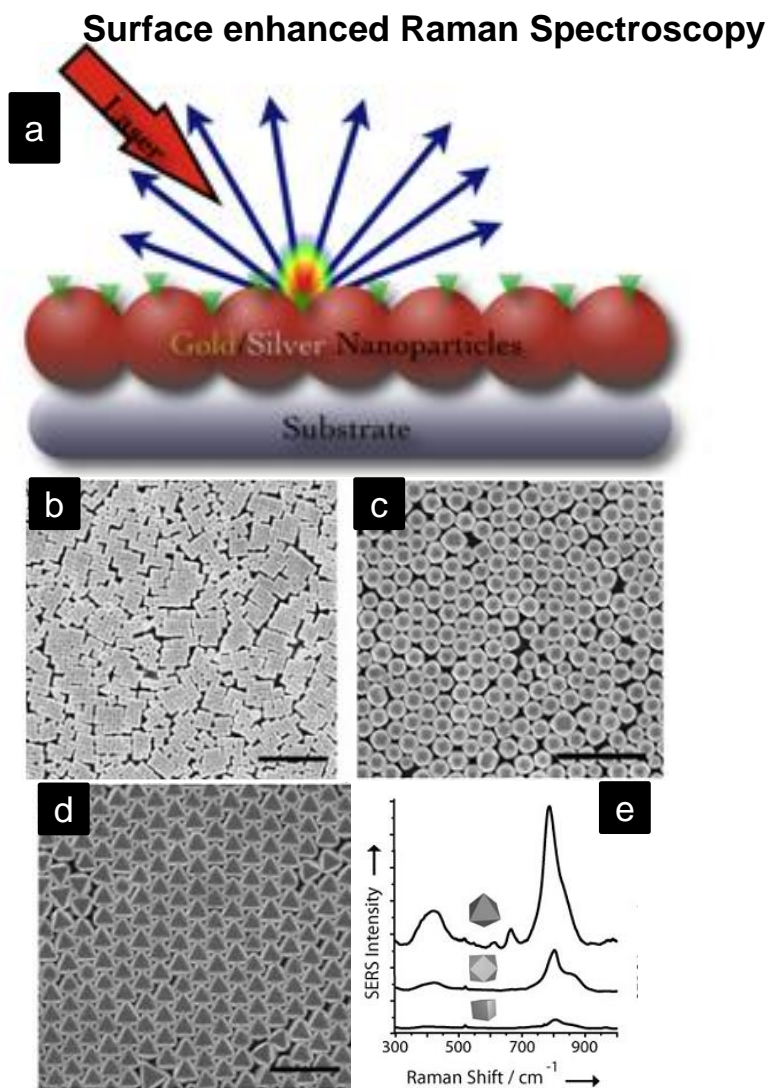


Figure 1.6 (a) Schematic illustration of SERS phenomenon. (b-d) TEM image of Au spherical, rods and flower shaped nanocrystallites. (e) SERS spectra of Na_2HSO_4 adsorbed on nanocrystallites. (b-e) Reproduced with permission from ref (14).

SERS phenomenon was first observed in 1973 and interpreted in 1977. The vibrational modes of molecules adsorbed on metal nanocrystallites are enhanced by many orders of magnitude. This phenomenon is called SERS. The two important enhancement mechanisms underlying the SERS phenomenon are namely electromagnetic and chemical enhancement mechanisms.

i. Electromagnetic enhancement mechanism

The electric field close to plasmonic metal surfaces is strong due to the surface plasmon resonance. Any analyte molecule placed near the surface will be under the influence of strong electric field (E_{Max}), it is the super position of incident field and the dipole field induced at the metal surface.

ii. Chemical enhancement mechanism

Electronic coupling between molecule and metal leads to formation of an adsorbate-surface complex, resulting in an increased Raman cross section of the adsorbed molecule in the complex. This forms a new (charge transfer) electronic transition in the metal-molecule system. This mechanism has mainly three steps.

The photon is absorbed by the metal nanostructures which results in a hot electron state.

The hot electron gets transferred into the LUMO of the molecule.

The hot electron is transferred from LUMO back to the metal nanostructures.

Return of the electron to its initial state by emitting Stokes photons.

The chemical enhancement mechanism contributes to an enhancement factor of 10 to 100 in magnitude.

Surface plasmons are strongly dependent on the composition, size and shape of the crystallite, hence SERS is influenced by these parameters. Numerous simulation studies have been carried out to understand the intensity of local electric field, and it is found that metal nanoparticles with sharp surface features host immense electric field at the tips. SERS measurements on various regular and complex shapes of Au and Ag nano and microcrystallites have been performed. It is observed that nanorods and 3D structures with sharp tips exhibit higher enhancement than spherical nanoparticles (Fig. 1.6) (14).

Synthesis of metal nanocrystallites

For synthesizing metal nanocrystallites, chemical, physical and biological methods have been adopted (Fig. 1.7). Chemical methods provide a great window to alter size and shape of the

nanocrystallites which is difficult with physical and biological methods. However the latter methods provide ligand free metal nanocrystallites unlike chemical routes.

1.3a Chemical methods

In the past two decades, numerous chemical routes have been developed for preparing metal nanocrystallites. Importantly these methods involve the reduction of metal ions using various sources. Few important synthetic methods to prepare plasmonic metal nanocrystallites are discussed here.

i. Plasmon mediated method

This method is an intriguing method because it depends on the localized surface plasmon resonance of noble metal nanocrystallites (15). This method is very much different from usual photochemical reduction, where metal ions are directly reduced to elemental state. It was introduced by the Mirkin group. Here, size and shape of Ag nanocrystallites can be tailored by varying the excitation wavelength (16).

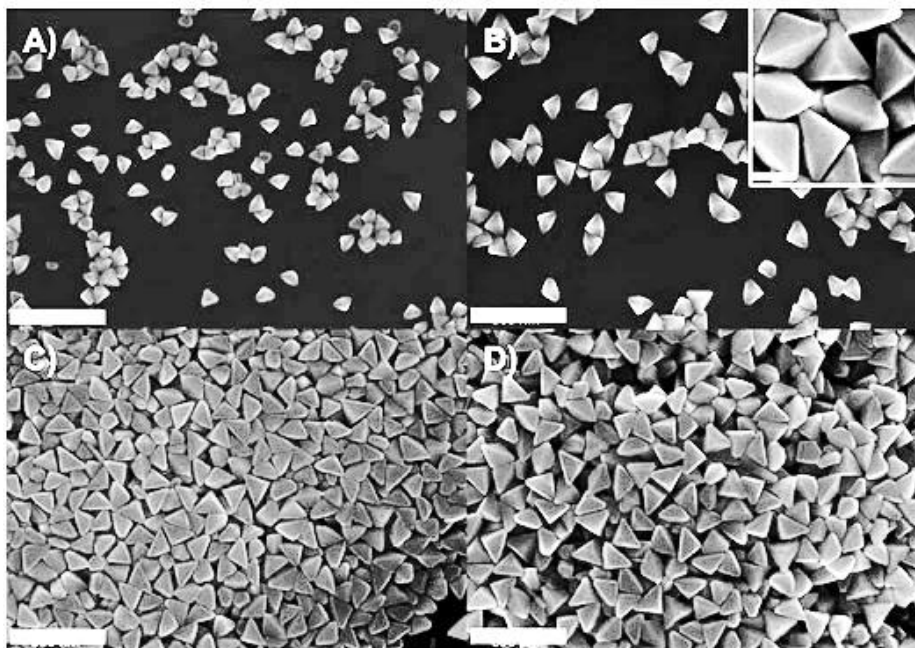


Figure 1.7 SEM images of Ag right triangular bipyramids of different shapes obtained by plasmon mediated route. Scale bar, 100 nm. Reproduced with permission from ref (16)

This method involves, irradiation of appropriate wavelength on reaction mixture which consists of Ag nanoparticles, Ag(I) precursor, and capping agent. The incident light couples to the LSPR of Ag nanocrystallites, and cause the formation of hot electrons. The plasmon decay of hot electrons assists the reduction of Ag(I) to Ag(0) by a reducing agent such as sodium citrate (17). On the other hand, bis-(p-sulfonatophenyl)-phenylphosphine (BSPP) oxidizes Ag to provide Ag(I) ions for reduction (18). Nanoprisms of ~ 100 nm were obtained using a fluorescent lamp. In further studies, size of prisms was maneuvered by excitation with two wavelengths or controlling the pH of the solution (Fig. 1.8). Larger prisms were obtained by irradiating radiation of higher wavelength. Generally it is observed that due to size effects, smaller crystallites grow faster than the larger crystallites until their localized surface plasmon resonance (LSPR) are suitably red shifted (16).

ii. The polyol synthesis

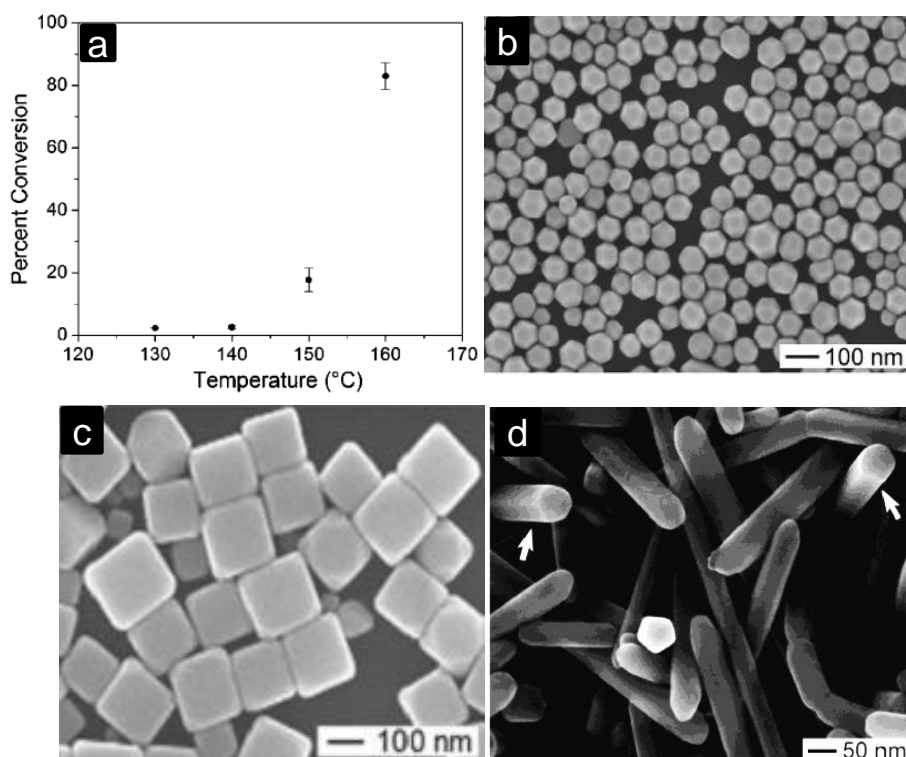


Figure 1.8 (a-d) Ag nanocrystallites of various shapes obtained from Polyol method. (a-d) Reproduced with permission from refs (19-21).

Among numerous solution based method, polyol route has gained much attention due to its simplicity and handiness to prepare in bulk quantity. It involves the reduction of metal salts with polyol and polymer capping agent at moderate temperatures. This method was introduced by the Xia group. AgNO₃, poly(vinyl pyrrolidone) (PVP) and ethylene glycol (EG) have been served as metal source, capping agent and polyol respectively (21). Continuous generation of reductant takes place upon heating of EG. In a way the reduction power of EG and reaction temperature are related. Figure 1.8a shows the effect of reaction temperature on Ag(I) to Ag(0) conversion, and it is clear that a varied range of reduction rates are possible by altering the temperature. At early stage of the reduction, small Ag clusters may form from the aggregation of atoms acquired from reduction of Ag(I) ions. Besides the temperature, additives such as chloride, atmospheric oxygen (O₂) (20) and Fe(II) (19) also influence the shape of the nanocrystallite drastically. Various interesting shapes like truncated octahedrons, cubes and penta-twinned Ag nanorods have been obtained by using polyol method (Figs. 1.8b-d) (21).

iii. Thermal reduction

Nakamoto and coworkers introduced the thermal reduction of metal organic complex, without the aid of any external reducing agent. It is the only method that provides suitable conditions to grow nano, micro and sub millimeter crystallites on a desired substrate. Since thermal reduction depends on thermolysis temperature, size and shape of the crystallites can be tuned drastically. Au nanocrystallites of below 100 nm were obtained by the thermal decomposition of [C₁₄H₂₉(CH₃)₃N][Au(SC₁₂H₂₅)₂] at 180 °C under N₂ atmosphere (Fig. 1.9a) (22). Later, few more metal organic precursors have been explored to prepare Au, Ag, Pd, Pt and Cu nanocrystallites.

Kulkarni and coworkers have introduced a versatile method to synthesize single crystalline and ultra-smooth Au microcrystallites (Fig. 1.9b), using M-ToABr (M=Au, Ag, Pt, Pd and Cu) complexes obtained by phase transfer of metal salt anions to the organic layer by ToABr (23). The size was controlled by varying the concentration of reactants and thermolysis temperature. The metal organic precursors provide a wide range of thermolysis temperatures (130-250 °C) (24). At low temperatures (~ 130 °C) sub millimeter size (~ 400 μm) Au crystallites were seen, while much lesser size crystallites (~ 30 μm) were observed at higher temperature (25, 26). In addition to above methods, many more routes have been reported to synthesize metal nanocrystallites of various shapes.

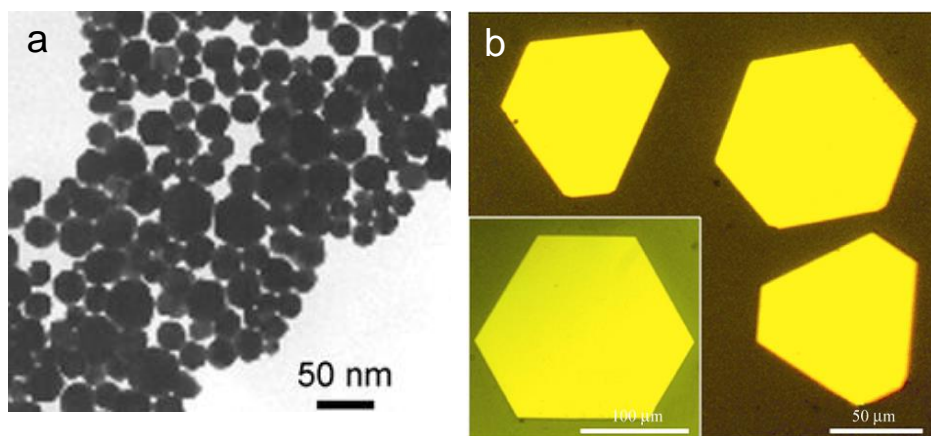


Figure 1.9 (a) TEM image of Au nanocrystals obtained from $[C_{14}H_{29}(CH_3)_3N][Au(SC_{12}H_{25})_2]$, and (b) optical microscopy image of Au polygons obtained by thermal reduction of Au-ToABr complex. (a, b) Reproduced with permission from ref (22, 24).

1.4 Shape of metal nanocrystallites

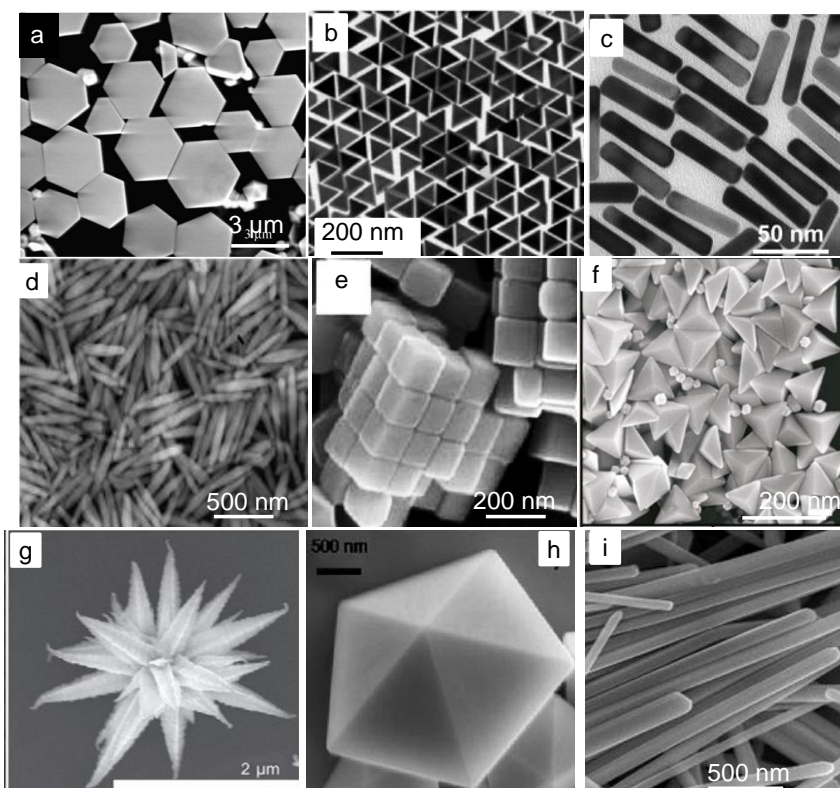


Figure 1.10 SEM images of Au and Ag nanocrystallites of various shapes. (a, i) Reproduced with permission from refs (24, 27-33).

Shape of the crystallite is an important parameter that influences properties such as optical, magnetic, catalytic, etc. The reported shapes for various transition metals are shown in Fig. 1.10 and Table 1.2.

Table 1: A summary of different shapes that have been achieved for various metal nanocrystals.

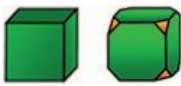













Structures	Shapes	Schematic drawings	Metals
single-crystal	perfect/truncated cube ^[a]		Pd, Ag, Au, Pt, Cu, Rh, Bi, Fe
	perfect/truncated octahedron ^[a]		Pd, Ag, Au, Pt
	perfect/truncated tetrahedron ^[a]		Ag, Au, Pt, Rh
	rectangular bar		Pd, Ag, Pt
	octagonal rod		Pd, Au, Fe, Co, Ni
	rectangular or octagonal wire		Pb, In, Sn, Sb, Fe, Co
singly twinned	right bipyramid		Pd, Ag
	beam		Ag
multiply twinned	decahedron ^[a]		Pd, Ag, Au
	icosahedron ^[a]		Pd, Au
	five-fold twinned pentagonal rod		Pd, Ag, Au, Cu
	five-fold twinned pentagonal wire		Ag, Au, Cu
	triangular/hexagonal plate		Pd, Ag, Au, Cu, Pb, Bi, Co, Ni
	disc		Sn, Co

Table 1.2 Summary of various shapes that have been obtained for various transition metals. Reproduced with permission from ref (6).

The shapes exhibited by noble metals are hexagons (24), triangles (29), rods (34), rice (28), cubes (33), trigonal bipyramids (31), mesoflowers (27) and penta-twinned nanowires (35). Usually FCC metals such as Au, Ag, Cu, Pd and Pt take the symmetry allowed geometries such as triangle (3-fold), cube (4-fold) and hexagon (6-fold). However, shape of the nanocrystallite can be tuned by choosing an appropriate capping agent.

1.3b Growth evolution

Growth of metal nanocrystallites involves the following general steps (Fig. 1.11).

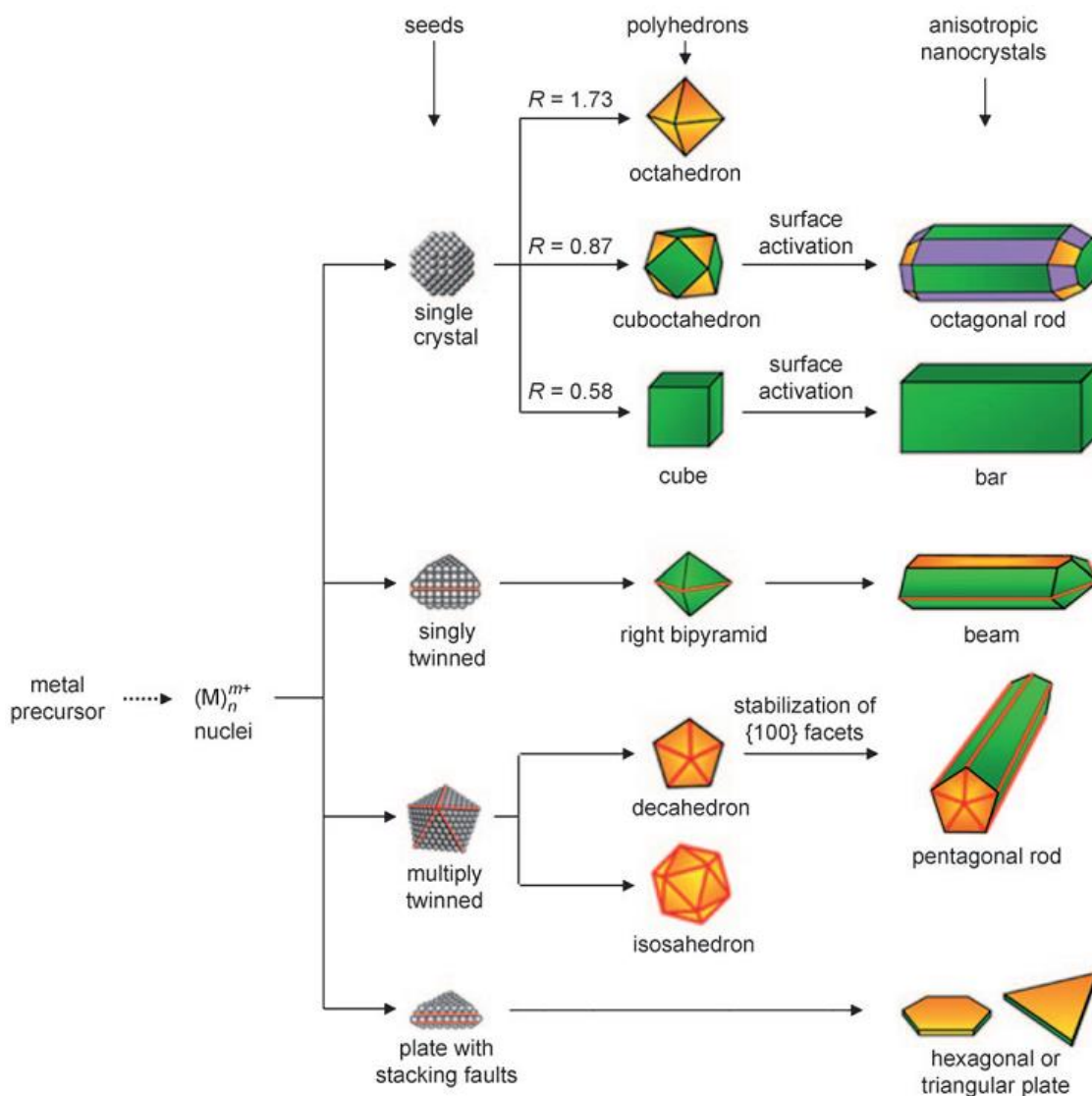


Figure 1.11 The possible reaction paths reported in order to obtain various interesting shapes of FCC metals. Reproduced with permission from ref (6)

i. Nucleation of seed

To obtain well shaped crystallites, formation of nuclei is very critical. Small nanocrystallites serve as nucleation sites, and also influence the growth on various sites. Shape control synthesis was carried out via either homogeneous or heterogeneous nucleation.

ii. Selective adsorption of capping agents and nanocrystal growth

Various polymers and quaternary salts have been employed as capping agents to maneuver shape and size of the nanocrystallites. Typically used capping agents are poly(vinyl pyrrolidone) (PVP), poly(vinyl alcohol) (PVA), cetyltrimethylammonium bromide (CTAB), tetraoctylammonium bromide (ToABr), sodiumdodecylsulfate (SDS) and bis(2-ethylhexyl)sulfosuccinate (AOT). The capping agents selectively get adsorbed on specific planes and therefore control the growth at various sites. Local coordination number of a crystal plane and molecular structure influence the adsorption of capping agent on specific site. Selective adsorption on a set of planes causes the anisotropic growth, and eventually produces 1D, 2D and branched structures. From various energy calculations and experimental observations it was understood that PVP and citrate selectively adsorbed on Ag (100) and (111) planes respectively.

In predicting the final morphology of the nano and microcrystallites surface energy consideration is much crucial. Surface energy strongly determines the growth on a facet of a crystal. Unlike amorphous materials, metals show different surface energies for different crystallographic planes. Usually, metal crystallites take the shape having minimum surface energy. The crystal structure of most of the noble metals is face centered cubic (FCC), and the surface energy order is $\{111\} < \{100\} < \{110\} < \{hkl\}$. Hence, most of the shapes are enclosed with low energy (111) and (100) surfaces (Fig. 1.10).

1.5 Strain in metal nanocrystallites

Metal nanocrystallites with five-fold symmetry are widely observed, yet the fine details of the geometry are not well documented. Decahedron, icosahedrons and penta-twinned nanorods/wires are well known geometries which exhibit five-fold cross section (Fig. 1.12) (6). Decahedron and icosahedrons are enclosed with $\{111\}$ facets, while tips and side faces of the nanorods/wires are $\{111\}$ and $\{100\}$ facets respectively. Decahedron is an assembly of five tetrahedron units

sharing a common edge. Theoretical angle between two adjacent tetrahedrons is 70.53° ; joining five tetrahedrons leaves a gap of 7.35° , which should be filled by elongating the Au-Au bond length. Such elongation will cause internal lattice strain and distorts the crystal structure. The strain increases with diameter of decahedron; hence, observation of large decahedrons is rare (6). Similarly icosahedron (36) and penta-twinned nanorods (35) also have host internal strain due to the five-fold symmetry (Figs. 1.12 b-d).

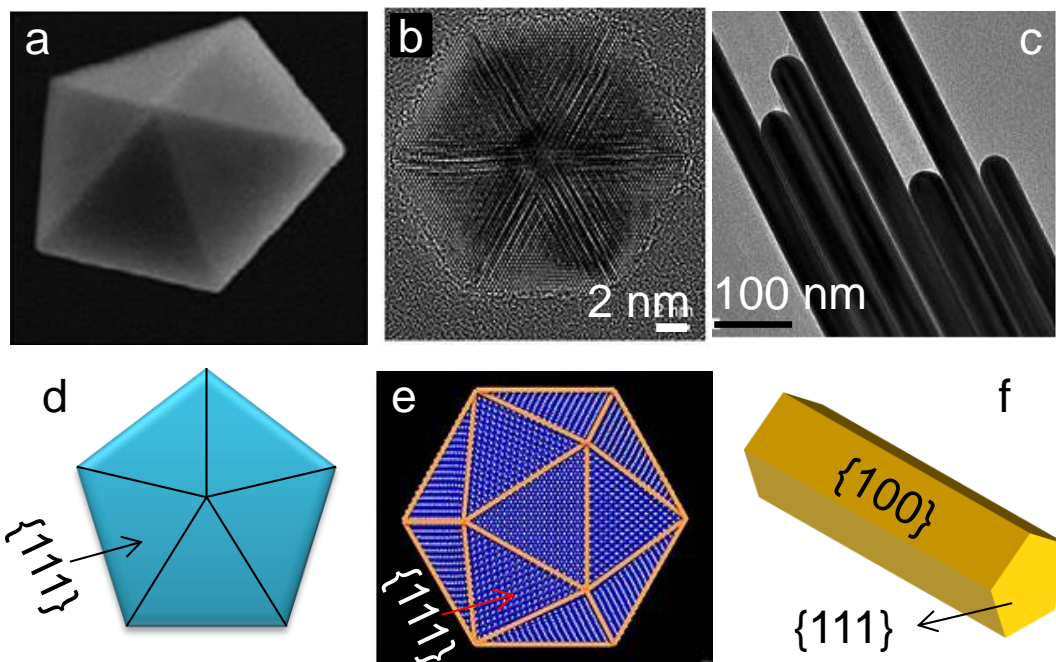


Figure 1.12 (a-c) Microscopy images of decahedron, icosahedron and penta-twinned nanowires of Au nanocrystallites. (d-f) The corresponding schematics are given below. Reproduced with permission from ref (35-37).

1.6 Nanostructured surfaces

1.6a Nanoholes in metal films

Ebbesen's pioneering work on enhanced optical transmission through nanoholes has opened lot of interest in fabricating nanoholes in metal films and studying their optical properties (38). Various lithography methods such as focused ion beam (FIB) lithography, nanospheres lithography, etc have been used to fabricate perforated metal films. Periodic lattices of nanoholes with various shapes such as circular, square and rectangle have been fabricated in Au and Ag

nanofilms (Fig. 1.13(a-c)) (38, 39). These nanofilms have served as SERS substrates. Occasionally random holes have also been fabricated (Fig. 1.13(d)).

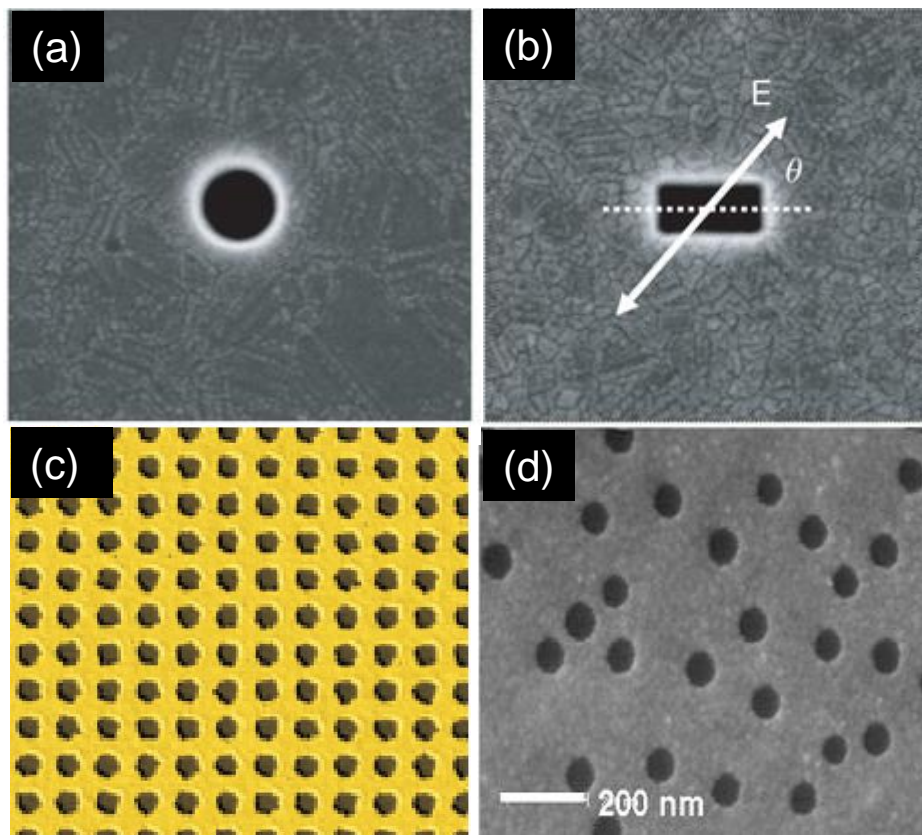


Figure 1.13 (a-d) SEM images of nanoholes of various shapes in metal films. Reproduced with permission from refs (38, 40, 41).

1.6b Metal nanosponges

There exist numerous applications for porous materials due to high surface area. Nanoporous noble metals, a subset of porous materials are interesting due to their catalytic and optical properties (42). Fabrication of porous systems with controlled pore size is in high demand owing to rich surface chemistry. Dealloying of AuAg alloy in nitric acid (HNO_3) is a well-known technique to fabricate porous Au nanosponge (43). Annealing metal film at higher temperature, and electro deposition also have been used to prepare metal nanosponges (42). The above methods involve the usage of harsh acids and higher annealing temperatures.

Recently, Eswaramurthy et al have come up with a simple method to prepare nanosponges of Au, Ag, Pd and Pt by reducing the metal salts with strong reducing agent like NaBH_4 . The nanosponge thus obtained is comprised of ~ 10 nm broad ligaments (Fig. 1.14) (44).

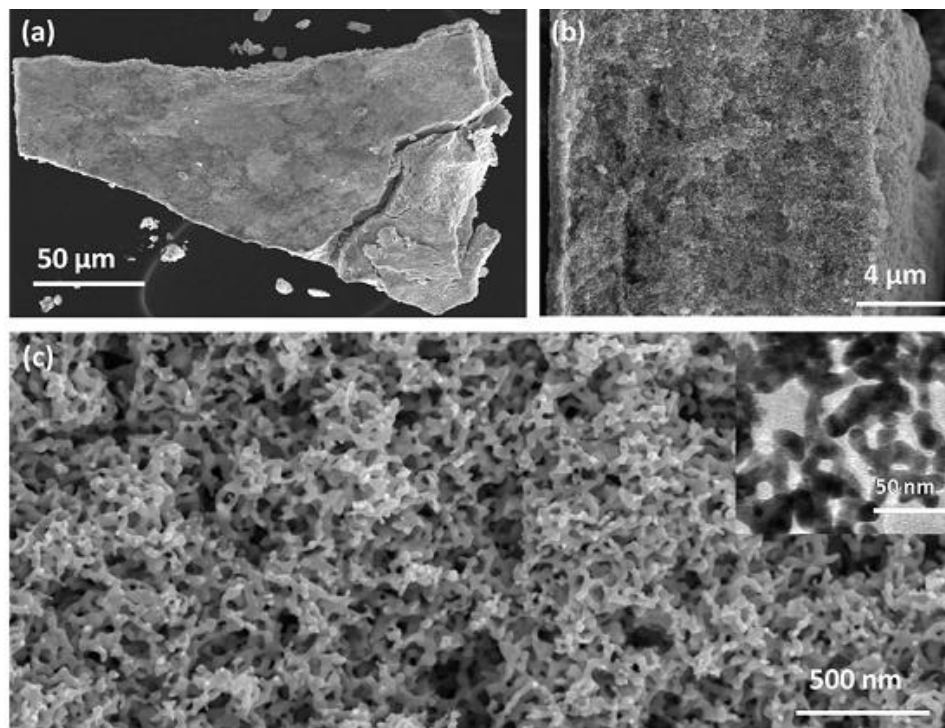


Figure 1.14 SEM images at different magnifications of Au nanosponge. Reproduced with permission from ref (44).

1.7 Physical methods

To prepare nanocrystalline metal films those are free of solvent contamination physical methods are adequate. Laser ablation (45) and evaporation-condensation (46) are well known ways to bring nanoparticles on a desired substrate. Though evaporation route yields organic ligand free metal nanocrystallites, it needs high temperature, large amount of energy and space. Suji et al have reported the Ag nanoparticles synthesis by using laser ablation of bulk Ag (47). The obtained nanoparticles are of ~ 20 -50 nm with no defined shape. Shape controlling in physical methods is very difficult or impossible, in spite of controlling organic ligands and solvents in the synthesis. Hence the use of physical methods in metal nanocrystallites is limited.

1.8 Biological methods

Biological methods are not well established like other methods, there are few attempts to prepare metal nanocrystallites using bacteria and fungi. For nanoparticles synthesis, it is an alternative method to chemical method. Sastry et al. have introduced a simple biological route to prepare submicron size triangle shaped Au crystallites (48). Further, various biological organisms have been employed to prepare Ag and Pt nanocrystallites (49). However, biological method is not very suitable to obtain shape controlled metal nanocrystallites.

1.9 Lithography

Though chemical routes are well established to produce various interesting shapes, unfortunately they are not very helpful in producing complex geometries such as grating nanowires etc. To create such intriguing shapes lithography methods have been adopted. Using lithography methods non-periodic patterns such as circuits and periodic patterns such as gratings are fabricated.

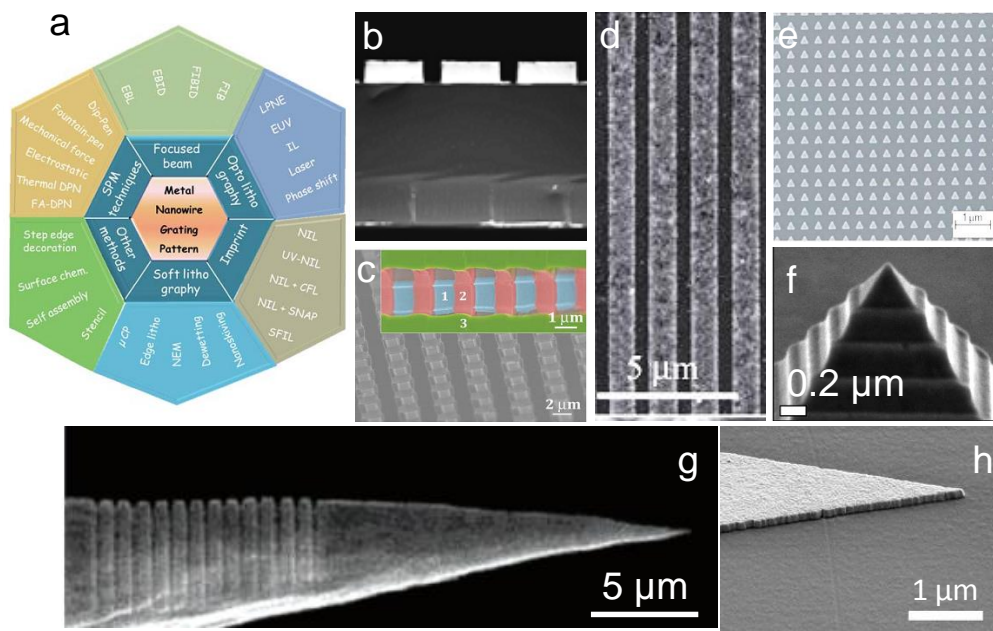


Figure 1.15 (a) A palette showing the fabrication techniques. (b-h) SEM images of metal nano and microstructures obtained from various lithography techniques. Reproduced with permission from refs (50-55).

Lithography is an art of producing picture on a flat substrate by using various routes. The size of feature can be tuned from micrometer to nanometer by choosing appropriate technique (Fig. 1.15). Photolithography is an optical means for creating patterns on a substrate. The lithography tool-kit comprise of resists (polymers), light source and a substrate (glass or any other) (56). Resists spin coated on a desired substrate are pre baked in an oven or hot plate to evaporate the solvent from the resist. Next step is the mask alignment, exposing the resist through high intensity ultraviolet light. There are three primary exposure methods: contact, proximity, and projection. Using photo lithography, down to a micron size features can be obtained (Fig. 1.15(b)).

Whitesides group at Harvard University introduced Soft lithography method (57). It is an affordable and rapid technique for patterning wide range of function materials on a desired substrate. The term “soft” refers to the use of materials involved in stamping elastomers as well as organic molecules. Poly(dimethyl siloxane) or Sylgard 184 is a well-known silicon elastomer. For the PDMS stamp fabrication base material (vinyl terminated siloxane prepolymer) and cross-linking agent (siloxane) are mixed in 1:10 ratio and heated at 60 °C for 6h. Once the stamp is fabricated with desired features, used for many purposes such as micromolding and imprinting (Fig. 1.15(d)) (58). PDMS deforms under external stress, and swell in various organic solvents such as toluene and hexane. It is also difficult to fabricate defect free PDMS stamps over large area. Hence, soft lithography has failed at many aspects. This demand for a rigid stamp than elastic one.

Chou et al., developed NIL method developed by employs a rigid master such as glass or quartz (59). A rigid master used for embossing a polymer that has been heated at melting point. It is considered as next generation lithography due to high through put and size of the features which is well below 50 nm (Fig. 1.15(c)). Similarly, various other lithography techniques such as template stripped lithography (60) (Fig. 1.15(f)), dip pen lithography (61) have been adopted do create nanofeatures of metals on any desired substrate. The above mentioned lithography methods have been employed to produce metal anisotropic structures. However, such processes are expensive, and not suitable for large scale synthesis.

Due to small e-beam probe size and wavelength, EBL provides excellent resolution which is limited by the wavelength of the light that is used (62). In direct writing, a small e-beam spot is

moved with respect to the wafer to expose the wafer one pixel at a time, eliminating the expensive and time-consuming production of masks. Poly(methyl methacrylate) (PMMA) has been the most widely used and high resolution positive-tone resist and hydrogen silsesquioxane (HSQ), a relatively new resist material, is a high resolution negative-tone resist. Typically the writing field, which is defined by the maximum deflection range of the e-beam, is of the order of a few hundred micrometers. Larger patterns require mechanical stage movements, which need to be very accurate in order to precisely stitch consecutive writing fields. The process steps involved in EBL are similar to that of the photolithography (Fig. 1.15(e)) (63).

1.10 Advantages of microcrystallites

At nanoscale, the size and shape of a metal crystallite influence the optical, electronic, catalytical and structural properties. Various physical, chemical and bio-methods have been reported for shape controlled synthesis of nanocrystallites. High end techniques such as HRTEM and high energy X-ray diffraction techniques have been used to understand the growth and structural aspects of nanocrystallites. However, it is not always possible to access such expensive techniques. In spite of numerous applications in various fields, nanoparticles are not quite suitable for few specific applications such as nano-focusing of light, creating interesting plasmonic structures over larger areas and also to understand growth or etching of various shaped crystallites in a simple way. In addition, the finite size limits the manipulation and transferring a desired crystallite from one to another substrate. To address the mentioned problem, microcrystallites have been revisited. Hitherto, micronsize long Ag and Cu were the only known microstructure, while no other shapes have been reported. Though there are few attempts to grow atomically smooth single crystalline metal films, they lack the desired quality. In addition to the size, quality of the crystallite also matters for reliable results. Hence, fabrication of single crystalline micron size metal nanocrystallites is indeed in demand. The thesis deals with the fabrication of Au and Ag microcrystallites using metal organic precursors. Importantly, the obtained microcrystallites provide extended planar surfaces like the bulk with corners and edges similar to the nanocrystallites. The larger dimensions are also a platform in realizing metastable crystal structures, possibly without any external influence such as pressure. The thesis is an exploration of the above mentioned aspects using only routine characterization tools.

References

1. Z. Mu, X. Zhao, Z. Xie, Y. Zhao, Q. Zhong, L. Bo, Z. Gu, *J Mater Chem B* **1**, 1607-1613 (2013).
2. <http://www.wisegeek.org/what-are-the-different-uses-for-talcum-powder.html>.
3. <http://www.webexhibits.org/causesofcolor/9.html>.
4. E. Roduner, *Chem Soc Rev* **35**, 583-592 (2006).
5. M. Rycenga, C. M. Cobley, J. Zeng, W. Li, C. H. Moran, Q. Zhang, D. Qin, Y. Xia, *Chem Rev* **111**, 3669-3712 (2011).
6. Y. Xia, Y. Xiong, B. Lim, S. E. Skrabalak, *Angew Chem-Int* **48**, 60-103 (2009).
7. Z. Junxi, Z. Lide, X. Wei, *J Phy D: Appl Phys* **45**, 113001 (2012).
8. K. L. Kelly, E. Coronado, L. L. Zhao, G. C. Schatz, *J Phys Chem B* **107**, 668-677 (2003).
9. B. Wiley, Y. Sun, Y. Xia, *Acc Chem Res* **40**, 1067-1076 (2007).
10. V. Bansal, V. Li, A. P. O'Mullane, S. K. Bhargava, *CrystEngComm* **12**, 4280-4286 (2010).
11. N. Tian, Z.-Y. Zhou, S.-G. Sun, Y. Ding, Z. L. Wang, *Science* **316**, 732-735 (2007).
12. C. Lin, K. Tao, D. Hua, Z. Ma, S. Zhou, *Molecules* **18**, 12609-12620 (2013).
13. Q. Zhang, H. Wang, *ACS Catal* **4**, 4027-4033 (2014).
14. M. Li, S. K. Cushing, J. Zhang, J. Lankford, Z. P. Aguilar, D. Ma, N. Wu, *Nanotechnology* **23**, 115501 (2012).
15. J. E. Millstone, S. J. Hurst, G. S. Métraux, J. I. Cutler, C. A. Mirkin, *Small* **5**, 646-664 (2009).
16. J. Zhang, S. Li, J. Wu, G. C. Schatz, C. A. Mirkin, *Angew Chem-Int* **48**, 7787-7791 (2009).
17. X. Wu, P. L. Redmond, H. Liu, Y. Chen, M. Steigerwald, L. Brus, *J Am Chem Soc* **130**, 9500-9506 (2008).
18. C. Xue, G. S. Métraux, J. E. Millstone, C. A. Mirkin, *J Am Chem Soc* **130**, 8337-8344 (2008).
19. B. Wiley, Y. Sun, Y. Xia, *Langmuir* **21**, 8077-8080 (2005).
20. B. Wiley, T. Herricks, Y. Sun, Y. Xia, *Nano Lett* **4**, 1733-1739 (2004).
21. Y. Sun, B. Mayers, T. Herricks, Y. Xia, *Nano Lett* **3**, 955-960 (2003).

22. M. Nakamoto, M. Yamamoto, M. Fukusumi, *Chem Commun*, 1622-1623 (2002).
23. B. Radha, S. Kiruthika, G. U. Kulkarni, *J Am Chem Soc* **133**, 12706-12713 (2011).
24. B. Radha, M. Arif, R. Datta, T. Kundu, G. Kulkarni, *Nano Res* **3**, 738-747 (2010).
25. B. Radha, G. U. Kulkarni, *Curr Sci* **102**, 70-77 (2012).
26. B. Radha, G. U. Kulkarni, *Cryst Growth Des* **11**, 320-327 (2011).
27. P. Sajanlal, T. Pradeep, *Nano Res* **2**, 306-320 (2009).
28. H. Liang, H. Yang, W. Wang, J. Li, H. Xu, *J Am Chem Soc* **131**, 6068-6069 (2009).
29. L. Scarabelli, M. Coronado-Puchau, J. J. Giner-Casares, J. Langer, L. M. Liz Marzán, *ACS Nano* **8**, 5833-5842 (2014).
30. K. E. Korte, S. E. Skrabalak, Y. Xia, *J Mater Chem* **18**, 437-441 (2008).
31. M. L. Personick, M. R. Langille, J. Zhang, N. Harris, G. C. Schatz, C. A. Mirkin, *J Am Chem Soc* **133**, 6170-6173 (2011).
32. A. Mayoral, H. Barron, R. Estrada-Salas, A. Vazquez Duran, M. Jose Yacaman, *Nanoscale* **2**, 335-342 (2010).
33. M. Rycenga, J. M. McLellan, Y. Xia, *Adv Mater* **20**, 2416-2420 (2008).
34. C. Zhang, A.-X. Yin, R. Jiang, J. Rong, L. Dong, T. Zhao, L.-D. Sun, J. Wang, X. Chen, C. H. Yan, *ACS Nano* **7**, 4561-4568 (2013).
35. F. Kim, K. Sohn, J. Wu, J. Huang, *J Am Chem Soc* **130**, 14442-14443 (2008).
36. J. Wu, W. Gao, J. Wen, D. J. Miller, P. Lu, J.-M. Zuo, H. Yang, *Nano Lett* **15**, 2711-2715 (2015).
37. G. Walters, I. P. Parkin, *J Mater Chem* **19**, 574-590 (2009).
38. C. Genet, T. W. Ebbesen, *Nature* **445**, 39-46 (2007).
39. J. Braun, B. Gompf, T. Weiss, H. Giessen, M. Dressel, U. Hübner, *Phy Rev B* **84**, 155419 (2011).
40. D. Gao, W. Chen, A. Mulchandani, J. S. Schultz, *Appl Phys Lett* **90**, 073901 (2007).
41. J. Braun, B. Gompf, T. Weiss, H. Giessen, M. Dressel, U. Hübner, *Phys Rev B* **84**, 155419 (2011).
42. R. Zhang, H. Olin, *Materials* **7**, 3834 (2014).
43. M. M. Collinson, *ISRN Anal Chem* **2013**, 21 (2013).
44. K. S. Krishna, C. S. S. Sandeep, R. Philip, M. Eswaramoorthy, *ACS Nano* **4**, 2681-2688 (2010).

45. S. Barcikowski, G. Compagnini, *Phys Chem Chem Phys* **15**, 3022-3026 (2013).
46. H. Förster, C. Wolfrum, W. Peukert, *J Nanopart Res* **14**, 1-16 (2012).
47. T. Tsuji, K. Iryo, N. Watanabe, M. Tsuji, *Appl Surf Sci* **202**, 80-85 (2002).
48. S. S. Shankar, A. Rai, B. Ankamwar, A. Singh, A. Ahmad, M. Sastry, *Nat Mater* **3**, 482-488 (2004).
49. K. Roy, C. K. Sarkar, C. K. Ghosh, *Appl Nanosci*, 1-7 (2014).
50. B. Radha, G. Kulkarni, *Nano Res* **3**, 537-544 (2010).
51. N. C. Lindquist, P. Nagpal, A. Lesuffleur, D. J. Norris, S.-H. Oh, *Nano Lett* **10**, 1369-1373 (2010).
52. G. U. Kulkarni, B. Radha, *Nanoscale* **2**, 2035-2044 (2010).
53. B. Radha, S. H. Lim, M. S. M. Saifullah, G. U. Kulkarni, *Sci. Rep.* **3**, 1078 (2013).
54. D. K. Gramotnev, S. I. Bozhevolnyi, *Nat Photon* **4**, 83-91 (2010).
55. C. David, J. Bruder, T. Rohbeck, C. Grünzweig, C. Kottler, A. Diaz, O. Bunk, F. Pfeiffer, *Microelectron Eng* **84**, 1172-1177 (2007).
56. <http://www.kettererkunst.com/dict/lithography.shtml>.
57. Y. Xia, G. M. Whitesides, *Angew Chem Int Ed* **37**, 550-575 (1998).
58. X. M. Zhao, Y. Xia, G. M. Whitesides, *J Mater Chem* **7**, 1069-1074 (1997).
59. Q. Xia, S. Y. Chou, in *Proceedings of SPIE - The International Society for Optical Engineering* **5725**, 180 (2005).
60. P. Nagpal, N. C. Lindquist, S.-H. Oh, D. J. Norris, *Science* **325**, 594-597 (2009).
61. B. Radha, G. Liu, D. J. Eichelsdoerfer, G. U. Kulkarni, C. A. Mirkin, *ACS Nano* **7**, 2602-2609 (2013).
62. A. A. Tseng, C. Kuan, C. D. Chen, K. J. Ma, *IEEE Transactions on Electronics Packaging Manufacturing* **26**, 141 (2003).
63. A. E. Grigorescu, C. W. Hagen, *Nanotechnology* **20**, 292001 (2009).

Several microscopic and spectroscopic techniques have been used to characterize the samples reported in the thesis. In the following paragraphs, the details of instruments used and the sample preparation methods are described.

Microscopy

Scanning electron microscopy (SEM) and Energy-dispersive X-ray spectroscopy (EDS)

SEM was performed using a Nova NanoSEM 600 equipment (FEI Co., The Netherlands). Energy dispersive spectroscopic (EDS) mapping was performed using EDAX Genesis V4.52 (USA) attached to the SEM column. The EDS mapping was performed at 10 kV (energy window, 10 eV) with a beam current of 1.1 nA, the dwell time per pixel being 25 μ s. Low vacuum imaging was performed on the same instrument using a helix detector. Energy-dispersive X-ray spectra were collected with 15 kV, performed using a Nova NanoSEM 600 equipment (FEI Co., The Netherlands).

Transmission electron microscopy (TEM) and Electron Diffraction (ED)

Transmission electron microscopy (TEM) measurements were carried out with a JEOL-3010 instrument operating at 300 kV ($\lambda = 0.0196 \text{ \AA}$) and electron diffraction (ED) patterns were collected at a camera length 20 cm (calibrated with respect to the standard polycrystalline Au thin film). Samples for TEM were prepared by depositing a drop of the nanomaterial (scraped from the substrate) on a holey carbon copper grid, allowing it to dry in a desiccator overnight.

Atomic force microscopy (AFM)

AFM experiments were carried out using Bruker diInnova Scanning Probe Microscope with Nanodrives controller. Imaging has been done in tapping Mode. TESP etched silicon cantilever probes of 125 μ m nominal length were used, at a drive frequency of approximately 240–280 kHz. Both height and amplitude information were recorded at a scan rate of 2–3 Hz, and stored

in a 512-512 pixel format. Images were processed using the Nanoscope version 7.30 software. For optimum clarity in visual presentation of the images, flattening of first order was employed unless stated otherwise.

X-ray diffraction (XRD)

Powder X-ray diffraction measurements were performed using a Siemens Seifert 3000TT diffractometer employing Cu K α ($\lambda = 1.5406 \text{ \AA}$) radiation. Samples were prepared by depositing the nanomaterials in the form of films on glass slides and typical scan rate was 1 deg.min^{-1} .

Thermogravimetric analysis (TGA)

TGA was carried out (Mettler Toledo, TG-850) usually in the temperature range of $30 \text{ }^\circ\text{C} - 300 \text{ }^\circ\text{C}$ at a heating rate of $2 \text{ }^\circ\text{C.min}^{-1}$ in air. Typically using 10 mg of the sample in solid form mounted on a porcelain boat.

X-ray photo electron spectroscopy (XPS)

XPS measurements have been carried out using Omicron SPHERA spectrometer with non-monochromatic AlK α X-rays ($E=1486.6 \text{ eV}$).

Raman Measurements

Raman measurements were performed using LabRAM HR apparatus (Horiba, USA) with an excitation wavelength of 632.8 nm and 5 mW.cm^{-2} . Signal accumulation was performed for 10 s with a spot size of $1 \text{ }\mu\text{m}$.

FTIR

Fourier transform infrared (FTIR) measurements were done using a Bruker IFS66v/s spectrometer with a resolution of $\sim 2 \text{ cm}^{-1}$.

Facet Selective Etching of Au Microcrystallites

Summary

High symmetry crystals, by nature, exhibit isotropic properties. The possibility of inducing anisotropy for example by facet selective etching, is considered highly remote in face centered cubic (FCC) metals, particularly in gold, which besides being FCC, is also noble. Here, for the first time, facet selective etching of Au microcrystals obtained in the form of cuboctahedrons and pentagonal rods from thermolysis of a gold-organic precursor is reported. The selective etching of {111} and {100} facets has been achieved via a capping method. In this method, tetraoctylammonium cations selectively cap the {111} facets, while Br⁻ ions protect the {100} facets. The exposed facets are oxidized by O₂/Cl⁻, producing a variety of interesting geometries. Facet selective etching of Au microcrystallites is governed only by the nature of the facets as geometry does not seem to play any significant role. Etched surfaces appear rough but a closer examination reveals well-defined corrugations indexable to high *hkl* values. Such surfaces exhibit enhanced Raman activity.

3.1 Introduction

The crystal lattices of most metals are FCC (face centered cube), which is highly symmetrical. Due to the large number of equal symmetry directions and facets, anisotropic etching is not easily attainable in FCC metals particularly in noble metals. While anisotropic etching is well known among low symmetry semiconducting materials such as Si (1), Ge (2) and GaN (3) etc., there are hardly any reports on metal crystals. In this study, anisotropic etching of Au microcrystals has been explored. There are few reports on anisotropic etching of nanoparticles of noble metals. Etching of a nanoparticle facet is dependent on its surface energy (γ) and the general trend is $\gamma_{(110)} > \gamma_{(100)} > \gamma_{(111)}$ (4). Hence, it is expected that the {110}, {100} and {111} facets show high, medium and low reactivities with a given etchant. However, there are counter effects due to the polarization (5), symmetry (6) and other parameters of adsorbed species, which manoeuvre the facet selective etching of metal crystallites. For an instance, Br⁻ anions bind preferentially to {100} facets (7), while quaternary cations bind to {111} facets (8). Etching of a

facet is a combined effect of surface energy and the nature of the adsorbed species and in the absence of counter effects, etching proceeds in accordance with the surface energy. However, this often leads to irregular geometries. The capping agent lowers etchant interaction considerably with the adsorbent facets (9). The strength of etchant also plays an important role in guiding anisotropic etching. While isotropic etching takes place with a strong etchant (eg., HNO_3), no etching can occur if the etchant is too weak. Commonly used mild etchants for noble and semi-noble metals are H_2O_2 (10), CN^- (11), Fe(III) (12), Cu(II) (13, 14), Pb(II) (15), NH_3 (16) and O_2/Cl^- (7). For instance, Pd cuboctahedrons and octahedrons have been obtained from nanocubes by selective etching along the [111] direction using O_2/Cl^- as etchant, while Br^- ions protected the {100} facets (7, 17). In another case, Yang et al. have obtained a variety of geometries from Ag octahedron by selectively etching the [100] facets using $\text{NH}_4\text{OH}/\text{H}_2\text{O}_2$, with PVP as the capping agent (16). The above studies have produced interesting nanoparticle geometries without significantly altering the size. Unlike Ag and Pd, etching of Au nanoparticles is not easy because of its noble character. Jana et al. (18) have reported the anisotropic etching of Au spheroid to spherical nanoparticles using CN^- . Electrochemical oxidation to Au crystals also has been reported (19, 20). Pradeep et al. have used CuCl_2 as an etchant for the anisotropic etching of Au nanorods, and selective etching of body and tip of the nanorods have been demonstrated (21). Au nanorods were oxidized to spherical nanoparticles using H_2O_2 (22, 23). Yet, the nature of the etched facets and the mechanism seem unclear. All above examples pertain to particles with size well below 300 nm. Recently Fan et al. have reported a versatile method for the selective etching of edges and {111} facets of various shaped Au nanocrystals (24). Face selective etching is indeed interesting not only to understand the nature of the facets but also to produce various shapes with nearly same size. Since anisotropic etching does not alter the size of the nanoparticles, the obtained nanoparticles with different shapes are the ideal systems to study shape dependent properties.

It is interesting to examine anisotropic etching behavior of Au microcrystals in the form of Au polygonal plates grown in the laboratory as these are essentially single crystalline with well-defined facets (25, 26). An advantage is that facet selective etching of the microplates and the crystallographic details of the etched facets can be visualized under commonly used optical and electron microscopes unlike nanoparticles which require high resolution TEM (27). Indeed, successful demonstration on large metal crystallites has not been reported hitherto. Although

such studies are possible on bulk crystal surfaces, facet selectivity is found to be rather poor due to inherent surface defects and dislocations (28). Specifically, this chapter deals with the systematic study of selective etching of {100} and {111} facets of various types of Au microcrystals namely cuboctahedron, hexagons, triangles and pentagonal microrods, using Ag(I) and Cu(II) based etchants. The selective etching has produced a variety of intermediates enclosed with highly corrugated surfaces, indexable to high *hkl* values.

Table 3.1 Summary of literature showing the conditions have been adopted for Au nanoparticles etching

S. No	Etchant	Shape of the Au particle	Type of etching	Nature of the obtained facet	Ref
1	KI and H ₂ PtCl ₆	Octahedron, decahedron, nanorod, and nanoplates (>150 nm)	Selective etching of edge, followed by {111} etching	High index facets	(24)
2	Dopamine	13 nm, spherical nanoparticles	Reduction of Particle diameter reported.	----	(29)
3	KSCN, H ₂ O ₂ and Co ²⁺	Nanorods	Preferential etching along the longitudinal direction	----	(30)
4	Cu(II) salts, H ₂ SO ₄ and H ₂ O ₂	Nanorods	Etching along the longitudinal direction	----	(14)
5	FeCl ₃	Nanorods	Etching along the longitudinal direction ({111} facets might be etched)	----	(12)

6	H ₂ O ₂ and Br ⁻	Nanorods	Etching along the longitudinal direction	----	(23)
7	H ₂ O ₂ , HCl and CTABr	GNRs, bipyramids (BPs) and prisms	Shortening along longitudinal directions	----	(31)
8	NO ₂ ⁻	Nanorods (< 50 nm)	Preferential shortening along the axial direction	----	(32)
9	S ₂ O ₃ ²⁻ and Pb ²⁺	Nanorods	Shortening along the axial direction	----	(33)
10	Cr (VI)	Nanorods	Shortening along the axial direction	----	(34)
11	Cu(II) and HBr	Nanorods	Preferentially along the longitudinal direction	----	(35)
12	Cholesterol	gold nanoparticles	No discussion	----	(36)
13	HNO ₃	Gold nanoparticles	No discussion	----	(37)
14	CuCl ₂	Nanorods	Body and tip	----	(21)
15	sodium dodecylbenzenesulfonate	Au plates	No defined etching on {111} facets	----	(38)
16	KCN	Nanorods	No discussion	----	(39)
17	Au(III)-CTAB Complexes	Nanorods, Irregular Nanoparticles	Shortening of size	----	(11)
18	H ₂ O ₂	Bipyramids	Shortening along the axial direction	----	(10)
19	HCl and O ₂	Nanorods	Shortening along the axial direction	----	(22)
20	KCN and O ₂	Nanorods and bipyramids	Shortening along the axial direction	----	(18)
21	H ₂ O ₂	Nanorods	Shortening along the axial direction	----	(40)
22	HAuCl ₄	Au disks	Etching corners	----	(41)

23	HAuCl ₄ and CTAB	Nanorods	Transverse etching of GNRs	----	(42)
24	H ₂ O ₂ , HCl and CTAB	Nanorods	Transverse etching of GNRs	----	(43)
25	HAuCl ₄ and CTAB	Au triangular prisms	Etching of sharp tips	----	(44)
26	Anodic dissolution	Single crystalline Au(111) electrode	Dissolution of (111) planes	Kinks	(19)
27	Electro chemical etching	Micron size Au plates	Dissolution of (111) planes, etching in vertical direction about 40 nm	----	(20)
28	Na ₂ S ₂ O ₃ , Pb(II)	Au spherical nanoparticles	Size reduction	----	(15)
29	NH ₃ -NH ₄ Cl and Cu(II)	Nanorods	Shortening along the axial direction	----	(13)
30	NH ₃ -NH ₄ Cl and Cu(II)	Au spherical nanoparticles, 15 nm	Shortening of diameter	----	(45)

3.2 Scope of the present investigation

The noble character of Au in the high symmetry crystal structure makes it nearly impossible to attain anisotropic etching. For the first time, facet selective etching of {100} and {111} facets has been achieved by a specialized capping method. The etching process is found dependent on the atomic arrangement of the planar surfaces rather than the shape of Au microcrystallites.

3.3 Experimental Section

3.3.1 Materials

Gold chloride (HAuCl₄), silver nitrate (AgNO₃), tetraoctylammonium Bromide (ToABr), cupric chloride (CuCl₂), sodium chloride (NaCl), copper sulphate (CuSO₄) and toluene were used. All

reagents were purchased from spectrochem, India. Water used in this study was double distilled and deionized. Si substrates were cleaned with water, IPA, toluene and dried under N₂ gas.

3.3.2 Synthesis of Au microcrystals

To a 75 μL of H₂AuCl₄ (25 mM), 100 μL of ToABr in toluene (50 mM) was added and stirred for 5 min (25). The bottom aqueous phase became colorless and top organic phase developed red color. The obtained AuToABr complex has nearly the same melting point (~ 90 °C) and decomposition temperature (~ 150 °C) as ToABr. The organic layer was pipetted out, drop coated on a Si substrate and heated at 135 °C on a hot plate in air. After growing Au microcrystals, they were washed with toluene to remove any residual precursor and dried with flowing nitrogen.

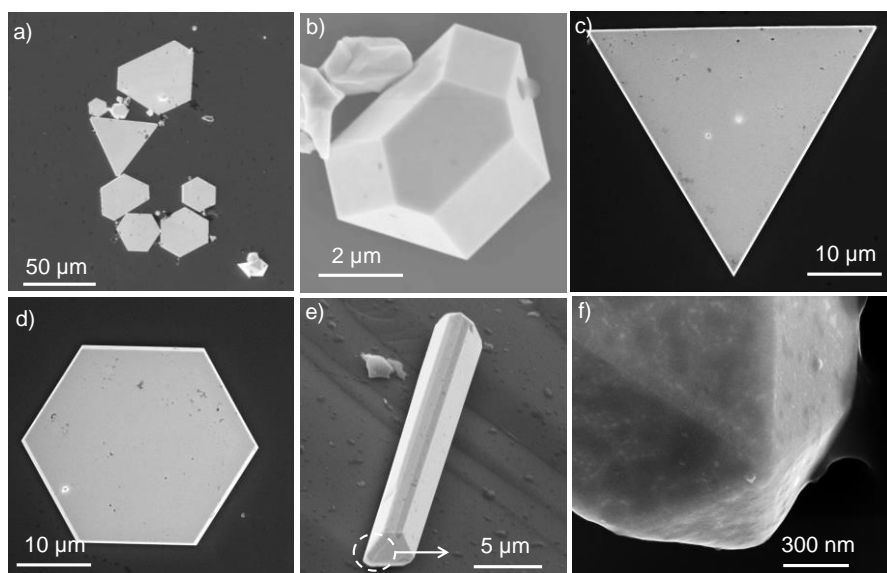


Figure 3.1 SEM images of Au microcrystallites of different shapes.

3.3.3 Preparation of AgToABr for the {100} facets etching

To a 200 μL of ToABr (50 mM) solution, 25 μL of AgNO₃ (25 mM) solution and 10 μL of HCl (110 mM) were added and stirred for 5 minutes (46). It may be noted that ToABr is in excess amount to ensure effective phase transfer of Ag(I) to the organic layer. The obtained AgToABr complex was characterized using FTIR, TGA and EDS measurements (see Fig. 3.2). The melting point and decomposition of the obtained AgToABr is nearly the same as ToABr and AuToABr.

A 200 μL of organic layer was taken out and drop coated on as prepared Au microcrystals, heated at 135 $^{\circ}\text{C}$ on a hot plate in air for 6h. Samples were washed with toluene to remove the unreacted precursor and dried under N_2 gas.

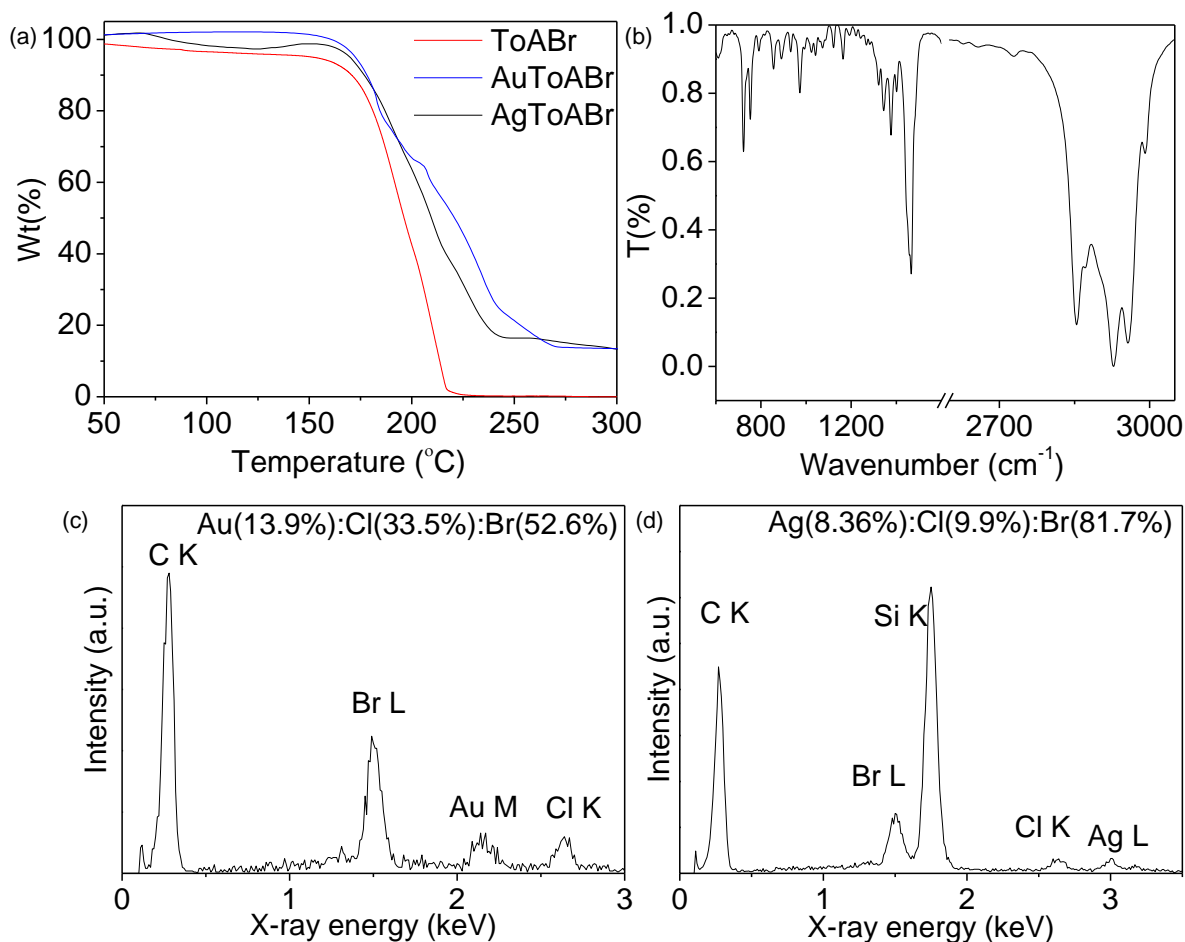


Figure 3.2 (a) TGA of ToABr, AuToABr and AgToABr complex. (b) FTIR spectrum of AgToABr. EDS spectra collected from (c) AuToABr and (d) AgToABr films. IR bands at 2954, 2927, 2872 and 2853 cm^{-1} indicate the asym. CH_3 stretch, asymm. CH_2 stretch, symm. CH_3 stretch and symm. CH_2 stretch modes of alkyl groups in ToA^+ cation.

3.3.4 Etching of the {111} facets

Au microcrystallites were dipped in 1 mL of 0.5 M CuCl_2 solution, heated at 60 $^{\circ}\text{C}$ in air. After 1 h, the solution was cooled down to room temperature. Samples were taken out, washed with plenty of water, dried under N_2 gas and used for characterization.

3.3.5 Characterizations

Scanning electron microscopy (SEM) was performed using a Nova NanoSEM 600 equipment (FEI Co., The Netherlands). Energy dispersive spectroscopic (EDS) mapping was performed using EDAX Genesis V4.52 (USA) attached to the SEM column. Atomic force microscopy (AFM) experiments were carried out using Bruker diInnova Scanning Probe Microscope with Nanodrives controller. Imaging has been done in tapping Mode. Thermogravimetric analysis (TGA) was carried out using a Mettler Toledo, TG-850 in N₂ atmosphere.

3.4. Results and Discussion

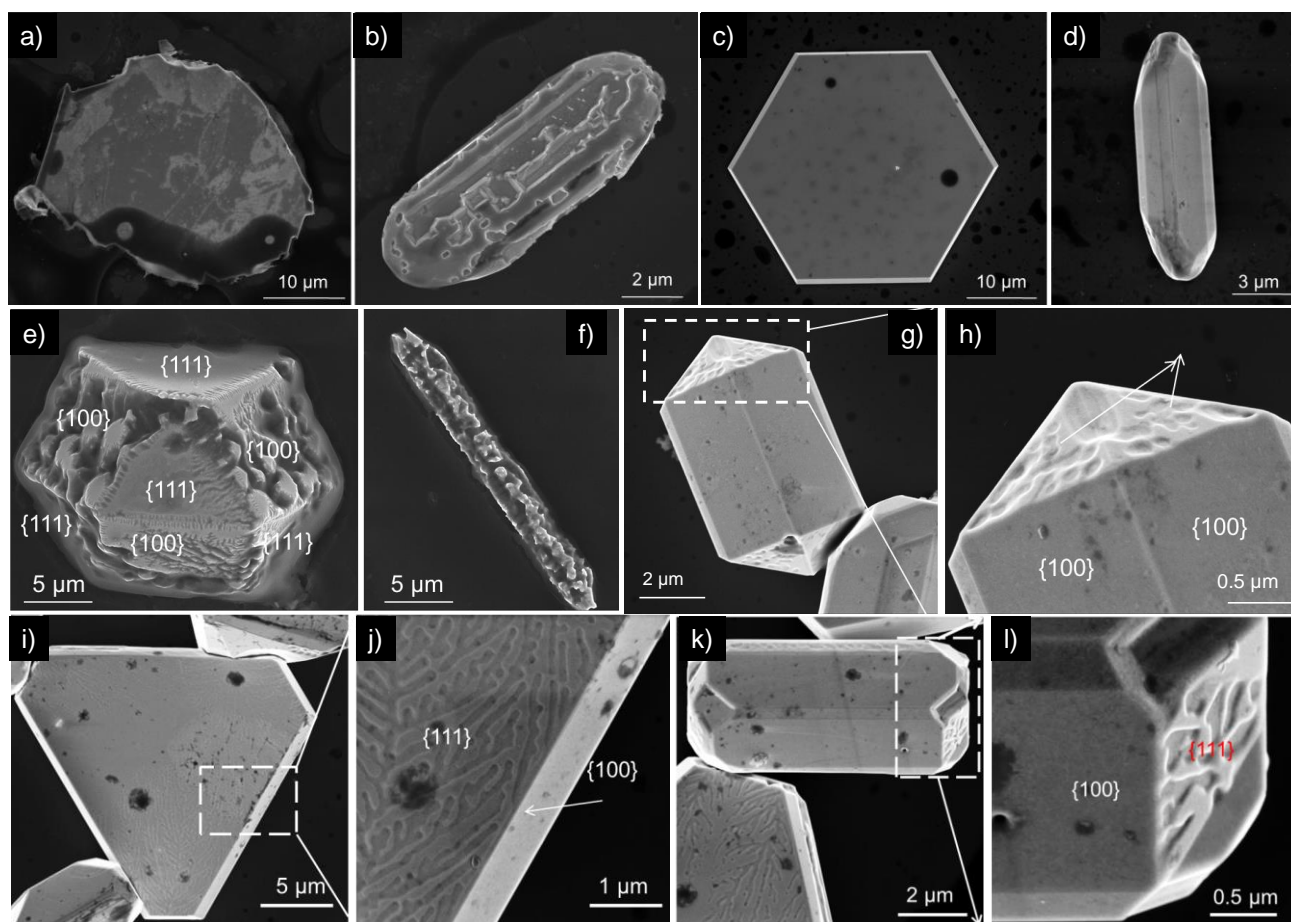


Figure 3.3 SEM images of Au microcrystals treated with 0.5 M FeCl₃ (a, b), H₂O₂ (c, d) ToABr (e, f) and NaCl (g-l).

3.4.1 Etching of {100} facets

Au microcrystals were prepared using a method reported from this laboratory recently (25). In a typical synthesis of Au microcrystals, 100 μL of precursor obtained by the stabilization of $(\text{AuCl}_4)^-$ with ToABr was drop coated on a Si substrate and thermalized on a hotplate at 135 $^\circ\text{C}$ in air for 1 hour. At this thermolysis temperature, the growth of Au microcrystals proceeds in the molten state of the precursor (AuToABr), while the decomposition starts at ~ 150 $^\circ\text{C}$ (see Fig. 3.2). In the obtained product, two types of Au microcrystals were observed, namely cuboctahedron derivatives and the penta-twinned microrods though the latter were less in abundance. In the first category, in addition to regular cuboctahedron, other analogous geometries- truncated octahedrons (10), hexagons and triangles, were also present (Fig. 3.1). The crystallite size is in the range of 1-10 μm . Among them, regular cuboctahedron is of our interest in this study. It is enclosed with 14 facets among which eight are triangular and six are rectangular or square facets. In the given conformation of a cuboctahedron shown in Fig. 3.4(a), the top and bottom faces are made of triangles, and the side facets are enclosed with alternative six triangular and six rectangular or square facets (47, 48). A typical view of cuboctahedron particle is depicted in Fig. 3.4(a), where four triangular and three-square facets are seen clearly, which are assigned to $\{111\}$ and $\{100\}$ facets respectively (47). The edges are sharp and the surface of each face is smooth as evident from Fig. 3.4(b). To achieve anisotropic etching, various etchants like FeCl_3 , NaCl , H_2O_2 , ToABr and AgToABr were tried out. However, poor anisotropic etching was observed with FeCl_3 , NaCl , H_2O_2 and ToABr (see Fig. 3.3), while facet selective etching was attained with AgToABr . Briefly, to the obtained microcrystals, ~ 200 μL of the etching solution, AgToABr in toluene (see experimental section for the preparation), was added and thermolysis was continued at 135 $^\circ\text{C}$.

The etching of the $\{100\}$ facets took place in molten AgToABr . The products obtained at various stages of thermolysis were analyzed. SEM image of a cuboctahedron obtained after 1h of thermolysis is shown in Fig. 3.4(c). Interestingly, all $\{100\}$ facets got etched to roughened surfaces, whereas the $\{111\}$ facets are seen unaffected which is quite evident in the magnified image shown in Figs. 3.4(d-f). This observation confirms selective etching of the $\{100\}$ facets by AgToABr . In addition, the edges and corners also become roughened (Figs. 3.4(d-f)). It may be

recalled that selective etching of $\{100\}$ facet has been studied in the case of Ag (16) and Pd nanocrystals (7), but there is no such example known in the case of Au.

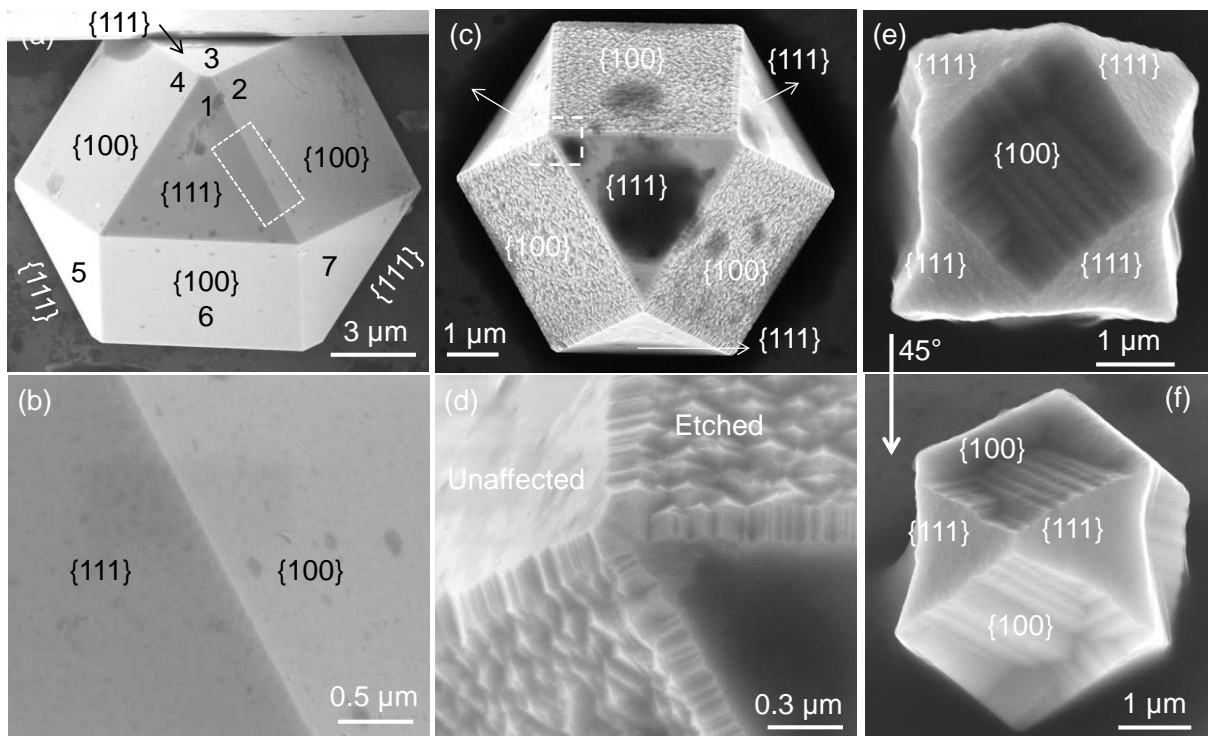


Figure 3.4 Typical SEM images of (a-b) as prepared and (c-d) after treated with AgToABr for selective etching of $\{100\}$ facets. (e, f) SEM images of an etched cubo-octahedron collected on tilting the stage by 0 and 45° .

Continued etching of $\{100\}$ facet produced concave type deepening as shown in Fig. 3.5(a); however, it disappeared during further etching, due to the thermodynamical instability (27). It appears that as the $\{100\}$ facets were gradually etched, a variety of intermediates formed with the $\{111\}$ facets unaffected (Figs. 3.5(a, b)). However on extended etching, the $\{111\}$ facets shrunk in area, and eventually disappeared in the final stage (Fig. 3.5(f)). The Au microcrystals obtained at intermediates stages exhibit two types of roughened surfaces indicated as RS1 and RS2 in Fig. 3.5b. Etching along the $[100]$ direction produced RS1, while the corrugated surfaces formed at the interface of $\{111\}$ and $\{100\}$ facets gave rise to RS2, parallel to the top/bottom $\{111\}$ facets. The surface morphology is quite different in that well defined corrugated steps are present in RS2 (Fig. 3.5(c)) while interconnected streak-like topography is observed on RS1. The

latter correspond to mini {110} facets as the angle between two adjacent mini facets is either 60° or 120° (Fig. 3.5(d)) (49).

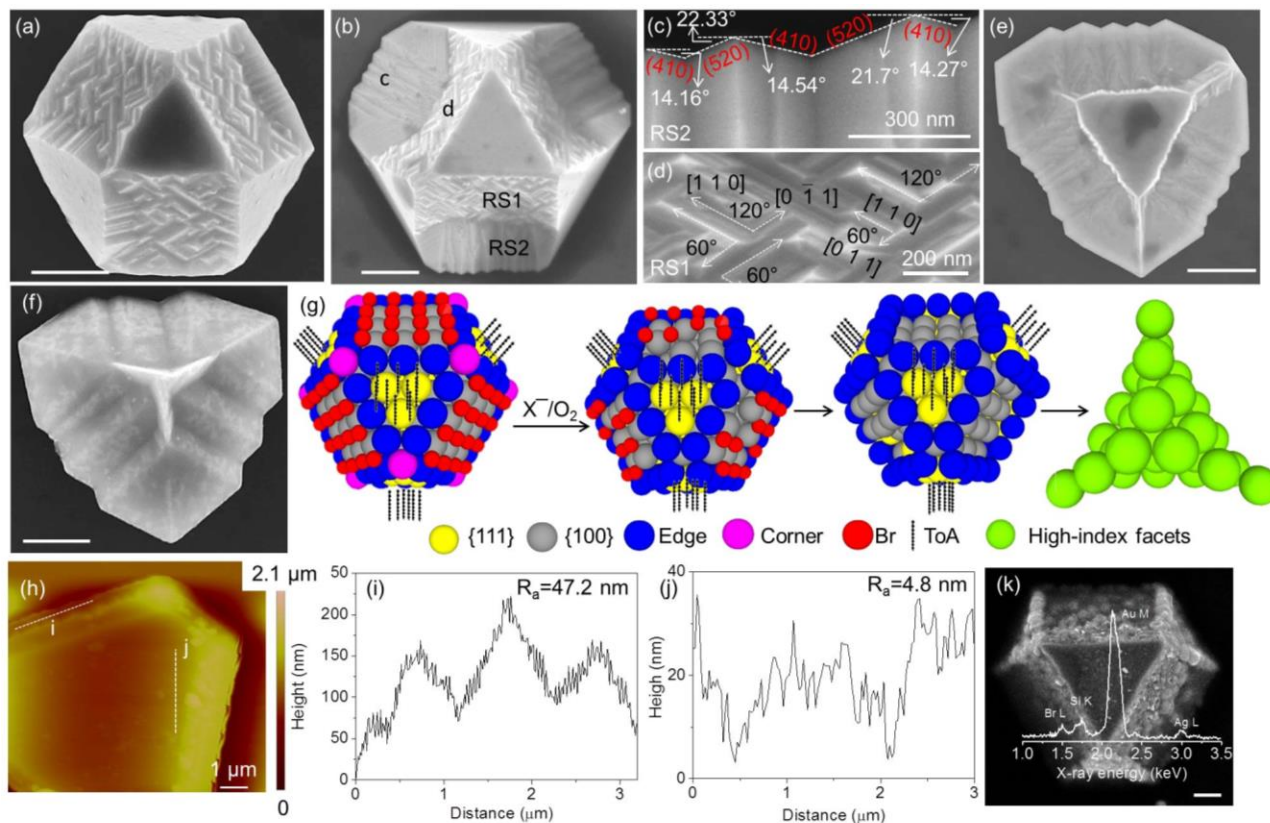
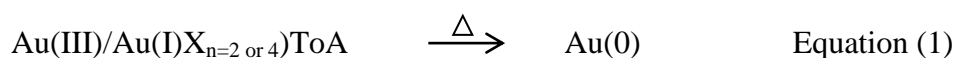


Figure 3.5 (a-f) SEM images of Au cuboctahedrons at various stages of {100} facet etching. (g) Schematic illustrating selective etching of the {100} facet. (h) AFM topography of Au microcrystals. (i-j) Height profiles along the lines drawn in h. The average roughness on etched {100} and unetched {111} facets are 47.2 and 4.8 nm respectively. (k) SEM image Au cuboctahedron after treated with AgToABr in Ar atmosphere. The corresponding EDS spectrum is shown on the top of the image k. Scale bar, 1 μm .

In case of RS2, there are two sets of angles between the pristine {100} facet and the corrugated features, namely $14.34 \pm 0.20^\circ$ and $22.0 \pm 0.3^\circ$ (see Fig. 3.5(c)) which going by the calculated angles of 14.04° and 21.8° , should correspond to {410} and {520} facets respectively (50). It is interesting that etching of {100} facet can lead to such high index facets. As etching progresses along the [100] direction, the extent of RS1 diminished (Fig. 3.5(e)), and completely disappeared in the final product. As depicted in Fig. 3.5(f), the surface of the microcrystals is covered with

only RS2 type surface. Due to the preferential etching on {100} facet, the surface roughness of {100} facet is ~ 10 times higher than the {111} facets and the heights of the corrugated steps are in the range of ~ 50-150 nm (see AFM data in Figs. 3.5(h-i)). A continued etching resulted in the formation of trigonal bipyramids covered with corrugated surfaces (Figs. 3.5(f) and (g)). The etching mechanism is proposed based on the above experimental observations, drawing some clues from the literature examples of anisotropic etching of Pd nanocubes (7) and Ag octahedrons (16). The selective etching of Au{100} facets involves four major steps. 1) Adsorption of tetraoctylammonium cation (ToA⁺) on the {111} facets. 2) Oxidation of atoms present at corners and edges. 3) Etching of {100} facets. 4) Redeposition of Au(III) or Au(I) on the etched {100} facets. The ToA⁺ ion preferentially adsorbs on the {111} facets due to the higher adsorption energy (8). To validate that Au{111} facets are covered with ToA⁺ cations, Au microcrystals obtained from AuToABr were partially washed and SEM imaging was performed. Au{111} facets are seen covered with a thin organic layer (Fig. 3.6(a-c)). EDS spectrum collected from the Au{111} consists of a weak carbon signal which may attributed to the ToA⁺ ligands adsorbed on the {111} surface. No detectable Br⁻ is seen EDS spectrum collected from Au{111} facets (Fig. 3.6(d)). Interestingly, SEM images reveal that the carbonaceous species is much less on Au{100} facets (see Fig. 3.6(b)), which enables selective etching. The long alkyl chain of ToA⁺ projects away from the Au{111} surface and makes it hydrophobic (51). Hence, the polar etchant like O₂/Br⁻ may not able to attack the {111} facets. In addition, higher surface energy of the Au{100} facet also facilitates selective etching of the {100} facet (4). Atmospheric oxygen in combination with the halide anion available in the reaction medium can etch gold to form soluble Au(I) or Au(III) complexes such as (AuX₂)ToA (Au is in +1 state) and (AuX₄)ToA (Au is in +3 state). Etching of {100} facets begins at the corners due to the high reactivity arising out of low coordination number and low bromide coverage (7). As this process continues, the atoms on the {100} facets are etched away involving the removal of Br⁻ ions from the {100} facets (see schematic in Fig. 3.5(g)). Etching of the {100} produces high index facets which are more reactive compared to the low index facets. The newly generated Au(III) or Au(I) complexes get reduced to Au(0) due to the thermal reduction, and deposits on the high-index facets (eq. 1).



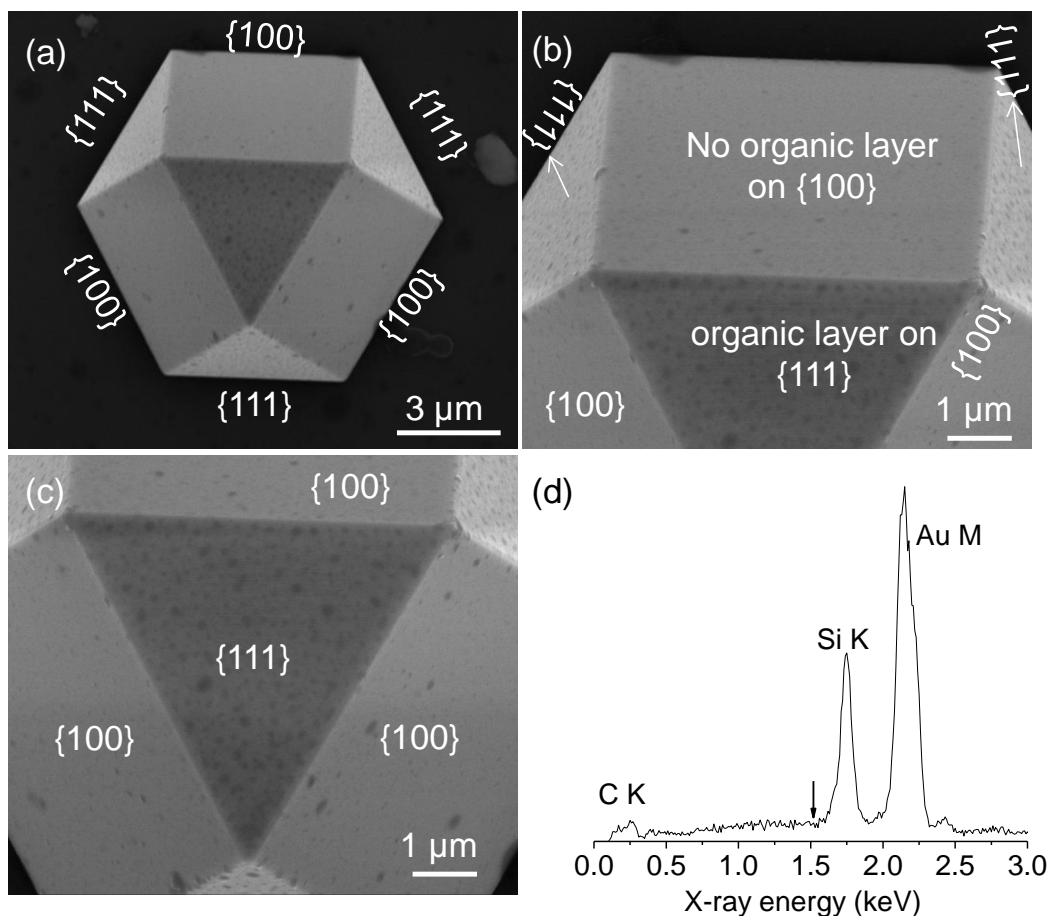
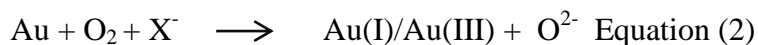


Figure 3.6 (a-c) SEM images of Au cuboctahedron are depicting the residual organic islands on Au{111} facets. (d) EDS spectrum collected from the Au{111} facet, arrow indicates the expected position of Br L signal.

As described in our earlier work (52, 53), Ag(I) from AgToABr tends to deposit selectively on the Au{100} facets due to the under potential deposition (UPD) to form a monolayer or sub-monolayer of Ag(0). The Ag monolayer stabilizes the high index facets (54). However, the nature of adsorption sites is still unclear. In the absence of Ag(I) (etching with ToABr alone), the etched surface is found rather irregular (see Fig. 3.3). To examine the role of atmospheric oxygen in the etching process, thermolysis was carried out in Ar atmosphere. No etching took place and instead the thermolysis led to the formation of AgBr crystallites (55). Thus, AgBr got deposited on the cuboctahedrons, which is evident from the EDS spectrum shown in Fig. 3.5(k). From the above set of experiments, the plausible equation of Au etching is as follows.



3.4.2 Etching of {111} facets

Similarly, etching of {111} facets has been tried out using a different but specific etchant.

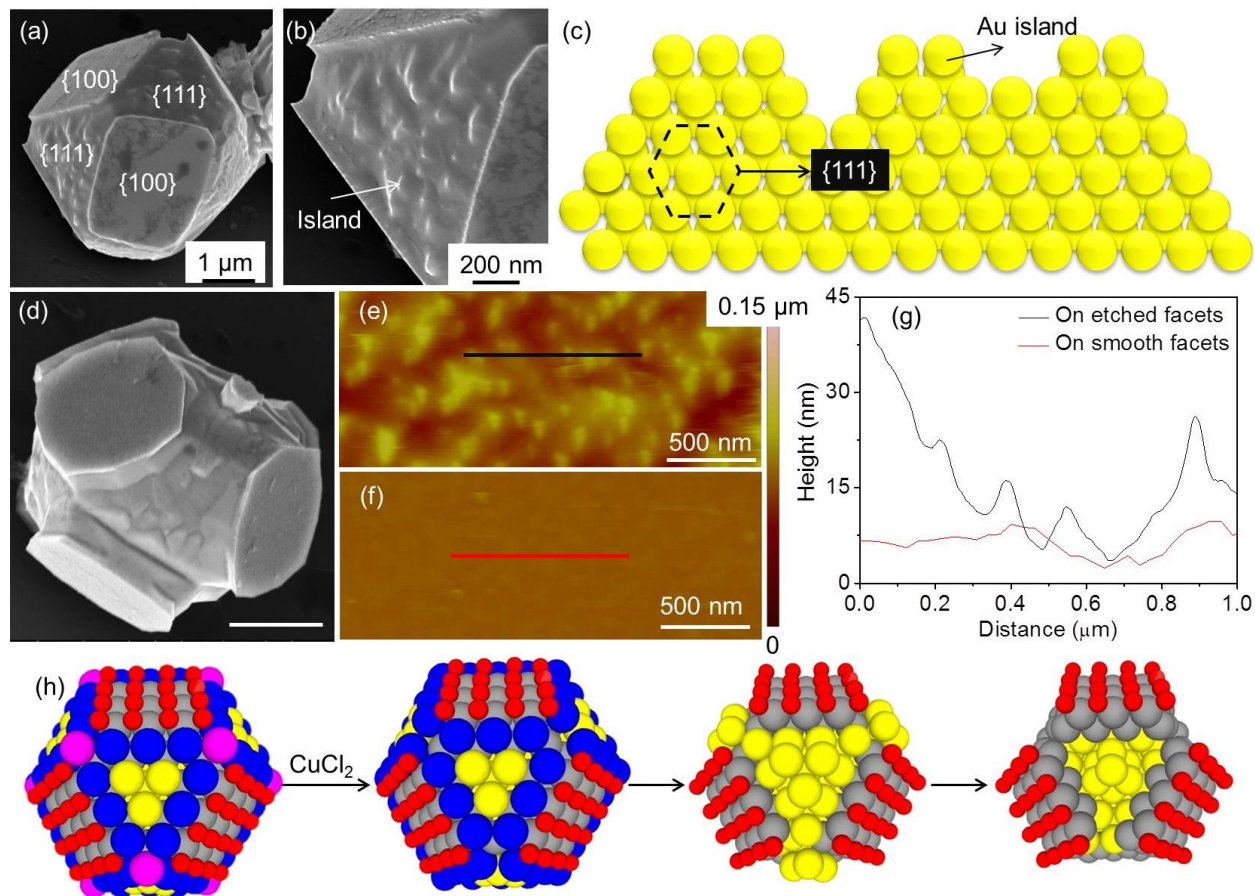


Figure 3.7 (a-b) SEM images of cuboctahedron obtained after treatment with 0.5 M CuCl₂. (c) Schematic illustration of islands formed from {111} facets. (d) SEM images of a hexapod obtained by the selective etching of Au{111} facets. (e-f) AFM topography images collected from various regions of a cuboctahedron. (g) Height profiles along the lines drawn in e and f. (h) Plausible etching mechanism of {111} facets.

Fresh Au microcrystals were immersed in 1 mL of 0.5 M CuCl₂ solution held at 60 °C and the morphological changes were examined (Fig. 3.7). Contrary to the {100} etching, in this case, triangular {111} facets got etched while {100} facets were intact (Fig. 3.7(a)). The magnified image in Fig. 3.7(b) shows randomly distributed islands formed due to etching of the {111} facets which is schematically illustrated in Fig. 3.7(c). Unlike Au{100} etching, selective etching

of the $\{111\}$ facets did not produce corrugated facets. Etching of Au cuboctahedron along the $\{111\}$ facets produced a set of intermediate geometries and the final product was a hexapod (Fig. 3.7(d)). In order to understand the etching process and to identify the active etchant species, a set of experiments were tried out. First, oxygen dissolved in CuCl_2 solution was removed by adding Na_2SO_3 which is O_2 scavenger (21). Etching was then carried out with this solution and interestingly, no noticeable etching was observed even after 12 h (see Fig. 3.8).

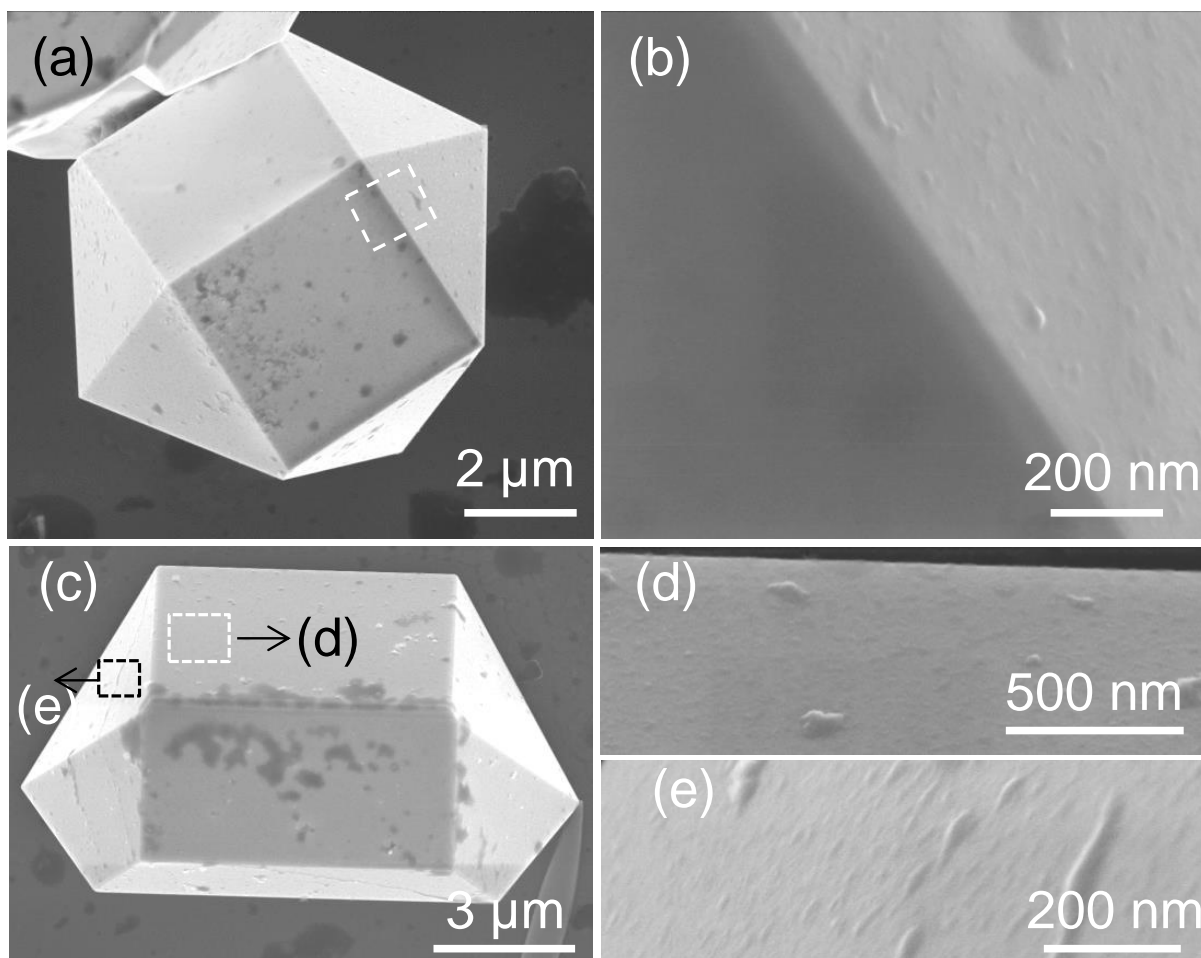


Figure 3.8 SEM images of cuboctahedrons treated in (a-b) mixture of CuCl_2 and Na_2SO_3 . (c-e) Etching in 0.5 M CuSO_4 solution, all other conditions being the same.

This experimental observation reconfirms that oxygen is indeed essential for etching of Au surfaces. To address the role of Cl^- , CuSO_4 was used instead of CuCl_2 , and in this case too, no significant etching was observed (see Fig. 3.8). Similarly, the $\{111\}$ facets etching was performed with NaCl instead of CuCl_2 . Although the etching is observed on the $\{111\}$ facets, the

extent of etching was relatively less under the experimental conditions employed (see Fig. 3.3). It produced interesting dendrimeric etched patterns, which may deserve a separate study. The milder action of Na^+ is mainly due to its highly negative reduction potential (-2.71 eV). Cu(II) , on the other hand, acts as a catalyst for the production of intermediates such as superoxide (O_2^-) that etches the Au surface (30). From the above two experiments, it is clear that Cu(II) , Cl^- and O_2 are the active components of the etchant. It appears that the quaternary salts adsorbed on $\{111\}$ facets of Au microcrystals (obtained from AuToABr) get removed during toluene washing due to the high solubility of the ToABr in toluene (380 g/L) (56), while Br^- may remain intact on $\{100\}$ facets due to poor solubility in toluene. Hence the $\{111\}$ facets are easily accessible for the etchant which is devoid of the capping agent. As in $\{100\}$ etching, here too etching commenced at the corner and proceeded along the edges (see schematic Fig. 3.7(h)). The islands formed due to the $\{111\}$ etching are separated by ~ 100 nm and the average height of islands is ~ 10 nm (Figs. 3.7(e) and (g)). As the etching progressed, the roughness of $\{111\}$ etched facets (Fig. 3.7(e)) increases by an order compared to $\{100\}$ facets (see AFM data in Figs 3.7(e-g)).

As mentioned previously besides cuboctahedrons, several other geometries such as truncated octahedrons, hexagonal plates, triangles and pentagonal nanowires have also been observed (Fig. 3.9). In these cases as well, the facets are smooth with well-defined edges and corners prior to etching (Figs. 3.9(a-c), (h) and (m)). Similar to cuboctahedrons, cuboctahedron derivatives also exhibit selective etching of $\{100\}$ facets with AgToABr (Figs. 3.9(d-f), (i-k) and (n-p)). Continued etching along the $[100]$ direction has led to the formation of trigonal bipyramidal microcrystals covered with corrugated surfaces. In the case of Au nanowires, the selective etching of $\{100\}$ facets produced corrugated pentagonal nanowires (Figs. 3.9(n-o)). However, the tips of $\{111\}$ are unaffected by the etchant (Fig. 3.9(p)). On the other hand, selective etching of $\{111\}$ facet is observed with CuCl_2 (Figs. 3.9(g, l) and (q-s)). It is noteworthy that the anisotropic etching of Au $\{100\}$ and Au $\{111\}$ facets is purely facet selective independent of the geometry of the Au microcrystals and size. The process is substantiated by growing Au crystals of ~ 300 nm and etching the $\{100\}$ and $\{111\}$ facets using AgToABr and CuCl_2 respectively (see Fig. 3.10). The process should be applicable to even smaller sizes though imaging becomes more involved.

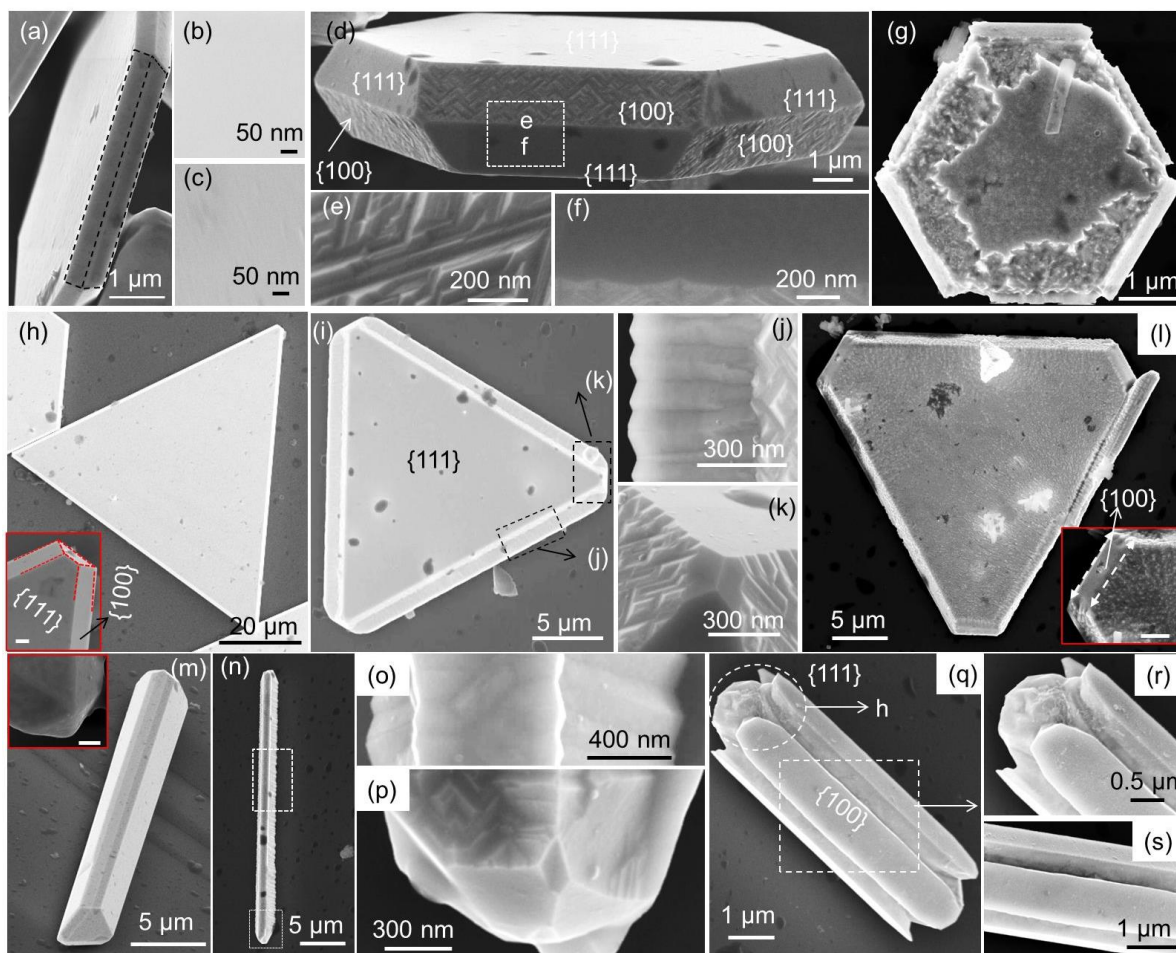


Figure 3.9 SEM images of Au hexagons, triangles and microrods before etching (a-c, h and m), after selective $\{100\}$ etching (d-f, i-k and n-p) and after $\{111\}$ etching (g, l and q-s) respectively. Scale bar is 300 nm, where not mentioned.

With this study involving large microcrystals, the finer steps involved during etching are made clear and the surface crystallography of the etched facet is also evident. As shown in the above cases, all the intermediate stages of selective etching of Au microcrystals were identified using an ordinary electron microscopy that is simply not possible with nanoparticles due to their small dimensions. These larger dimensions are handy and attractive not only in the context of the facet selective etching phenomenon but also because of the emergence of crystallographically well-defined nanocorrugated surfaces over large areas.

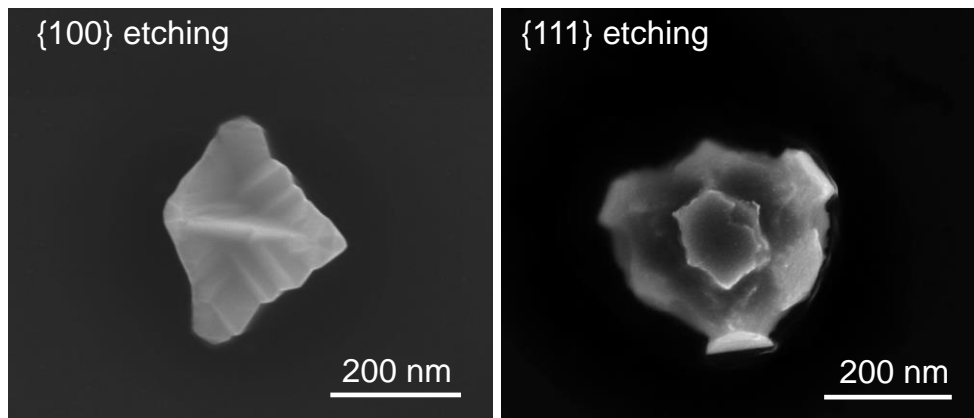


Figure 3.10 SEM images of submicron size Au crystals after {100} and {111} etching.

For instance, selective etching of {100} facet of penta-twinned microrods has produced nanocorrugated Au microrods, while there are no changes in the length of rods. Usually, such corrugated nanowires are obtained only using sophisticated lithography techniques (57). To the best of our knowledge, it is the first report that has successfully demonstrated anisotropic etching of Au microcrystals. A nanocorrugated surface can be interesting with regard to surface plasmon polaritons and their interaction with light (see Fig. 3.11) (58). In the literature, facet selective etching of Metals is known only for {100} facets of Ag and Pd nanocrystals.

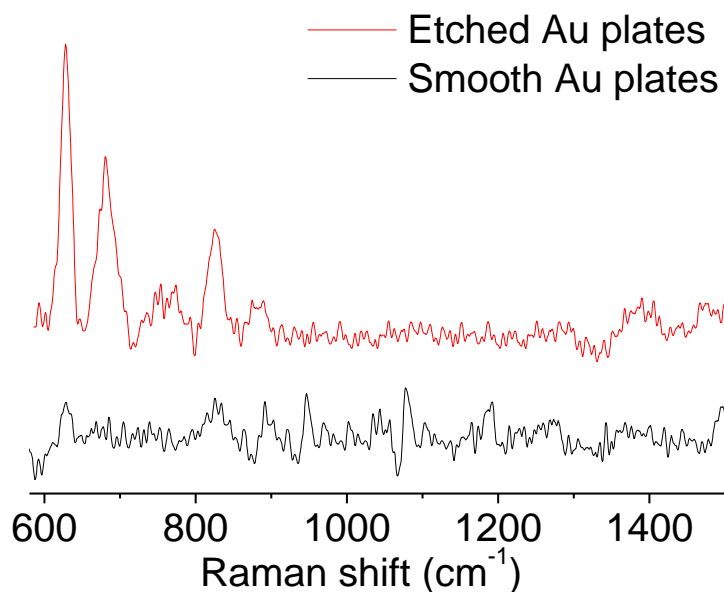


Figure 3.11 SERS spectrum of R6G collected from smooth and etched plates.

3.5 Conclusion

This study, for the first time, has dealt with anisotropic etching of Au that too in the form of microcrystals. Specific geometries belong to cuboctahedron, truncated octahedron, hexagon, triangle and pentagonal rod, all in the range of few tens of microns enclosed with {111} and {100} facets. Gold etching is done by atmospheric O₂ in presence of halides. Selective etching of {100} facets took place as ToA⁺ ions present in the reaction medium selectively capped the {111} facets. Similarly, the {100} facets were protected by the adsorbed Br⁻ ions while {111} facets were etched. Trigonal bipyramids and hexapods are the final products obtained by the selective etching of {100} and {111} facets respectively. In both cases, etching initiated at the corners, and then spread towards the edges. Complete etching produced corrugated facets that have been assigned to high index facets. Anisotropic etching of microcrystals is remarkable not only for producing various interesting shapes but also for creating high index facets over large surface area (~ hundreds of μm²). More importantly, it is observed that the selective etching was dependent only on the crystallography of the facets and not on the specific geometry of the microcrystal. Due to the nanocorrugations, etched surfaces exhibited enhanced Raman signal of an analyte while no enhancement was observed from the smooth surfaces.

References

1. H. Seidel, L. Csepregi, A. Heuberger, H. Baumgärtel, *J Electrochem Soc* **137**, 3612-3626 (1990).
2. R. Leancu, N. Moldovan, L. Csepregi, W. Lang, *Sensor Actuat A: Phys* **46**, 35-37 (1995).
3. H. M. Ng, N. G. Weimann, A. Chowdhury, *J Appl Phys* **94**, 650-653 (2003).
4. C. Kan, C. Wang, H. Li, J. Qi, J. Zhu, Z. Li, D. Shi, *Small* **6**, 1768-1775 (2010).
5. O. M. Magnussen, *Chem Rev* **102**, 679-726 (2002).
6. D. S. Kilin, O. V. Prezhdo, Y. Xia, *Chem Phys Lett* **458**, 113-116 (2008).
7. M. Liu, Y. Zheng, L. Zhang, L. Guo, Y. Xia, *J Am Chem Soc* **135**, 11752-11755 (2013).
8. S. K. Meena, M. Sulpizi, *Langmuir* **29**, 14954-14961 (2013).
9. R. Long, S. Zhou, B. J. Wiley, Y. Xiong, *Chem Soc Rev* **43**, 6288-6310 (2014).
10. X. Kou, W. Ni, C.-K. Tsung, K. Chan, H.-Q. Lin, G. D. Stucky, J. Wang, *Small* **3**, 2103-2113 (2007).

11. J. Rodríguez-Fernández, J. Pérez-Juste, P. Mulvaney, L. M. Liz-Marzán, *J Phys Chem B* **109**, 14257-14261 (2005).
12. R. Zou, X. Guo, J. Yang, D. Li, F. Peng, L. Zhang, H. Wang, H. Yu, *CrystEngComm* **11**, 2797-2803 (2009).
13. Z. Chen, R. Liu, S. Wang, C. Qu, L. Chen, Z. Wang, *RSC Adv* **3**, 13318-13323 (2013).
14. T. Wen, H. Zhang, X. Tang, W. Chu, W. Liu, Y. Ji, Z. Hu, S. Hou, X. Hu, X. Wu, *J Phys Chem C* **117**, 25769-25777 (2013).
15. D. Dai, D. Xu, X. Cheng, Y. He, *Anal Meth* **6**, 4507-4511 (2014).
16. M. J. Mulvihill, X. Y. Ling, J. Henzie, P. Yang, *J Am Chem Soc* **132**, 268-274 (2010).
17. J. Zhang, C. Feng, Y. Deng, L. Liu, Y. Wu, B. Shen, C. Zhong, W. Hu, *Chem Mater* **26**, 1213-1218 (2014).
18. N. R. Jana, L. Gearheart, S. O. Obare, C. J. Murphy, *Langmuir* **18**, 922-927 (2002).
19. S. Ye, C. Ishibashi, K. Uosaki, *Langmuir* **15**, 807-812 (1999).
20. J. Shao, E. A. Josephs, C. Lee, A. Lopez, T. Ye, *ACS Nano* **7**, 5421-5429 (2013).
21. T. S. Sreeprasad, A. K. Samal, T. Pradeep, *Langmuir* **23**, 9463-9471 (2007).
22. C.-K. Tsung, X. Kou, Q. Shi, J. Zhang, M. H. Yeung, J. Wang, G. D. Stucky, *J Am Chem Soc* **128**, 5352-5353 (2006).
23. L. Saa, M. Coronado-Puchau, V. Pavlov, L. M. Liz-Marzan, *Nanoscale* **6**, 7405-7409 (2014).
24. N. Fan, Y. Yang, W. Wang, L. Zhang, W. Chen, C. Zou, S. Huang, *ACS Nano* **6**, 4072-4082 (2012).
25. B. Radha, G. U. Kulkarni, *Crystal Growth & Design* **11**, 320-327 (2011).
26. B. Radha, M. Arif, R. Datta, T. Kundu, G. Kulkarni, **3**, 738-747 (2010).
27. Z. c. Zhang, F. Nosheen, J.-c. Zhang, Y. Yang, P.-p. Wang, J. Zhuang, X. Wang, *ChemSusChem* **6**, 1893-1897 (2013).
28. H. J. Levinstein, W. H. Robinson, *J Appl Phys* **33**, 3149-3152 (1962).
29. H. C. Lee, T.-H. Chen, W.L. Tseng, C. H. Lin, *Analyst* **137**, 5352-5357 (2012).
30. Z. Zhang, Z. Chen, D. Pan, L. Chen, *Langmuir* **31**, 643-650 (2015).
31. H. Yuan, K. P. F. Janssen, T. Franklin, G. Lu, L. Su, X. Gu, H. Uji-i, M. B. J. Roeffaers, J. Hofkens, *RSC Adv* **5**, 6829-6833 (2015).
32. Z. Chen, Z. Zhang, C. Qu, D. Pan, L. Chen, *Analyst* **137**, 5197-5200 (2012).

33. Y.-J. Lan, Y.-W. Lin, *Anal Meth* **6**, 7234-7242 (2014).
34. F. M. Li, J. M. Liu, X. X. Wang, L. P. Lin, W. L. Cai, X. Lin, Y. N. Zeng, Z. M. Li, S. Q. Lin, *Sensor Actuat B: Chem* **155**, 817-822 (2011).
35. Z. Zhang, Z. Chen, C. Qu, L. Chen, *Langmuir* **30**, 3625-3630 (2014).
36. V. Raj, T. Johnson, K. Joseph, *Biosens and Bioelectron* **60**, 191-194 (2014).
37. J. P. Chaudhary, A. Kumar, P. Paul, R. Meena, *Carbohydr Polym* **117**, 537-542 (2015).
38. Y. Cheng, C. Qiu, H. Ma, X. Zhang, X. Gu, *Nanoscale* **2**, 685-688 (2010).
39. S. O. Obare, N. R. Jana, C. J. Murphy, *Nano Lett* **1**, 601-603 (2001).
40. G. Chandrasekar, K. Mouglin, H. Haidara, L. Vidal, E. Gnecco, *Appl Surf Sci* **257**, 4175-4179 (2011).
41. S. Hong, J. A. I. Acapulco, H. Y. Jang, S. Park, *Chem Mater* **26**, 3618-3623 (2014).
42. T. Xie, C. Jing, W. Ma, Z. Ding, A. J. Gross, Y.-T. Long, *Nanoscale* **7**, 511-517 (2015).
43. Z. Bao, Z. Sun, M. Xiao, H. Chen, L. Tian, J. Wang, *J Mater Chem* **21**, 11537-11543 (2011).
44. M. N. O'Brien, M. R. Jones, K. L. Kohlstedt, G. C. Schatz, C. A. Mirkin, *Nano Lett* **15**, 1012-1017 (2015).
45. R. Liu, Z. Chen, S. Wang, C. Qu, L. Chen, Z. Wang, *Talanta* **112**, 37-42 (2013).
46. B. Radha, S. Kiruthika, G. U. Kulkarni, *J Am Chem Soc* **133**, 12706-12713 (2011).
47. M. P. Pileni, *J Phys: Condens Mat* **23**, 503102 (2011).
48. K. Gilroy, P. Farzinpour, A. Sundar, T. Tan, R. Hughes, S. Neretina, *Nano Res* **6**, 418-428 (2013).
49. M. L. Personick, M. R. Langille, J. Zhang, N. Harris, G. C. Schatz, C. A. Mirkin, *J Am Chem Soc* **133**, 6170-6173 (2011).
50. J. Zhang, M. R. Langille, M. L. Personick, K. Zhang, S. Li, C. A. Mirkin, *J Am Chem Soc* **132**, 14012-14014 (2010).
51. Y. H. Tsao, S. X. Yang, D. F. Evans, H. Wennerstrom, *Langmuir* **7**, 3154-3159 (1991).
52. G. Mettela, R. Boya, D. Singh, G. V. P. Kumar, G. U. Kulkarni, *Sci. Rep.* **3**, (2013).
53. G. Mettela, M. Bhogra, U. V. Waghmare, G. U. Kulkarni, *J Am Chem Soc* **137**, 3024-3030 (2015).
54. M. L. Personick, M. R. Langille, J. Zhang, C. A. Mirkin, *Nano Lett* **11**, 3394-3398 (2011).

55. G. Mettela, S. Siddhanta, C. Narayana, G. U. Kulkarni, *Nanoscale* **6**, 7480-7488 (2014).
56. S. S. Luthra, X. Yang, L. M. Freitas dos Santos, L. S. White, A. G. Livingston, *Chem Commun*, 1468-1469 (2001).
57. N. C. Lindquist, P. Nagpal, A. Lesuffleur, D. J. Norris, S.-H. Oh, *Nano Lett* **10**, 1369-1373 (2010).
58. A. G. Brolo, D. E. Irish, G. Szymanski, J. Lipkowski, *Langmuir* **14**, 517-527 (1998).

Site Selective Cu Deposition on Au Microcrystallites: Corners, Edges versus Planar Surfaces

Summary

Among epitaxially grown metal over metal systems, Cu on Au surface forms a notable exception given the large lattice mismatch ($\sim 11.2\%$). Although widely observed, Cu growth on Au is less understood at both nano and bulk length scales. The present study has relied on Au microcrystallites which provide adequate platform to access both the length scales and thus have examined Cu electroless deposition using electron microscopy techniques, on planar as well as corner and edge regions distinctly. Amazingly, the growth at different regions was found to be highly varied; the corners were found to be most active, followed by edges and planar regions. Interestingly, sharper the corner more was the Cu deposition. Importantly, both Au{111} and Au{100} facets could be explored simultaneously, using a routine electron microscope.

4.1 Introduction

Heterometallic systems are interesting due to their enhanced chemical stability and catalytical activity (1). In recent years, these interfaces are being revisited equipped with new synthetic recipes and advanced microscopy tools (2-6). Various physical and chemical methods have been employed for conformal growth of one metal over another, where the growth can be epitaxial or non-epitaxial. Usually, epitaxial growth takes place when the lattice mismatch between the participating metals is below 5%, Au/Ag (6), Au/Pd (7) and Pd/Pt (4) being well known examples. Metals with higher lattice mismatch (such as Pd/Ag) do not tend to exhibit epitaxial growth; however, Cu epitaxial growth on various noble and semi-noble metal surfaces is a clear exception. For instance, despite higher lattice mismatch, Cu can epitaxially grow on Pd (7.1%) (2) and Au (11.2%) due to favorable underpotential deposition (UPD) (5, 8-10) and higher Cu-M bond strength (M=Pd and Au, etc) (11). Sieradzki et al. have reported that the strain generated due to the lattice mismatch gets relaxed through the generation of misfit dislocation (12). Using scanning tunneling microscopy (STM), Magnussen et al. (13) studied the Cu growth on bulk Au{111} surface by electrochemical deposition, and ascribed the growth mode to be Stranski-

Krastanov (SK), i.e wetting layer and island formation take place simultaneously. On the contrary, Grillo et al. (14) in their STM study, have reported Frank-van der Merwe (FvdM) type growth for vacuum deposited Cu (layered by layer type growth). In the above mentioned studies, Cu deposition was monitored only on planar surfaces, while the nature of growth at corners and edges was not examined. Bulk single crystals used in such studies offer extended surfaces but make edges and corners practically inaccessible.

As regards nanoparticles, Au nanocrystallites of different shapes have been tried out in solution based epitaxial Cu deposition. Due to finite size of nanoparticles, contributions from corners and edges become very significant (15). The relevant growth modes (FvdM (16) and Tsuji-Ikeda type growth (17) have been identified using high resolution transmission electron microscopy (TEM). In spite of high resolution imaging, finer details relating to shape and crystallographic orientation of the deposited Cu islands could not be discerned (16, 17). In other words, the nature of growth on planar nanoparticle surface as against that on corners and edges, is usually not easily distinguishable, although the nanoparticle as a whole is accessible in microscopy. The issue therefore appears to be around the length scale associated with the bimetal system, single crystals and nanocrystallites being at extreme ends of the scale. An intermediate length scale pertaining to microcrystals should provide the right platform to access all three simultaneously - planar surface, corners and edges, while being able to distinguish and study the nature of growth at each region. Well faceted Au microcrystals grown using a recipe developed in the laboratory indeed prompted this study (18-20). To grow Cu epitaxially, electroless deposition method was adopted (21), so that external influences are avoided. The extent of Cu deposition on different regions of microcrystallite was monitored using electron microscopy (SEM) and the elemental identity by energy dispersive x-ray analysis (EDS). Where relevant, TEM and X-ray diffraction (XRD) techniques have also been employed. The effect of microcrystal size on Cu deposition has also been investigated. The present study thus not only provides a satisfactory explanation for Cu growth on Au but also puts all ambiguities to rest, related to lattice mismatch and epitaxy.

4.2 Scope of the present investigation

In this chapter, the epitaxial growth of Cu on Au microcrystallites has been demonstrated. Unlike previous studies, Au crystallites of adequate size were chosen to study the Cu epitaxial growth.

Here, for the first time, it is shown that Cu deposition takes place preferentially at sharp corners, followed by edges and planar regions much against the high lattice mismatch. The size of Au crystallite also influences the Cu deposition.

4.3 Experimental Section

4.3.1 Materials

Gold chloride (HAuCl_4), tetraoctylammonium Bromide (ToABr), copper sulphate (CuSO_4), sodium potassium tartrate ($\text{KNaC}_4\text{H}_4\text{O}_6 \cdot 4\text{H}_2\text{O}$), sodium hydroxide (NaOH) and toluene were used. All reagents were purchased from spectrochem, India. Water used in this study was double distilled and deionized. Si substrates were cleaned with water, IPA, toluene and dried under N_2 gas.

4.3.2 Synthesis of Au microcrystallites

Au microcrystallites were prepared by using one of our recent reports. Briefly, to a 100 μL of HAuCl_4 (25 mM), 300 μL of ToABr in toluene (50 mM) was added and stirred for 5 min. 100 μL of organic layer was coated on a Si substrate and heated at 135 $^\circ\text{C}$ on a hot plate in air. After growing Au microcrystals, they were washed with toluene to remove any residual precursor and dried with flowing nitrogen.

4.3.2 Cu electroless deposition

Copper plating solution contains solutions A and B. Solution A was prepared by dissolving CuSO_4 (3 g), sodium potassium tartrate (14 g) and NaOH (4 g) in 100 ml of distilled water. Solution B was aqueous solution of formaldehyde (37.2 wt%). Solution A and B were mixed in the volume ratio of 5:1. For Cu electroless deposition, Au microcrystallites were dipped in plating solution. The process was halted at different times by taking out the sample from solution. The obtained Au/Cu crystallites were characterized using SEM, EDS, TEM and XRD techniques.

4.4 Results and discussion

Au microcrystals were prepared using a method reported recently (18-20). Briefly, AuToABr complex is prepared by the stabilization of $(\text{AuCl}_4)^-$ with tetraoctylammonium bromide (ToABr) in toluene (~ 50 mM). A few drops (~ 30 μL) of AuToABr solution was drop-coated on a Si substrate, thermalized on a hot plate at 135 $^\circ\text{C}$ in air for 1h. The samples were washed with toluene to dissolve away the unreacted precursor. Among the obtained Au microcrystals, hexagons and triangles occurred more frequently, while cuboctahedrons, penta-twinned nanorods and decahedrons form the minor products. The width of these crystals ranges from ~ 0.7 to 80 μm . The crystallites exhibit well defined smooth facets, assignable to $\{111\}$ and $\{100\}$ (20). One such Au microcrystal is shown in Fig. 4.1(a). In hexagons, triangles and cuboctahedrons, top and bottom facets are made of $\{111\}$ facets, whereas the $\{100\}$ and $\{111\}$ construct the side facets (Figs. 4.1(b-c)) (20).

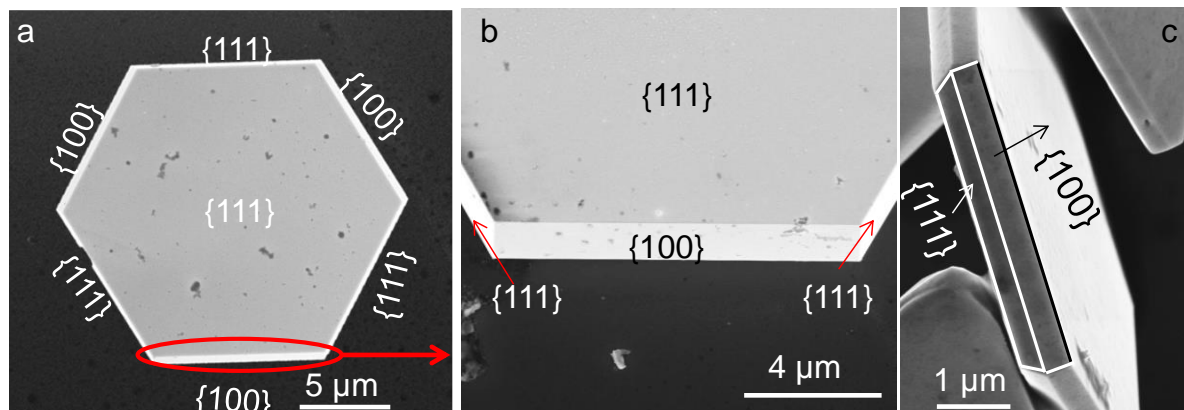
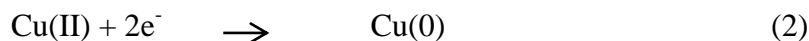


Figure 4.1 (a, b) SEM images at different magnifications of a Au microcrystal, and (c) side view of a Au microcrystallite, assigned with $\{111\}$ and $\{100\}$ facets.

To grow Cu epitaxially on Au microcrystals, electroless deposition method is preferable as the process will be guided by the nature of the host surface rather than an external electric field (13). For the same reason, the crystallites were used without any surface modification. The deposition involved the reduction of Cu(II) - tartrate in alkaline medium with formaldehyde onto the Au microcrystals (22). Here, Au being an active catalyst for oxidation of formaldehyde in basic medium is clearly an advantage (23). Hence, Cu deposition takes place rapidly on the Au crystallites. The reduction of Cu(II) can be described as following equations (22).



For electroless deposition of Cu, as-prepared Au microcrystals were immersed in the copper plating solution. A series of intermediate products were captured by halting the Cu deposition at different times. After plating, the samples were washed with water, ethanol, and dried under N₂ gas. Cu growth on Au surfaces has revealed several interesting aspects as discussed below. In very initial stages, Au surfaces become somewhat rough (Fig. 4.2) before distinct deposition can be observed, which may be attributed to Cu wetting layer (see EDS in Fig. 4.2).

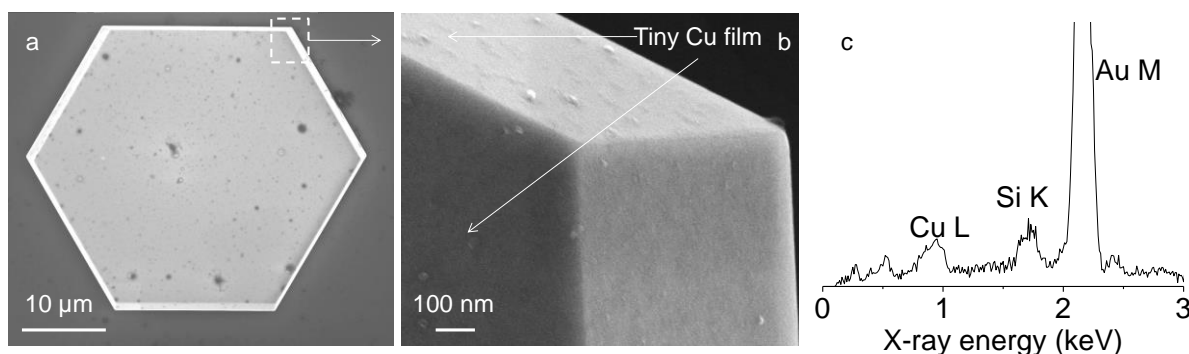


Figure 4.2 (a-b) SEM images of Au microcrystallite just after ~ 15 seconds of Cu plating. Arrows show the roughened regions caused by Cu deposition. (c) EDS spectrum shows the weak Cu L signal attributed to the Cu wetting layer.

After 4 min exposure to the plating solution, the Au{111} facets get covered with triangle and hexagonal shaped islands (Figs 4.3(c-h)), while on Au{100} facets square shaped islands are seen (Figs. 4.3(i-l)), and all the islands are composed of Cu as evident from EDS analysis (see the spectrum in Fig. 4.3(i)). Interestingly, the interior angles of Cu triangles and hexagons are ~ 60° and ~ 120° respectively which essentially reflect the symmetry of the Au{111} facet itself. Further, the angles between two adjacent Cu islands are ~ 60° and 120°, indicating that the space between Cu islands can be filled by either a triangle (for 60° gap) or by a hexagon (120°) (Fig. 4.3(d)), clearly indicating epitaxial relation in the growth. This observation is similar to that made by Magnussen et al. based on in situ STM studies of the surface (13). After prolonged deposition, the size of the Cu islands increased up to ~ 400 nm (Fig. 4.3(f)), and the average height, up to ~ 140 nm (Fig. 4.4) to eventually form a continuous film (Fig. 4.3(g)). Similarly on

the {100} facets, square shaped Cu islands with interior angle of 90° closely pack themselves (Figs. 4.3(i-k)). Like the parent Au crystallites, the Cu crystallites (islands) are seen enclosed with well-defined facets; those formed on Au{111} are enclosed with {111} and {100} facets (Fig. 4.3(e)), while those on {100} follow the substrate morphology itself (Fig. 4.3(j)) (5). The above observations are schematically illustrated in Figs. 4.3(h) and (l).

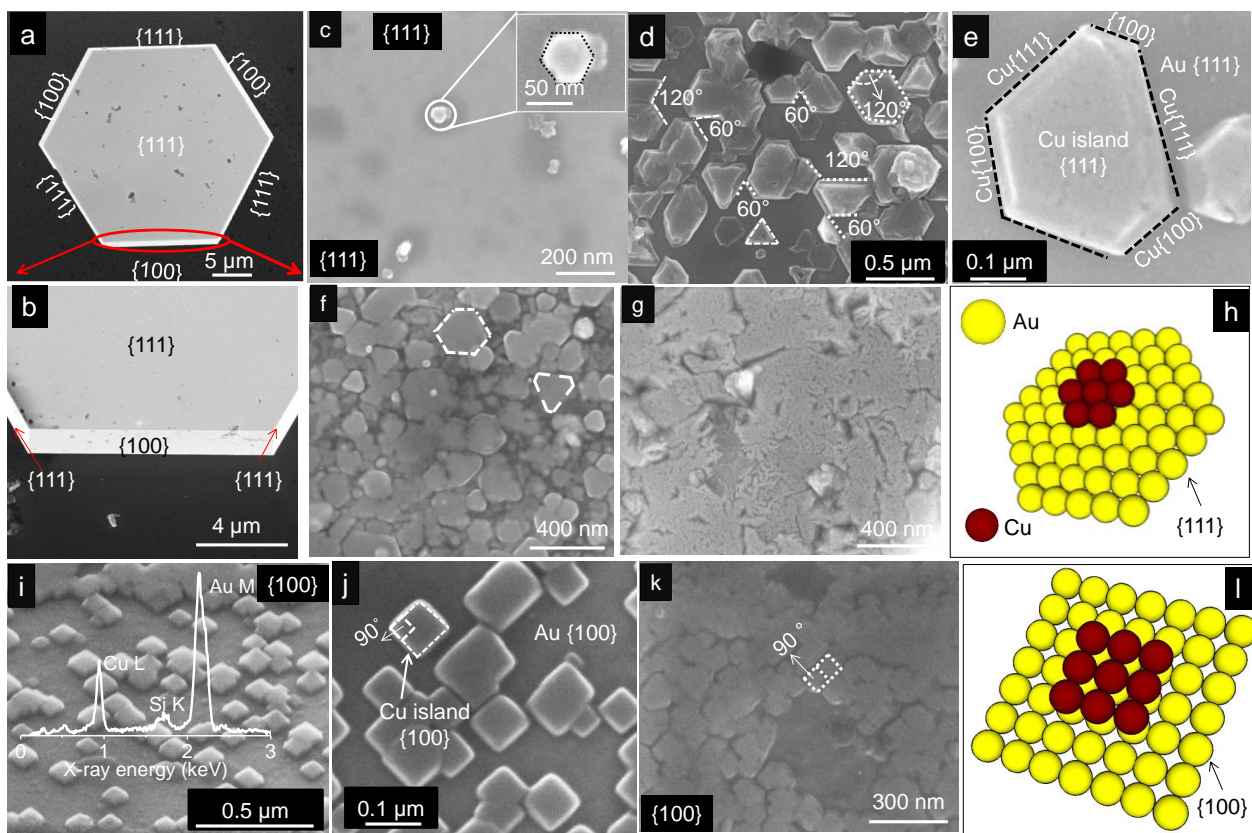


Figure 4.3 (a, b) SEM images of a Au microcrystal at different magnifications before Cu deposition. SEM images depicting the shape of Cu islands formed on Au{111} (c-h) and Au{100} (i-l) facets. Pictorial representation of Cu islands on Au{111} and {100} facets are shown in (h) and (l) respectively. The corresponding EDS spectrum collected from Cu islands is shown on the top of the image f.

It appears that Cu initially forms a wetting layer as seen by the EDS and increase in surface roughness before well-defined islands could grow with specific relation to the geometry of the underlying Au facet. This growth therefore closely resembles the SK (Stranski-Krastanow) mode (5), which is also understandable following the three rules introduced by Fan et al. for bimetal

interfaces (3). Because of lower atomic radius and electronegativity values of Cu (0.138 nm, 1.9 eV) compared to those of Au (0.144 nm, 2.54 eV), and higher Au-Cu bond strength, Cu can easily wet the Au surface forming few layers (16). As the deposition advances, island-like Cu crystallites are formed as shown in Fig. 4.3. Our observations on Au microcrystals differ from those made by Tsuji et al. and Yoshida et al. on Au nanocrystals who reported layer type growth mode (16, 17). The nanocrystal surface being relatively more active, only layer type deposition may be favored.

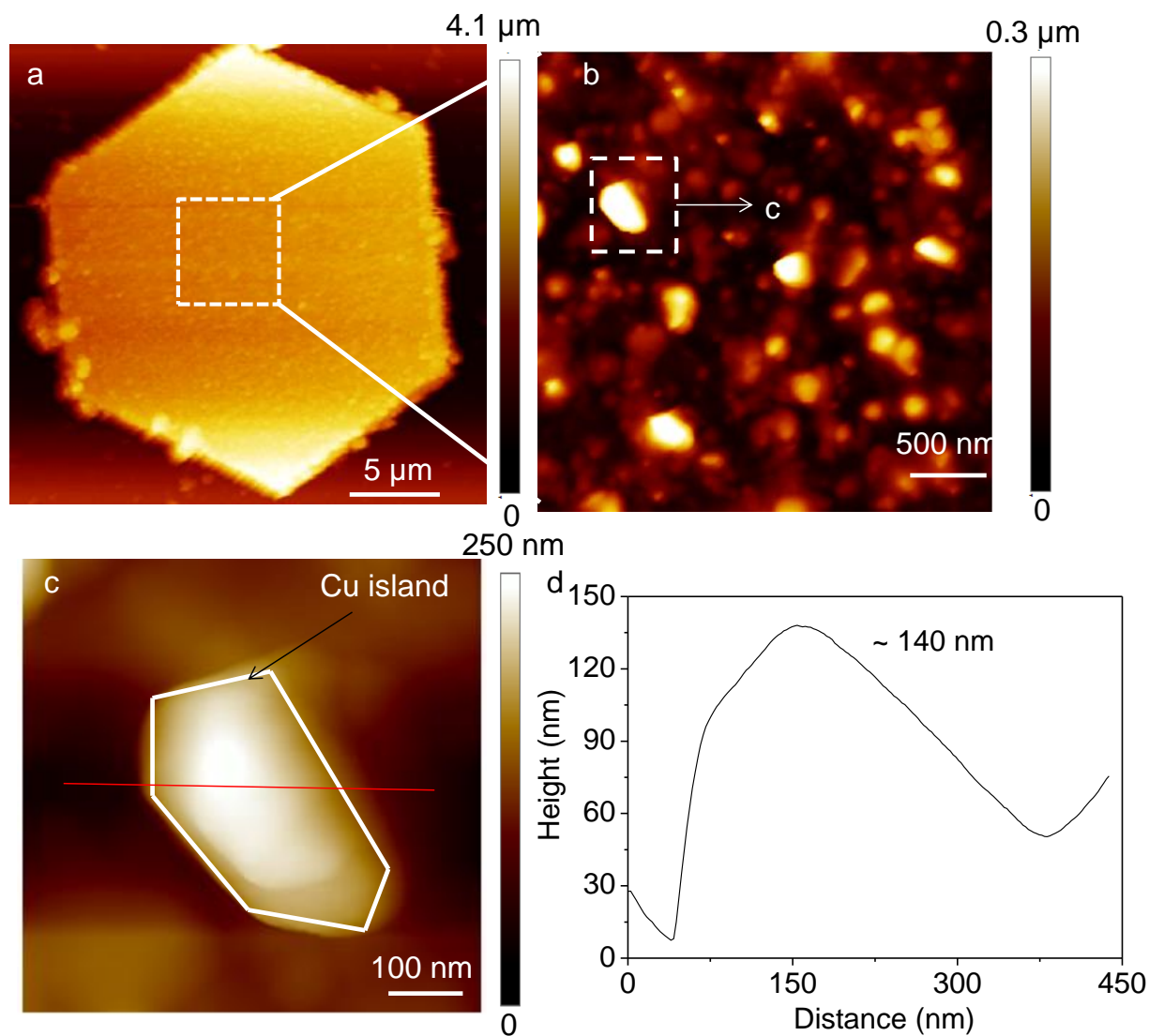


Figure 4.4 (a-c) AFM images of Cu islands formed on Au hexagon. (d) Height profile along the line drawn in c.

In Figs. 4.5(a-f), are shown examples of SEM and EDS mapping of Au trapezoid microcrystals with top {111} facet hosting 60° and 120° corners. After 4 minutes of electroless reaction (Fig. 4.5(a)), the extent of Cu deposition is found to be relatively high at the 60° corners compared to that at 120° corners and interestingly, no deposition is seen in the center (see Cu L contour image in Fig. 4.5(d)). From the 60° corner (C1) seen at the top of the image, the deposition extends up to ~ 7.5 μm inwardly on the {111} facet, which is slightly less (5.3 μm) for the left 60° corner (C2) presumably due to its lesser sharpness. Importantly for 120° corners (C3 and C4), these values are much lower (1.5-1.7 μm).

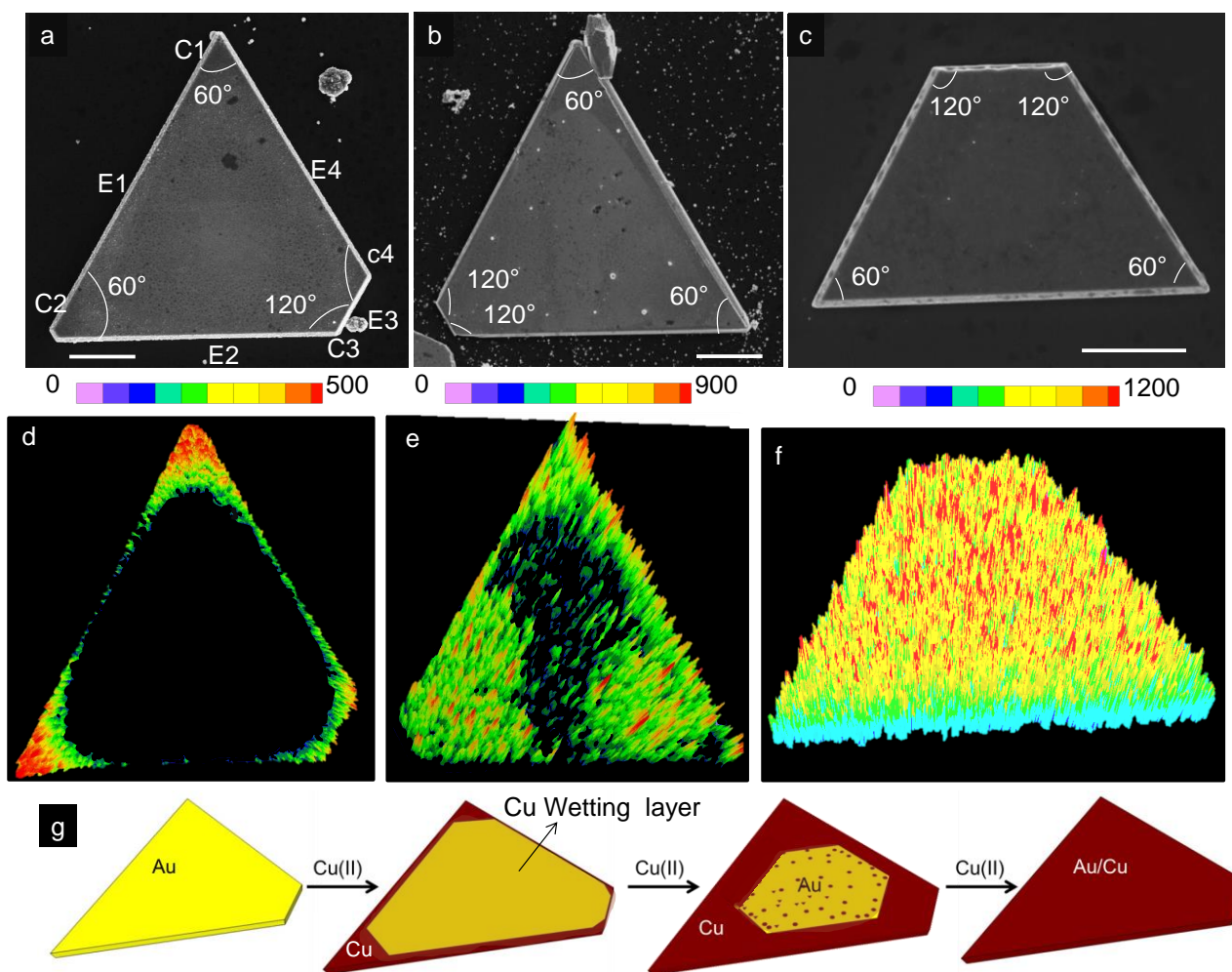


Figure 4.5 (a-c) SEM images of trapezoid Au crystals after Cu deposition for (a) 4, (b) 8 and (c) 12 min. (d-f) Contour plots illustrate the distribution of Cu L signal across the Au crystallites shown in a, b and c respectively. (g) Schematic illustration of site selective Cu deposition on Au microcrystals. Scale bar, 10 μm.

The above observations clearly indicate that the propensity of Cu deposition is varied around the given Au{111} facet implying a lower Au-Cu lattice on the angle enclosed at the corner. The {111} facet exhibits corners with angles of 120° and 60° and the corresponding CN values are 6 and 5. The Au-Au bond length is mismatch at corners and edges, else the observed deposition would have been uniform all over the surface. It may be noted that these observations are quite different from what is reported in the literature. In earlier studies on large Au single crystal surfaces (typically few mm to cm), the corners and edges have not been examined.⁵ In case of nanocrystallites, Tsuji et al. have reported non-uniform deposition of Cu and Ni on Au nanocrystallites (16, 24), which was attributed to higher lattice mismatch. However, there has been no detailed study that deals with the participation of corners and interior angles of facets of nano/microcrystallites in obtaining hetero-metallic systems. In our study, this aspect has come out quite clearly. The above observations may be explained based on local reactivity as well as lattice mismatch between the Au surface and the incoming Cu. In general, surface atoms have lower coordination number than the bulk atoms (CN, 12) (25, 26). The CN value for surface Au atoms on the {111} and {100} facets is 9 and 8 respectively. At edges, it is 7 and at the corners, it can be even lower, depending known to decrease with lowering CN value (Fig. 4.6(b)). Accordingly, the order of Au-Au bond length is as follows: bulk (2.88 Å) > surface Au{111} (2.84 Å) > surface Au{100} (2.82 Å) > edge (2.80 Å) > corner with 120° (2.78 Å) and corner with 60° (2.77 Å) (25-28). It is evident that the mismatch with respect to Cu-Cu bond length (2.56 Å) (29) should follow the same order: 11.2% (bulk), 9.85% (surface {111}), 9.21% (surface {100}), 8.57% (edge), 7.91% (120° corner) and 7.58% (60° corner) (Fig. 4.6(a)) (25). A similar trend has been obtained in DFT study (27). From these considerations, one may expect that the propensity of Cu deposition should increase in the same order. It appears that as more and more Cu is deposited at the corners and edges, the growth towards the central region is essentially independent of the underlying substrate, depends rather on interfacial strain (30). This kind of site selective Cu deposition on Au has been observed for the first time, to the best of our knowledge.

After 8 minutes, Cu deposition extends gradually to the center of the microcrystal (Figs. 4.5(b) and (e)), to eventually cover the whole facet (Figs. 4.5(c, f)). After 12 minutes, Au crystallites of different shapes are fully covered by Cu (Fig. 4.7). The progress of Cu deposition is illustrated in the schematic in Fig. 4.5(g). A similar trend was seen in a hexagonal shaped Au microcrystal

hosting top {111} facet with 120° corners. Cu deposition started at corners, edges and propagated to center of the Au hexagon. Therefore, it is understandable that Cu deposition selectively commences from the sharp corners, followed by edges, and progresses towards the center of the microcrystal.

a

Coordination Number (CN) ²⁸	12	9	8	7	6	5
Location	Bulk	(111) surface	(100) Surface	Edge	corner (120 deg)	corner (60 deg)
Au-Au Bond length (Å) ^{25, 26}	2.88	2.84	2.82	2.80	2.78	2.77
Mismatch (%)	11.11	9.85	9.21	8.57	7.91	7.58

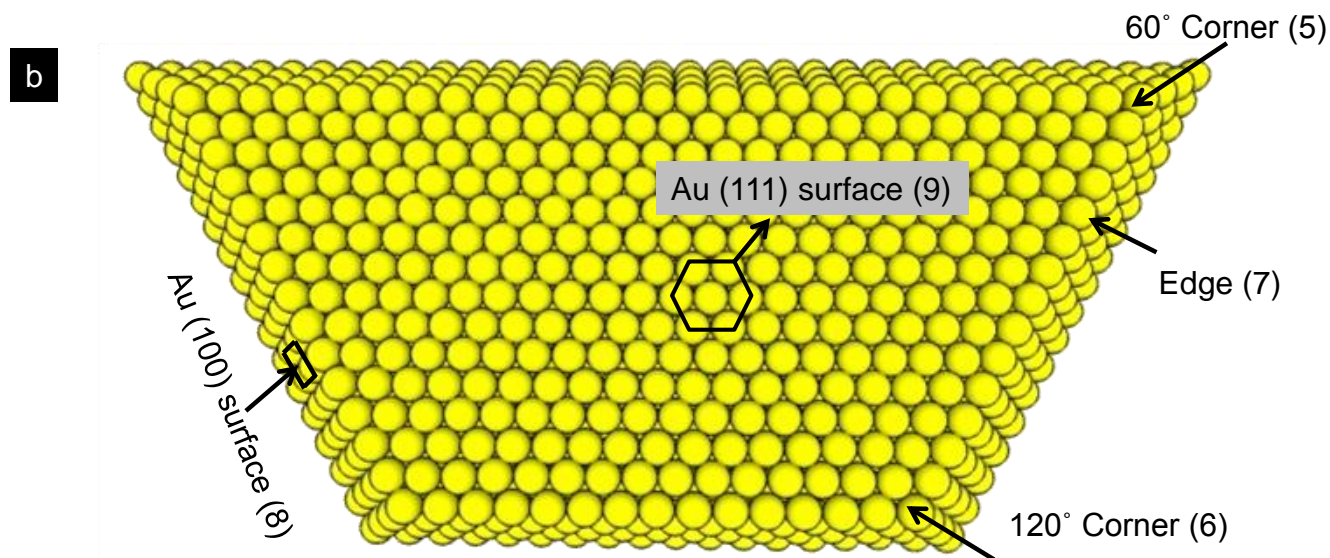


Figure 4.6 (a) Calculated lattice mismatch for Cu at various sites of Au microcrystallites by considering the bulk Cu-Cu bond length of 2.56 Å (ref 29). Au-Au bond lengths are taken from refs 25 and 26. (b) Schematic illustration of various sites on a trapezoid with the respective coordination number (CN) in bracket.

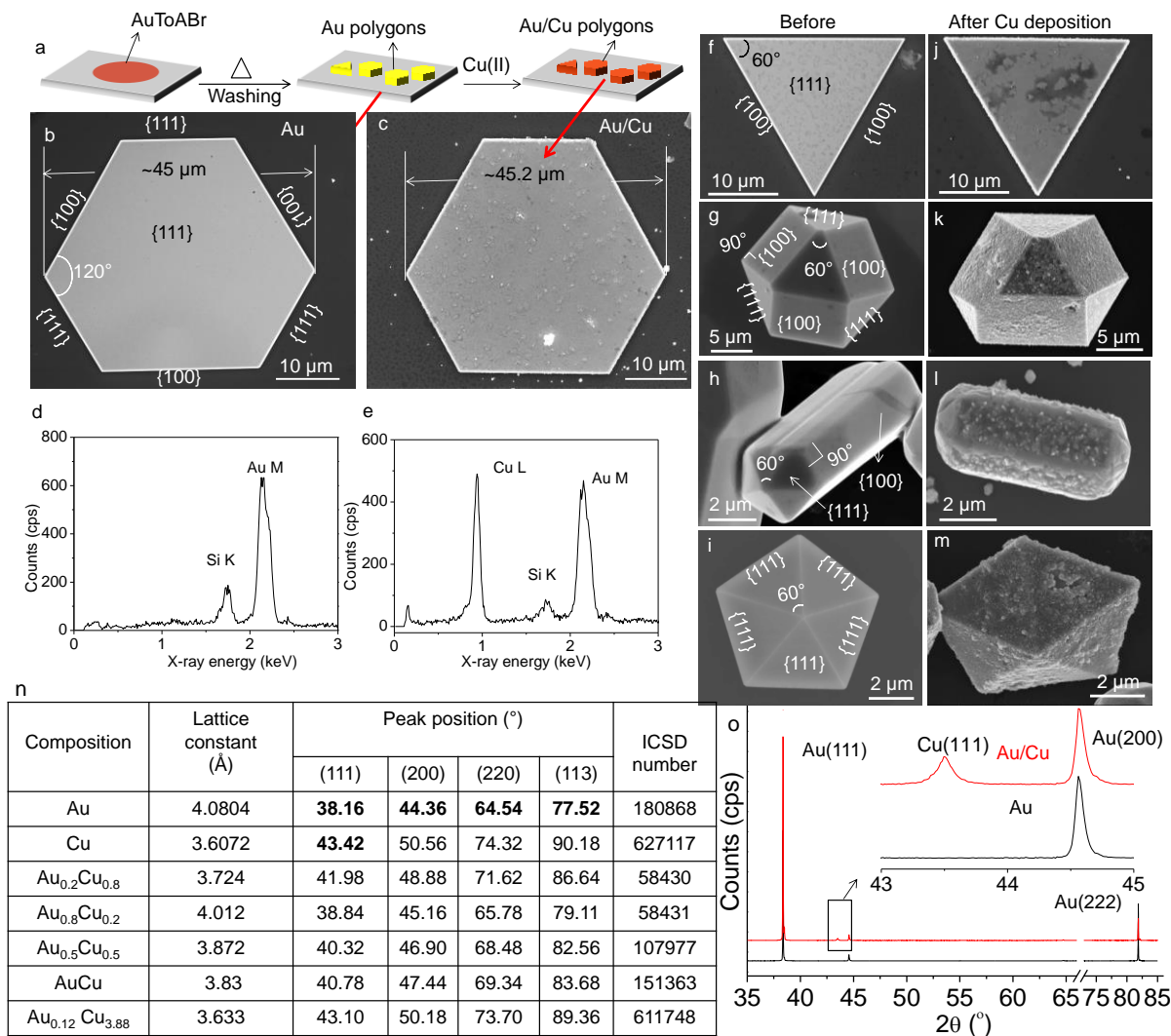


Figure 4.7 (a) Schematic illustrating synthesis of Au/Cu core-shell crystallites. SEM images of a Au hexagonal microcrystal, before (b) and after Cu deposition (c) with corresponding EDS curves in (d) and (e) respectively. SEM images of Au microcrystals of different shapes before (k-n) and after Cu deposition (f-m); triangle (f and j), cuboctahedron (g and k), penta-twinned nanorod (h and l) and decahedron (i and m). The interior angles of {111} and {100} facets of various geometries have been assigned. (n) Summary of possible compositions of Au and Cu. Numbers shown in bold have been observed in this study and correspond only to Au and Cu separately. Hence, there is no alloy formation. (o) XRD pattern collected from pristine Au and Au/Cu core-shell microcrystals.

Besides the crystal shape, the size also plays a role in Cu deposition (Fig. 4.8). For a crystallite size of $\sim 52 \mu\text{m}$ after 15 min exposure to electroless plating solution, the atomic ratio of Cu to

Au as measured by EDS, was < 0.1 , while the value was ~ 43 for a $0.7 \mu\text{m}$ crystallite (Figs. 4.8(a-e)). It is evident that Cu to Au ratio increases as the width of the Au plate decreases. Here, a higher atomic ratio arises due to limited penetration of the e-beam into Au due to the thick Cu overlayer, and thus stands for relative Cu thickness. Although nano and microcrystallites possess similar internal angles, Cu deposition is relatively higher on nanocrystallites due to their finite size. The separation between edges increases with the size of the crystallites. Hence, in the case of micronsize Au crystals, the time needed for the complete deposition is higher than in the case of nanocrystallites.

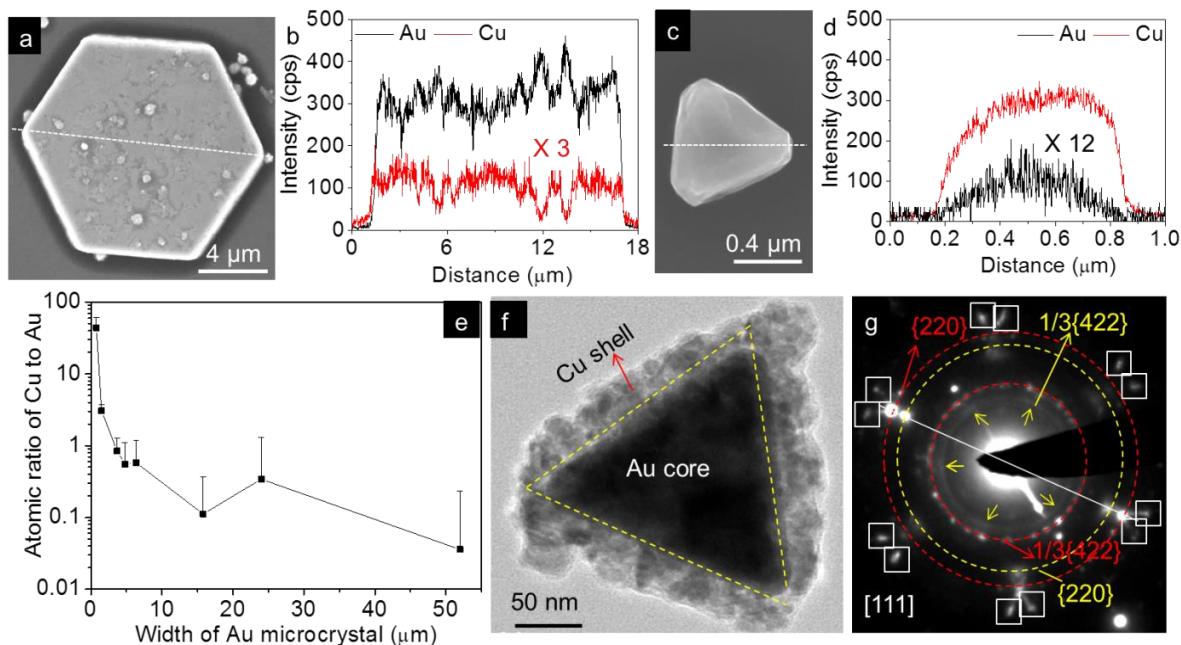


Figure 4.8 (a-b) SEM images of Au/Cu core-shell microcrystals and (c-d) the line mapping along the lines drawn in a and b. (e) at% ratio of Cu to Au along the width of Au microcrystallites. (f, g) TEM image and ED pattern obtained from Au/Cu triangular nanocrystallite. In ED, yellow and red circles represent diffraction spots from Au and Cu lattices, respectively. Square boxes indicate the spots generated due to double diffraction.

Further, TEM analysis has also confirmed the epitaxial growth of Cu on Au crystallites. TEM image and ED pattern of Au/Cu core-shell nanocrystallites are shown in Figs. 4.8(f) and (g). Due to higher atomic number of Au ($Z=79$), the core appears much brighter than Cu shell ($Z=29$). As evident from the TEM image (Fig. 4.8(f)), Au/Cu core-shell nanocrystallites follow the geometry

of the Au crystallite; it also confirms the conformal coverage of Cu on Au nanocrystallites. ED pattern of Au/Cu triangle obtained along the $\langle 111 \rangle$ direction consists of two sets of hexagonal spots that are indexable to reflections of Au and Cu (Fig. 4.8(g)). The $\{220\}$ reflections of Au and Cu are surrounded by faint diffraction spots (shown in squares). These weak reflections are due to the double-diffraction spots of Au and Cu. Importantly, as shown in ED pattern (Fig. 4.8(g)), Au and Cu are similarly oriented irrespective of the shape of the Au core. The allowed reflections of Au and Cu are collinear, indicating that Cu has grown epitaxially on Au despite larger lattice mismatch (11.2%) between Au and Cu. Finally, XRD patterns recorded from pristine Au and Au/Cu are dominated with the $\{111\}$ reflection of Au due to the preferential orientation of majority of the crystallites (Fig. 4.7(o)). Au/Cu core-shell microcrystallites exhibit a weak reflection at $\sim 43.5^\circ$ assignable to $\text{Cu}\{111\}$, while other reflections of Cu are not seen in the XRD pattern. Importantly in the XRD pattern, neither new peaks nor deformation in any of the peaks, is observed, indicating the absence of Au-Cu alloy formation and the core/shell formation does not affect the lattice parameters of Au and Cu (see Table in Fig. 4.7(n)).

4.5 Conclusion

In conclusion, the present study addresses the epitaxial growth of Cu on Au surface employing Au microcrystallites of different shapes in a simple electroless deposition method. Cu growth involved the formation of wet-layer on Au surfaces followed by islands, which is the classical SK mode. The shape of the Cu islands follows the crystal nature of underlying surface; hexagonal, triangle and square shaped Cu islands have been observed on $\text{Au}\{111\}$ and $\text{Au}\{100\}$ facets, respectively. For the first time, the role of the surface site, planar, edge or corner, on Cu epitaxial growth is demonstrated here. Cu deposition was found to be dependent on the local reactivity of the sites rather than shape of the crystallites. It is clearly shown that Cu deposition commenced at sharper corners (60°) followed by broader 120° corners and edges, and finally, at planar sites. Size effect on Cu deposition has also been studied. Cu deposition is relatively slower on larger Au crystallites than on smaller crystallites. The work demonstrated here is in principle, extendable to other noble metals with high lattice mismatches, for example Ag/Cu and Au/Ni systems.

References

1. R. Ghosh Chaudhuri, S. Paria, *Chem Rev* **112**, 2373-2433 (2012).
2. M. Jin, H. Zhang, J. Wang, X. Zhong, N. Lu, Z. Li, Z. Xie, M. J. Kim, Y. Xia, *ACS Nano* **6**, 2566-2573 (2012).
3. F.-R. Fan, D.-Y. Liu, Y. F. Wu, S. Duan, Z.-X. Xie, Z.-Y. Jiang, Z.-Q. Tian, *J Am Chem Soc* **130**, 6949-6951 (2008).
4. K. Cao, Q. Zhu, B. Shan, R. Chen, *Sci. Rep.* **5**, 8470 (2015).
5. R. Randler, M. Dietterle, D. M. Kolb, *Z Phys Chem* **208**, 43-56 (1999); published online Epub1999 (
6. C. Xue, J. E. Millstone, S. Li, C. A. Mirkin, *Angew Chem Int Edit* **46**, 8436-8439 (2007).
7. S. K. Srivastava, T. Hasegawa, R. Yamada, C. Ogino, M. Mizuhata, A. Kondo, *RSC Adv* **3**, 18367-18372 (2013).
8. R. J. Randler, D. M. Kolb, B. M. Ocko, I. K. Robinson, *Surf Sci* **447**, 187-200 (2000).
9. J. G. Xu, X. W. Wang, *Surf Sci* **408**, 317-325 (1998).
10. D. Krznarić, T. Goričnik, *Langmuir* **17**, 4347-4351 (2001).
11. A. H. Pakiari, Z. Jamshidi, *J Phys Chem A* **114**, 9212-9221 (2010).
12. T. Trimble, L. Tang, N. Vasiljevic, N. Dimitrov, M. van Schilfgaarde, C. Friesen, C. V. Thompson, S. C. Seel, J. A. Floro, K. Sieradzki, *Phys Rev Lett* **95**, 166106 (2005).
13. O. M. Magnussen, R. J. Behm, *J Electroanal Chem* **467**, 258-269 (1999).
14. F. Grillo, H. Früchtl, S. M. Francis, N. V. Richardson, *New J Phys* **13**, 013044 (2011).
15. Y. Xia, Y. Xiong, B. Lim, S. E. Skrabalak, *Angew Chem Int Edit* **48**, 60-103 (2009).
16. M. Tsuji, D. Yamaguchi, M. Matsunaga, M. J. Alam, *Cryst. Growth Des.* **10**, 5129-5135 (2010).
17. Y. Yoshida, K. Uto, M. Hattori, M. Tsuji, *CrystEngComm* **16**, 5672-5680 (2014).
18. B. Radha, M. Arif, R. Datta, T. Kundu, G. Kulkarni, *Nano Res* **3**, 738-747 (2010).
19. B. Radha, G. U. Kulkarni, *Cryst. Growth Des.* **11**, 320-327 (2011).
20. G. Mettela, G. U. Kulkarni, *Nano Res*, (2015)DOI 10.1007/s12274-015-0797-8).
21. S. Kiruthika, R. Gupta, K. D. M. Rao, S. Chakraborty, N. Padmavathy, G. U. Kulkarni, *J Mater Chem C* **2**, 2089-2094 (2014).
22. T. Ogura, M. Malcomson, Q. Fernando, *Langmuir* **6**, 1709-1710 (1990).

23. M. Enyo, *J Electroanal Chem Interfacial Electrochem* **186**, 155-166 (1985).
24. M. Tsuji, D. Yamaguchi, M. Matsunaga, K. Ikedo, *Cryst. Growth Des.* **11**, 1995-2005 (2011).
25. J. T. Miller, A. J. Kropf, Y. Zha, J. R. Regalbuto, L. Delannoy, C. Louis, E. Bus, J. A. van Bokhoven, *J Cataly* **240**, 222-234 (2006).
26. W. J. Huang, R. Sun, J. Tao, L. D. Menard, R. G. Nuzzo, J. M. Zuo, *Nat Mater* **7**, 308-313 (2008).
27. T. W. Janssens, B. Clausen, B. Hvolbæk, H. Falsig, C. Christensen, T. Bligaard, J. Nørskov, *Top Catal* **44**, 15-26 (2007).
28. Y.-H. Lee, G. Kim, M. Joe, J.-H. Jang, J. Kim, K.-R. Lee, Y.-U. Kwon, *Chem Commun* **46**, 5656-5658 (2010).
29. H. Oyanagi, Y. Orimoto, K. Hayakawa, K. Hatada, Z. Sun, L. Zhang, K. Yamashita, H. Nakamura, M. Uehara, A. Fukano, H. Maeda, *Sci. Rep.* **4**, 7199 (2014).
30. J. Zeng, J. Tao, D. Su, Y. Zhu, D. Qin, Y. Xia, *Nano Lett* **11**, 3010-3015 (2011).

Highly tapered pentagonal bipyramidal Au microcrystals with high index faceted corrugation: Synthesis and optical properties

Summary

Focusing light at sub-wavelength region opens up interesting applications in optical sensing and imaging beyond the diffraction limit. In the past, tapered Au wires with carved gratings have been employed to achieve nanofocusing. The fabrication process however, is expensive and the obtained wires are polycrystalline with high surface roughness. A chemical synthetic method overcoming these hurdles should be an attractive alternative. Here, a simple method is reported to chemically synthesize Au microcrystals ($\sim 10 \mu\text{m}$) bearing pentagonal bipyramidal morphology with surface corrugations assignable to high index planes. The method is a single step solid state synthesis at a temperature amenable to common substrates. The microcrystals are tapered at both ends forming sharp tips ($\sim 55 \text{ nm}$). Individual microcrystals have been used as pick and probe SERS substrates for a dye embedded in a polymer matrix. The unique geometry of the microcrystal also enables light propagation across its length.

5.1 Introduction

One-dimensional (1D) metal nanostructures have gained importance over the last decade due to their interesting optical properties such as tunable absorption from visible to near infrared region (1) and Raman scattering (2). They exhibit distinct surface plasmon features, transverse and longitudinal, associated with their dimensionality (3) which is routinely observed with Ag and Au nanowires (4). Apart from nanowires, there are other quasi 1D structures namely bipyramids or nanorice, bulged in the center and tapered at the ends (5), which have been the focus of recent research on anisotropic structures. For instance, Liu et al. have reported the synthesis of Au bipyramids with lengths of, 120 nm prepared in a highly acidic medium (6). Zheng et al. have synthesized Au nanorice (50–70 nm) bound by high index planes and utilized them for carbon monoxide oxidation (7). Additionally, Au bipyramids have been employed in varied applications such as dampening of acoustic vibrations (8) and dielectric sensing (9). Au nanostars with sharp

tips have shown superior surface enhanced Raman spectroscopy (SERS) activity (10) and plasmon mediated sensing (11). Odom and co-workers have shown the photothermal response of the Au nanopyramids with sharp tips (12). Nanorice-like structures have been reported in the case of Ag as well (13). Recently, star-fruit shaped Au nanorods of lengths up to, 1 μm have been reported by Vigderman and co-workers (14). However in such cases (15), the structures obtained are usually not beyond, 1 μm (for a comprehensive survey of the current literature on bipyramids, see Table 5.1).

Table 5.1 Literature reports for the synthesis of Au rice/pentagonal bipyramidal structures.

S.No	Shape	Approximate length (nm)	Reference
1	Au bipyramids	75	(16)
2	Au bipyramids	100	(6)
3	Au/Ag alloy bipyramids	40-90	(17)
4	Au bipyramids	200	(5)
5	Au bipyramids	75	(8)
6	Au bipyramids	100	(18)
7	Au bipyramids	250-350	(19)
8	Au bipyramids	100	(9)
9	Ag nanorice	450	(13)
10	Au bipyramids	600	(20)
11	Au bipyramids	130	(21)
12	Au bipyramids	100	(22)
13	Au bipyramids	70	(15)
14	Au nanorice	50-70	(7)
15	Au nanorice	370	(23)
16	Au bipyramids	100	(24)
17	Au bipyramids	100	(25)
18	Au bipyramids	55	(26)

Besides chemical methods, lithography based methods have also been employed to produce metal anisotropic structures. Metal wires with sharp tips produced by lithography are most sought after in plasmonic waveguides (27). However, lithography based method involve prefabricated templates, focused ion beam (FIB) milling, metal deposition, template stripping and such processes (28-30) and are not practical for large scale synthesis.

5.2 Scope of the investigation

This chapter deals with a simple method of producing Au μ -corrugated pentagonal bipyramids (μ -CPBs) in high yield, with lengths beyond 10 μ m, tips being sharp (tip diameter < 50 nm). For many applications such as optical nano-focusing (31, 32), it is desirable to have nanowire-like lengths, i.e., typically few micrometers but with the aforementioned special morphology. This explains the reason why many have resorted to using lithography methods to obtain large metal anisotropic structures such as pyramids and grooved structures required in nanophotonic applications (29). In this chapter, the synthesis and microscopy characterization of pentagonal bipyramidal structures of Au (~ 10 μ m long) reported. The obtained individual microcrystals have been employed as SERS substrates and optical waveguides.

5.3 Experimental Section

Hydrogen tetrachloroaurate(III) hydrate ($\text{HAuCl}_4 \cdot 3\text{H}_2\text{O}$), silver nitrate (AgNO_3), tetraoctylammonium bromide (ToABr), and toluene were obtained from spectrochem, India and used without further purification. The water used throughout this investigation was double distilled and deionized. To a 1.5 mL of HAuCl_4 (25 mM), 6 mL of tetraoctylammonium bromide (ToABr) in toluene (50 mM) was added and stirred for 5 min. The bottom aqueous phase became colorless and top organic phase developed red color. Then, a 0.5 mL of AgNO_3 (25 mM) was added to the solution and stirred for ~ 10 hrs. The resultant organic phase was in red color as shown in Fig 5.1. In this case, the volume ratio of Au(III) and Ag(I) in aqueous phase was 75:25. Likewise, different volume ratios of Au(III) and Ag(I) such as 50:50, 65:35, 80:20, 90:10 have been prepared. In all the experiments, the volume ratio of aqueous and organic phase was kept

constant as 1:3. The substrates used i.e., Si and glass were cleaned twice with water, IPA, toluene and dried under N₂ gas.

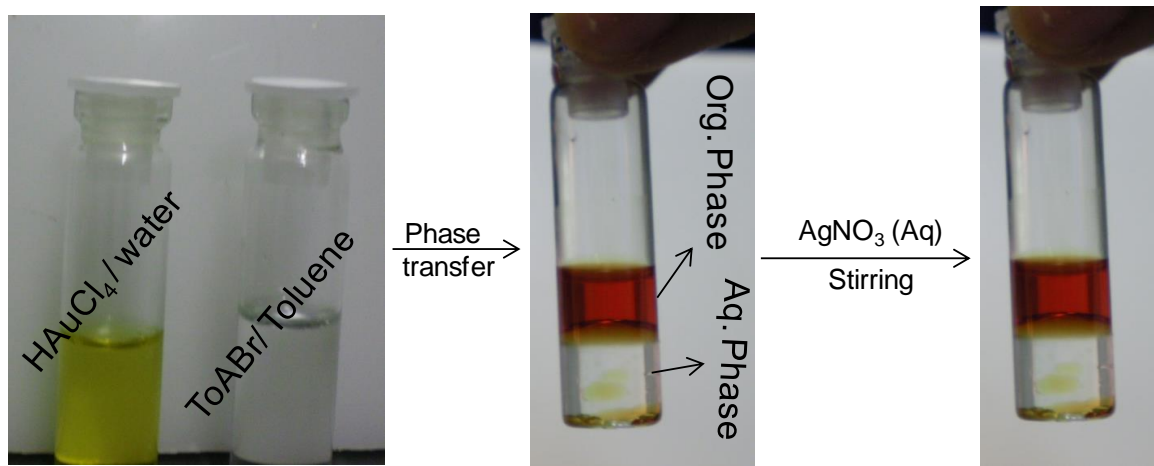


Figure 5.1 Steps involved in the precursor preparation.

5.4 Results and discussion

5.4.1 Characterization of AuAgToABr

The phase transferred organic phase (henceforth termed as AuAg-ToABr) was separated using a micropipette. After the evaporation of solvent, the isolated solid precursor was characterized using IR spectroscopy, XRD and TGA (Fig 5.2)

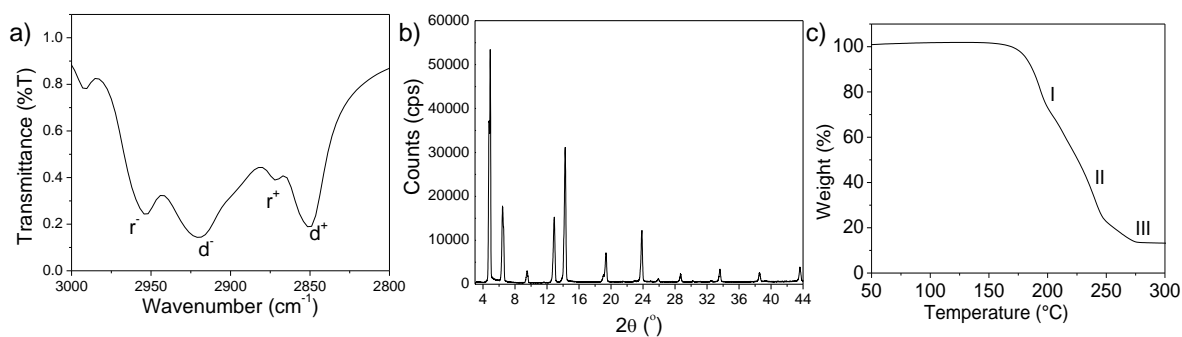


Figure 5.2 (a) IR spectrum, (b) XRD and (c) TGA of AuAgToABr.

In the IR spectrum (Fig 5.2), the peaks at 2952 and 2870 cm⁻¹ correspond to asymmetrical and symmetrical vibrational modes of CH₃, respectively. The peaks at 2924 and 2850 cm⁻¹ refer to asymmetrical and symmetrical vibrational modes of CH₂, respectively. The IR data shows the

presence of ToABr organic component in the precursor. The precursor solid was further characterized using XRD (Fig 5.2). TGA plot showing various stages (I-III) of decomposition of the precursor. The decomposition starts at ~ 160 °C and the weight loss occurs in three steps - region I (20.46%; 1 mole of ToA, Cl_2 and Br_2), regions II (53.61%; 3 moles of ToA, 2 moles of n-octyl bromide, Cl_2 or HBr) and region III (12.31%; 1 mole of ToA) corresponding respectively to solvent evaporation, AuAgToABr decomposition, desorption of ToA, and Cl^- , and the metallic residue (Fig 5.2). Majority of the weight loss is due to the removal of the ToA and it occurs in the range of 150–300 °C. Based on TGA, the derived formula is $(\text{AuCl}_4)^-(\text{AgCl}_2)^-.4\text{ToABr}$, which in a simplified way, is written as AuAgToABr.

5.4.2 Optimization of synthesis conditions

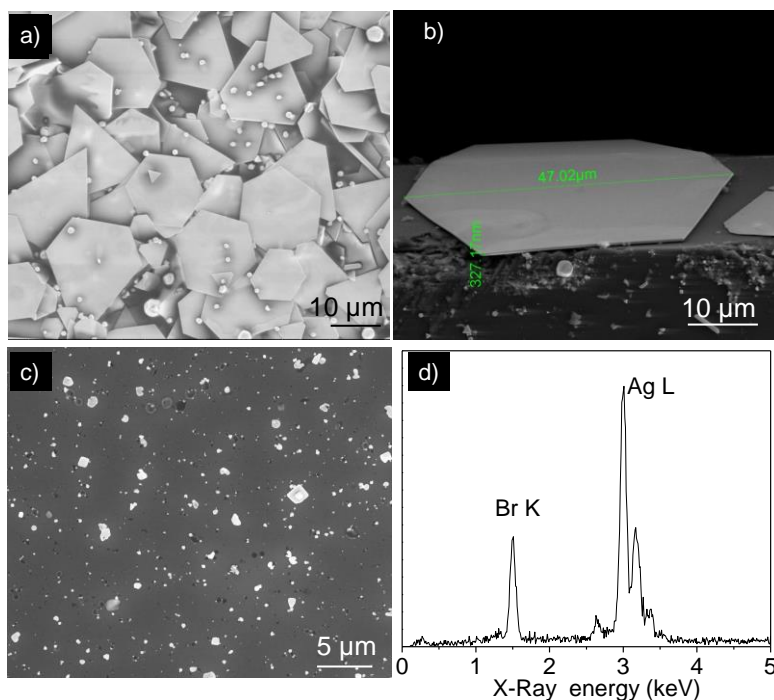


Figure 5.3 (a) Low magnification SEM image of Au polygons obtained by the thermolysis of AuToABr (without Ag) at 135 °C. (b) A magnified image of a polygon. (c) SEM image of the product obtained by the thermolysis of AgToABr (without Au) at 135 °C for 11 hrs. (d) EDS spectrum collected from a crystal confirms that the product is AgBr.

Anisotropic structures of Au reported in the literature are usually obtained via solution phase synthesis, upon reduction of metal ions stabilized with a suitable surfactant, in the presence of Ag(I) ions (5, 6). The latter is understood to play a key role in producing high index planes

resulting in interesting morphologies (33, 34). Nevertheless, these are seed-mediated multistep reactions (19) employing high concentrations of surfactants (21) or highly acidic conditions to control the growth (8).

The method, presented in this chapter, makes use of Ag(I) but not in solution phase. It is essentially a simple, single step solid state synthesis on a flat substrate, in which a precursor, i.e., a mixture of Au(III) and Ag (I) stabilized by tetraoctylammonium bromide (ToABr) named as AuAgToABr, is subjected to thermolysis on a hot plate in air, to produce long corrugated pentagonal bipyramidal microcrystals. The background, which led to this recipe, is interesting. Recently, some of us reported the synthesis of single crystalline Au microplates by the thermolysis of Au(III) stabilized with ToABr (AuToABr) (Figs 5.3(a, b)) (35). Similar attempts with AgToABr led to AgBr (Figs 5.3(c, d)) (36), as Ag-Br formation is thermodynamically more favorable than of Ag-Ag (37).

Upon drop coating a mixed precursor (75:25 of Au(III):Ag(I)) on a Si substrate and thermolyzing in air (see schematic in Fig. 5.4), there were no plate-like structures but instead micron sized long structures and symmetric 3D particles were obtained along with AgBr particles (Figs 5.4(b-d)). The latter could be washed away by treating with liquor ammonia. The focus of the present study is on the long micron sized anisotropic structures. As shown in the scanning electron microscopy (SEM) images in Fig. 5.4(e) and (f), the obtained structures are 10 ± 2 μm long. The central diameter was found to be in the range, 0.9–1.15 μm with a typical aspect ratio of ~ 7 (see histogram in Fig 5.4 (e)).

The magnified images in Figs. 5.4(f, g) and (h) bring out the interesting morphology of the long structures. They are tapered on both sides, from the center to the tips and the tapering is not smooth but corrugated. The tips are sharp with a radius of curvature of, 55 nm and a tip angle of $\sim 30^\circ$ (Fig 5.4(g)).

The contiguous corrugated features appear akin to folded fingers (Fig 5.4(h)). A side view reveals that the corrugated steps are approximately arranged in a pentagonal symmetry (Fig 5.4(i)) along the long axis. These interesting structures are termed as micron sized corrugated pentagonal bipyramids (μ -CPBs). Atomic force microscopy (AFM) topography image (Fig 5.4(j)) shows a well-defined stepped surface which is reflected in the height profile shown in Fig. 5.4(k). The width of the steps varied from, 180 nm at the tip to, 675 nm at the center. The surface

roughness on the flat regions of μ -CPB was minimal i.e., 1.5 nm. It is of considerable importance to have minimal surface roughness to alleviate the loss in light propagation studies (29).

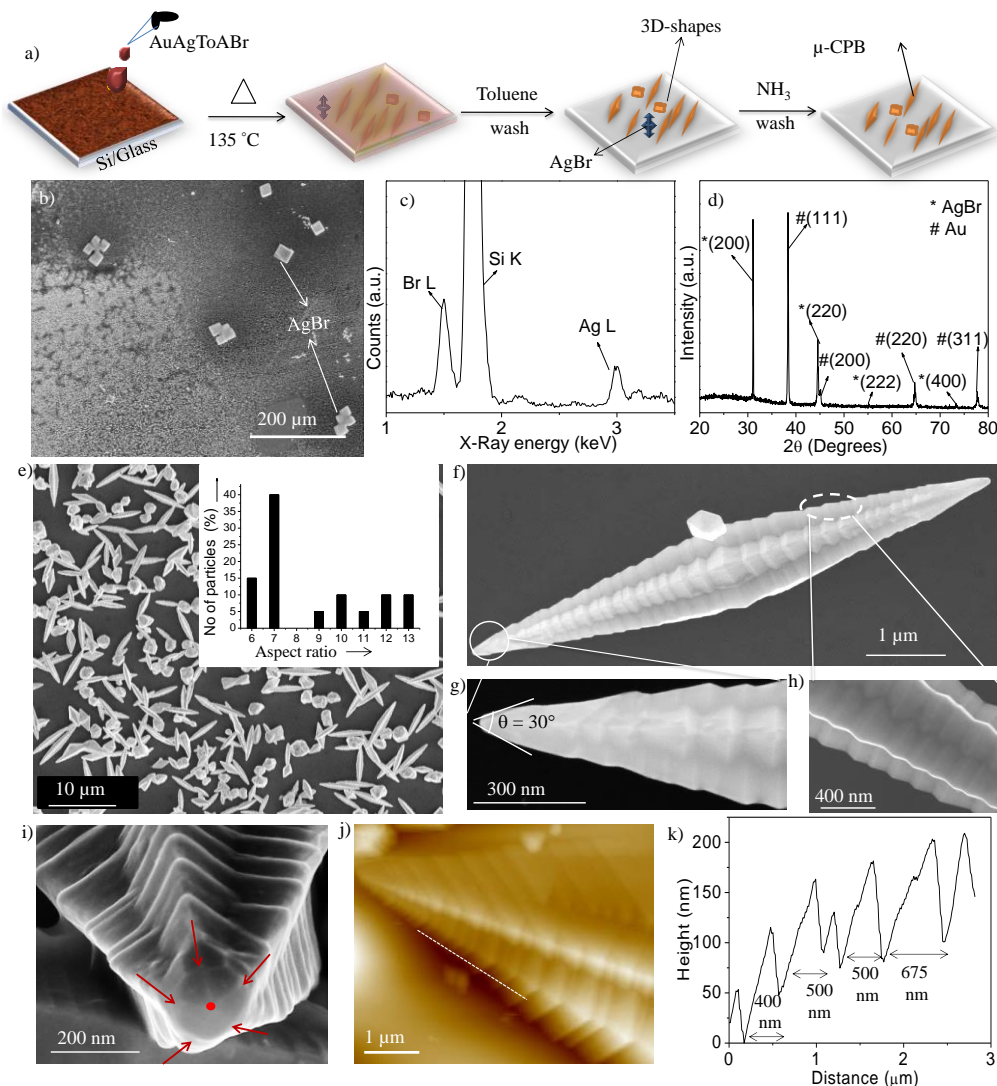


Figure 5.4 (a) Schematic illustrating the synthesis of μ -CPBs. SEM images of μ -CPBs prepared at 135 °C for 75:25 of Au(III):Ag(I) – (b) low magnification showing AgBr microcrystals and their EDS spectrum (c). (d) XRD pattern collected from as prepared sample. SEM image view showing (e) the collection of various shaped Au crystals, (f) single μ -CPB, (g) magnified view of the tip and (h) side facets marked in (f). (i) High resolution image of the pentagonal symmetry at the tip. (j) AFM topography image of the stepped surface of a μ -CPB and (k) height profile along the line drawn in (j). Inset in e shows the variation in the aspect ratio of long structures (μ -CPBs).

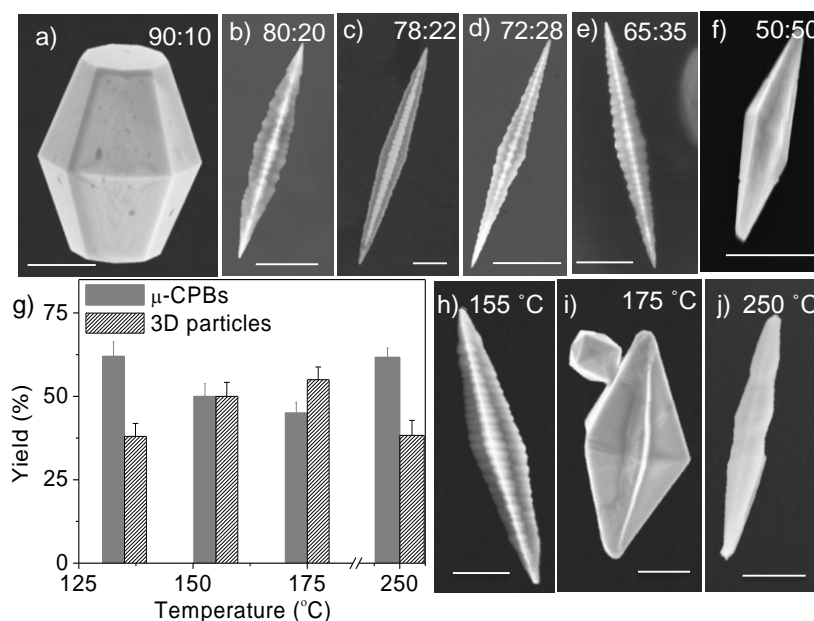


Figure 5.5 (a–f) SEM images of μ -CPBs prepared with different mole ratios of Au(III) and Ag(I) at 135 °C. (g) Histograms showing the relative populations of μ -CPBs and 3D particles obtained for various thermolysis temperatures (Au(III):Ag(I) ratio, 75:25). Error bars represent standard deviations in the yields. (h–j) SEM images of μ -CPBs obtained at various thermolysis temperatures. All scale bars correspond to 1 μ m.

The morphology of μ -CPBs and their relative population to other 3D particles depend on the Au(III):Ag(I) ratio in the precursor as well as on the thermolysis temperature (Fig 5.5). Elongated structures were observed when Au(III):Ag(I) = 90:10 ratio was employed (Fig 5.5(a)). They appear as dumbbells with pentagonal symmetry with flattened smooth edges; and the average length was found to be, 3 μ m. The average length increased to ~ 3.5 μ m with 80:20 of Au(III):Ag(I) and the elongated structures (see Fig 5.5(b)) resembled closely μ -CPBs obtained with the 75:25 ratio (Fig 5.4). The surface morphology was found to be sensitive in this concentration region (see Fig 5.5(c–e)). At 50:50, the pentagonal bipyramids possess small length (1.5 μ m) with smooth surface (Fig 5.5(f)). From the above experiments, it is clear that 75:25 of Au(III):Ag(I) produced the longest particles (μ -CPBs) with well-developed corrugations.

It is noteworthy that the μ -CPBs produced in this study are distinct from the nanorice/bipyramidal particles reported in the literature (5, 7, 38), the latter being typically sub- μ m in length. As μ -CPBs are few micrometers in length, they can be easily visualized and

manipulated under a conventional optical microscope (see Fig 5.6) unlike the nanorice/bipyramids.

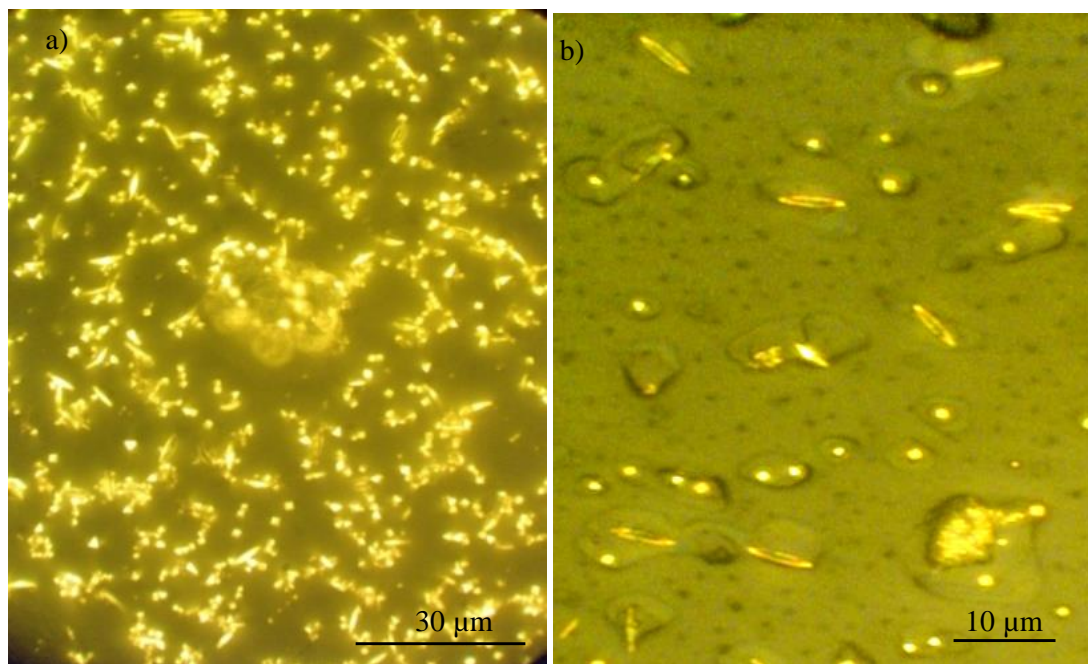


Figure 5.6 a-b, Optical microscopy images of μ -CPBs at different magnifications.

Besides the metal content, thermolysis temperature was found to be a crucial parameter for controlling the structure of μ -CPBs. The histogram in Fig. 5.5(g) shows the relative yields of μ -CPBs and 3D structures as a function of thermolysis temperature. μ -CPBs yield is above 45% at all temperatures. The thermogravimetric analysis indicates that there is no weight loss below 135 °C and the precursor decomposition is rapid above 170 °C (see Fig 5.2(c)). The length and morphology of μ -CPBs are influenced by the rate of precursor decomposition; slower the decomposition, longer the μ -CPBs. At 135 °C and 155 °C, long μ -CPBs with sharp tips were observed, while short pentagonal bipyramids with blunt tips and smoother surfaces are seen at higher temperatures (see Fig. 5.5(i) and (j)). The ones observed at 175 °C (see Fig. 5.5(i)) are bipyramids which possess similar morphology as reported in ref (15). The μ -CPBs prepared at 250 °C (see Fig. 5.5(j)) resemble the nanorods morphology reported in the literature (38). Thus, higher growth kinetics does not seem to permit the formation a well corrugated surface. A higher reduction rate at elevated temperatures leads to large number of nucleation sites and in turn, a large number of smaller particles.

5.4.3 Structure of μ -CPB

In order to understand the structure of the μ -CPBs in detail, X-ray diffraction (XRD), SEM and transmission electron microscopy (TEM) analysis have been performed. The μ -CPBs are highly crystalline as evident from the XRD pattern (Fig 5.4(d)). Low magnification TEM image (Fig 5.7(a)) shows the corrugated surface of a μ -CPB. Electron diffraction (ED) pattern collected from the tip showed two sets of spots (see Fig 5.7(b), hexagonal and rhombus patterns overlapping each other. These correspond to the Au FCC lattice viewed along the $\langle 111 \rangle$ and $\langle 110 \rangle$ zone axes, respectively. The ED pattern from the center of μ -CPB also shows two sets of spots indexable to $\langle 112 \rangle$ and $\langle 001 \rangle$ zone axes (see Fig. 5.7(c)). Similar ED patterns have been observed in the case of penta-twinned Au, Ag and Cu nanorods (39). This indicates that the μ -CPBs possess a penta-twinned structure grown along the $\langle 110 \rangle$ direction. When high resolution TEM (HRTEM) was performed at the tip, the observed spacing between the fringes was $\sim 2.36 \text{ \AA}$ corresponding to a d-spacing of Au(111) (see Fig. 5.7(d)). Figure 5.7(e) shows HRTEM image collected from the region of the side facets of μ -CPBs (indicated as e in Fig. 5.7(a)). The d-spacing was $\sim 2.07 \text{ \AA}$ corresponding to Au(200). The zig-zag ridges cannot be the (100) planes as the latter are atomically flat. The values of the angles at the ridges point to plausible existence of high-index planes. From the TEM image (Fig 5.7(f)), the angles subtended by the surface planes of the adjacent ridges are measured to be 147.1° and 146.8° , which are in close agreement with expected angular relation for the (730) and (610) ($\angle\alpha=147.3^\circ$) and, (210) and (910) ($\angle\beta=147.09^\circ$) (see Table 5.2).

To further confirm the assignments, one may refer to the projection angles in edge-on orientation along the $\langle 110 \rangle$ axis (see Table 5.2 and Fig. 5.7(g). Considering the ridges to be extraneous growth from the atomically flat (100) planes, the measure edge-on projection angles indicate that the ridges are $\{hk0\}$ (see Tables 5.2 and 5.3 and Figs. 5.7(f) and (g)) (where $h>1$ and $k\geq 1$) type high-index planes (7). Based on the above results, the growth direction of the μ -CPBs is considered to be $\langle 110 \rangle$ while the side facets are (100). The tips are enclosed with stable $\{111\}$ facets, in agreement with the reported literature on Au nanorice (5, 7). Figure 5.7(h) shows a highly magnified SEM image of a μ -CPB with various planes and growth directions assigned, based on ED and HRTEM analysis.

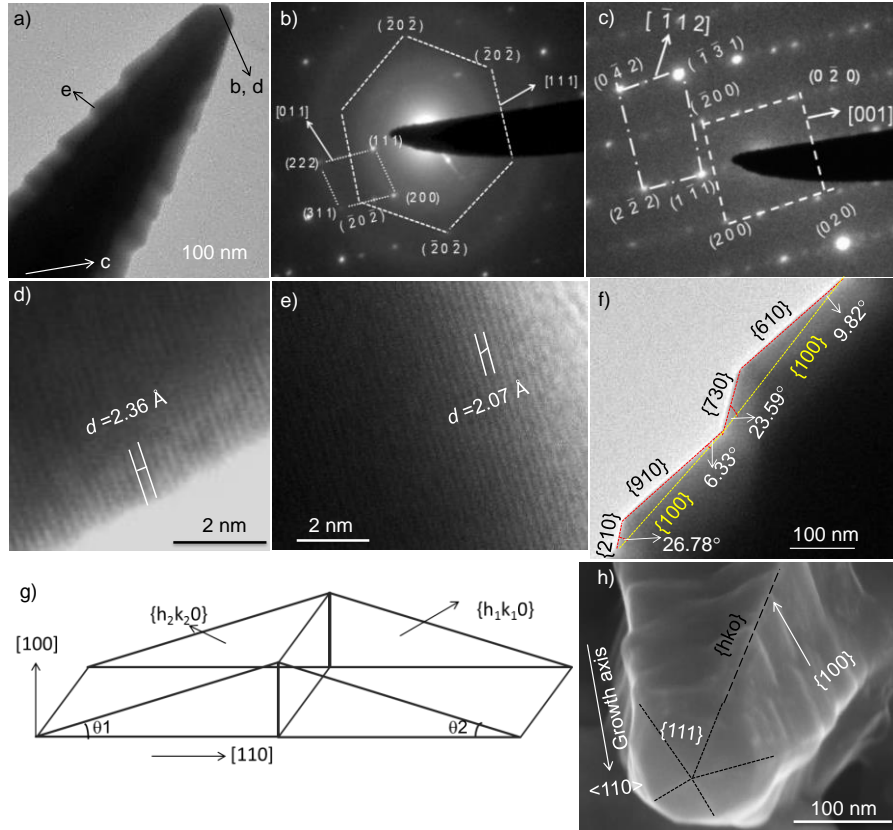


Figure 5.7 (a) TEM image of μ -CPB showing corrugated steps. ED patterns from μ -CPB's (b) tip and (c) center are shown. HRTEM images from the (d) tip and (e) side edges of μ -CPBs are shown along with the d-spacings marked corresponding to (111) and (200) respectively. (f) Magnified TEM image of a μ -CPB, showing ridges made of $\{hk0\}$ type high index facets. (g) A schematic illustration of a ridge bound by high index facets and (h) a magnified SEM image of a μ -CPB with the facets indexed.

Facet-I	Facet-II	Measured angle ($^{\circ}$)	Theoretical angle ($^{\circ}$)
{730}	{610}	147.1	147.34
{210}	{910}	146.8	147.09
{100}	{610}	9.82	9.46
{100}	{730}	23.5	23.2
{100}	{910}	6.33	6.2
{100}	{210}	26.7	26.57

Table 5.2 Angular relation between various facets.

Facet	Notation
{610}	Au(S)-[6(100)x1(110)]
{210}	Au(S)-[2(100)x1(110)]
{910}	Au(S)-[9(100)x1(110)]
{730}	Au(S)-[1(520)x1(210)]

Table 5.3 Micro facet notation of various facets.

For a Miller indices (n10), n(100)x(110) is the notation. The contribution of {100} is predominate in constructing {hk0} type high index planes.

The surface composition of μ -CPBs was examined using core-level spectroscopy (see Fig. 5.8). Interestingly, the surface was found to be almost entirely made of Au(0), Ag(0) being negligible. The metal-organic precursor contains Ag(I) ions which guide the Au microcrystal growth. In the absence of Ag(I) in the precursor, only Au plate-like fcc crystallites get formed. With Ag(I) in the precursor, bipyramidal-like morphology is found even under milder thermolysis temperature. Ag plays multiple roles in obtaining bipyramids.

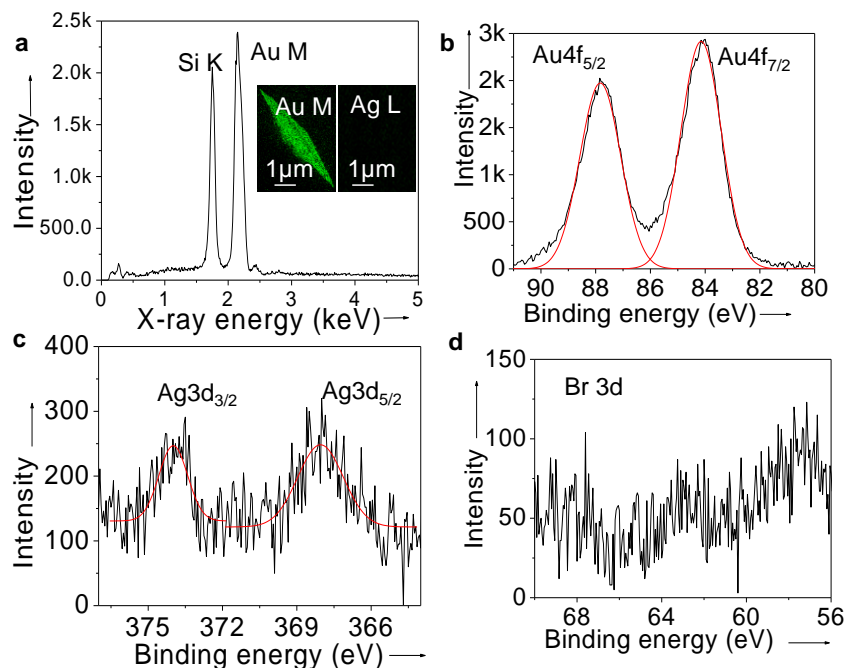


Figure 5.8 (a) EDS spectrum collected from a μ -CPB. EDS maps obtained for Au M and Ag L levels are shown in the insets. Core level photoelectron spectra in the regions of (b) Au 4f, (c) Ag

3d, (d) Br 3d. The μ -CPBs obtained with Au(III):Ag(I) of 75:25. The C1s (284.4 eV) signal was used for energy calibration

i. Enhancing the penta-twinned nucleation: Thermolysis of precursor devoid of Ag(I) produces cuboctahedron and its derivatives such as hexagonal plates, triangles and truncated octahedrons in a major proportion (~ 90%) while the penta twinned decahedrons and nanorods being the side products (~ 10%) (Fig 5.9). On the other hand, when Ag(I) is a part of the precursor, penta-twinned bipyramids shaped particles are the major product (~ 60%). The preferential deposition of Ag on Au{100} facets due to the higher coordination number and lower under potential deposition, stabilizes the Au decahedrons. Therefore, it is understood that Ag(I) assists the stabilization of penta-twinned particles. However, more detailed study is required in understanding how Ag(I) promotes the penta-twinned nucleation.

ii. Providing tapered geometry: While Ag(I) promotes penta-twinned growth, it does not lead to a Au nanowire with uniform diameter (like penta-twinned Ag nanowires described in the literature). Instead bipyramidal-like morphology is seen which is a result of diminishing concentration of Ag(I) in the reaction mixture. As the reaction progresses, more and more Ag(I) gets consumed depositing on the {100} facets due to the under potential deposition (UPD). If it were not the case, one would have expected penta-twinned nanowire like crystallites without tapering towards the tips.

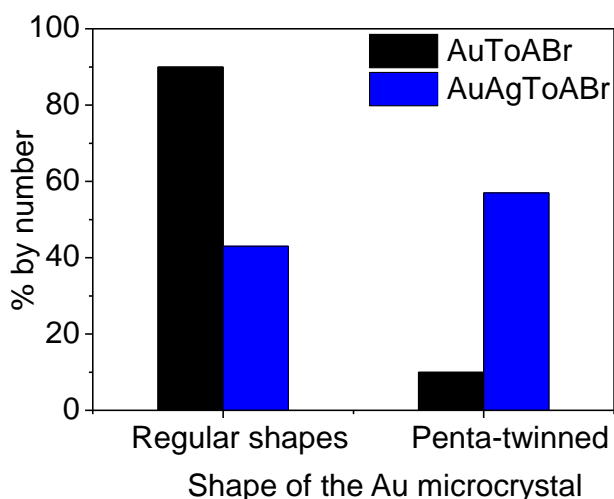


Figure 5.9 Relative percentage of Au microcrystals obtained from AuToABr and AuAgToABr precursors.

iii. Stabilization of high index facets: Corrosive reagents, O_2/X ($x=Cl, Br$), etch the metal surface and produce corrugated surface (40) that stabilized by a monolayer or sub monolayer of Ag.

5.4.4 Growth mechanism

The growth of μ -CPBs is indeed interesting. A μ -CPB has two growth modes namely along the longitudinal axis and the lateral growth leading to the observed corrugation (five-fold stars stacked along the longitudinal growth direction). These aspects were investigated by arresting the growth of μ -CPBs at different time periods by simply removing the substrate from the hot plate and examining under SEM. Initially, the growth along $\langle 110 \rangle$ direction is discussed. The thermolysis carried out for 30 min gave rise to nearly spherical particles in the range, 25 - 30 nm (see Fig. 5.10). The particles may have definite facets which is however not clearly visible in the SEM images owing to their small size.

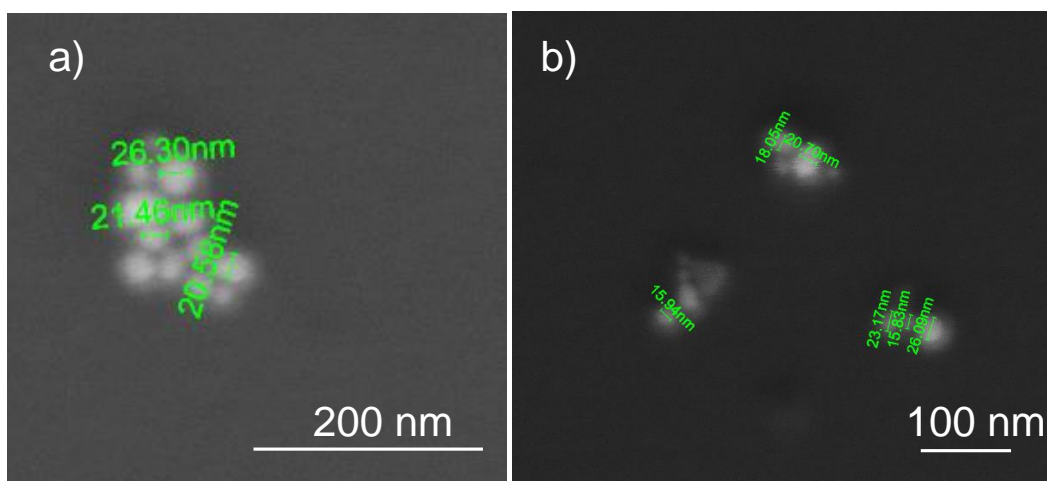


Figure 5.10 (a-b) SEM images collected at different magnifications after 30 min thermolysis. Irregular shaped Au nanoparticles with 20-30 nm were observed.

The facets become visible once the particles grew beyond 100 nm (time of thermolysis, 60 min). At this point, the particle is essentially a multiply twinned decahedron (MTD) (see Fig. 5.11(b) and its schematic in Fig. 5.11(a)) which is one among the known stable polyhedrons in this size regime (41). It has ten $\{111\}$ facets, five $\{100\}$ facets and two possible growth directions, $\langle 110 \rangle$ i.e., along the particle axis and also along five equivalent $\langle 112 \rangle$ directions across the particle

side faces (42) as shown in Fig. 5.11(a). Anisotropic particle growth is mainly due to the differences in the growth rates on different crystallographic facets. For FCC metals, the surface energy of different facets is as follows, $\gamma_{\{111\}} < \gamma_{\{100\}} < \gamma_{\{110\}}$. The $\{110\}$ and $\{211\}$ faces have surface energies of 0.0991 and 0.0908 eV/Å² respectively. Hence a faster growth along the $\langle 110 \rangle$ direction is expected (43). The growth rate along the $\langle 112 \rangle$ direction comes next (42). There is another contributing factor for the anisotropic structure of the μ -CPB. MTD is viewed as an association of five tetrahedral units, sharing an edge. The angle expected between two tetrahedral units is 70.53°. When five such tetrahedrons are stacked in a face-to-face orientation, there will be an angular gap of 7.35° to fill in (44). It therefore causes strain at the corners, which in turn induces anisotropic growth of μ -CPBs. MTD may act as a seed for further growth and this aspect is discussed in detail in the literature in relation to Au/Ag anisotropic structures (45). In the given reaction mixture, the following reactions are expected where the described redox potentials are with respect to the standard hydrogen electrode (SHE).



Following equations 1 and 2, Ag(0) oxidizes to Ag(I) and generates an electron (46, 47). Au ions get reduced by accepting the electrons according to equation 3. It is therefore not surprising that no significant Ag3d signal was observed in X-ray photoelectron spectrum (XPS).

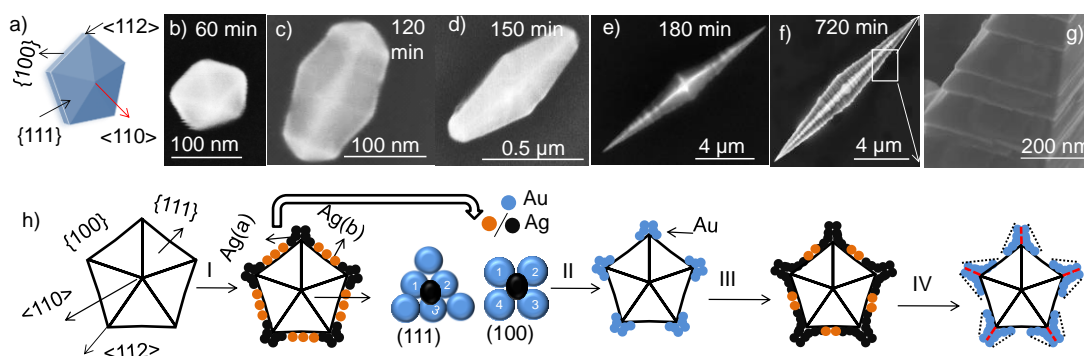


Figure 5.11 (a) Schematic of decahedron with facets and growth directions marked. (b-f) FESEM images of typical μ -CPBs collected at different time periods during thermolysis at 135°C. (g) side view of the μ -CPB. (h) Schematic depicting growth along $\langle 112 \rangle$ directions involving Ag(I) deposition on Au facets and galvanic displacement of Ag(0) by Au(I) from the

surrounding molten precursor. This process eventually leads to the fivefold star shape as seen along the $\langle 110 \rangle$ direction.

As shown in Fig. 5.11(c), nanoparticles obtained at 120 min thermolysis appear like elongated decahedrons. Similar structures are addressed as nanorice in the literature. They have a typical length of ~ 150 nm and an aspect ratio ~ 2 . In the subsequent growth, the aspect ratio of the decahedron increased by many folds (see Fig. 5.11(d) corresponding to 150 min thermolysis). In stage 5.11d, the nanoparticles became tapered with a large curvature. The intense electric field associated at the tip helps rapid reduction of Au(I) and Au(III) at the tip (48), favouring the tapered growth. Also, the electron liberated from Ag oxidation (see equations 1 and 2) moves to the tip of the μ -CPB particle, which leads to reduction of Au ions present in the reaction medium at the tip (see equation 3) (7). These processes lead to a relatively fast kinetics for longitudinal growth, thus eventually forming μ -CPBs (see SEM images in Figs. 5.11(e) and (f)). This is clear from the histogram in Fig. 5.12, which shows the mean length of μ -CPBs as a function of growth time.

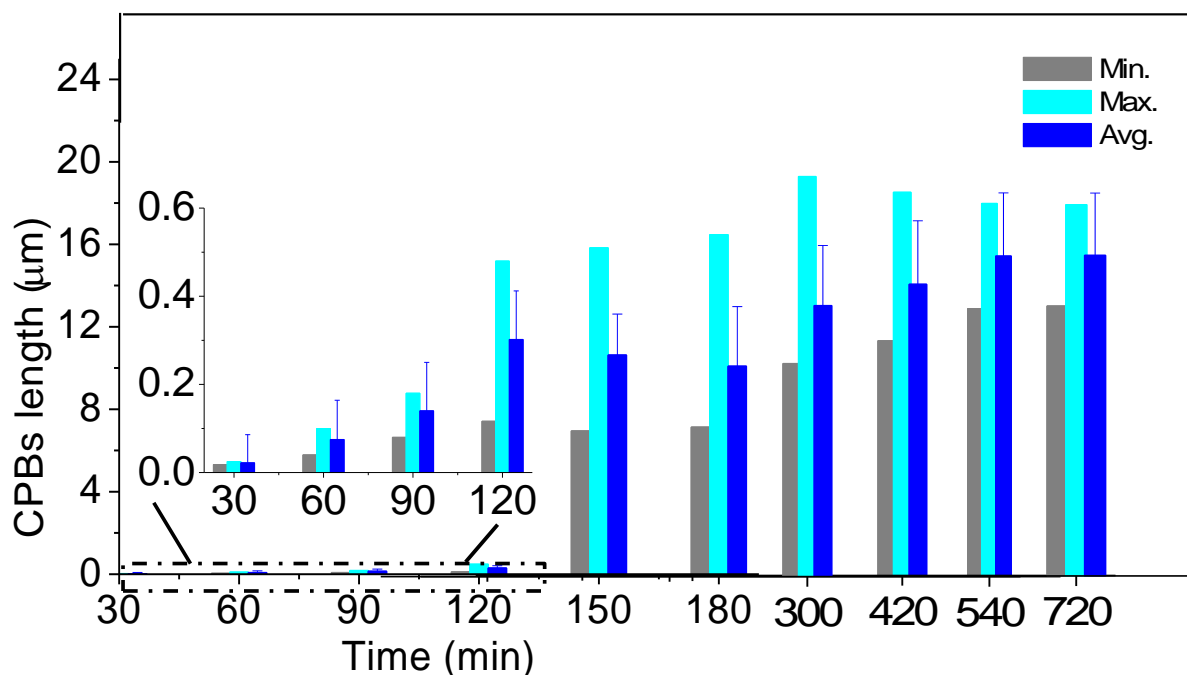


Figure 5.12 Histogram representing μ -CPBs growth as a function of time. The data from the 30-120 minutes period is magnified and shown in the inset. Error bars represent standard deviation in the length of μ -CPBs.

The discussion below is related to the growth of μ -CPB along the $\langle 112 \rangle$ direction. On the decahedron, the strained corners act as reactive sites to generate ridges-like extra growth. As shown in Fig. 5.11(h), the twin planes are oriented in the $\langle 112 \rangle$ direction. Ag(I) from precursor deposits preferentially on the Au{100} facets due to its lower deposition potential. On this plane, Ag finds higher coordination than on {111} (see Fig. 5.11(h)) (6). Ag(0) present on the Au{100} facets (indicated by brown colored circles in Fig. 5.11(h)) could be oxidized by a bromide ion present in the reaction mixture, leading to discharge of an electron (equation 2) (7) and release of AgBr. On the other hand, Ag(0) present at the boundary line where {100} facets meet (shown as black circles in Fig. 5.11(h)), gets galvanically displaced by Au(I) and thus stabilizes the energetic twin plane (49). This may lead to the growth of a star shape from a decahedron. The deposition and dissolution of Ag and the galvanic displacement of Au along the $\langle 112 \rangle$ directions take place repeatedly to produce well-defined star shaped Au petals on a decahedron base. These ridges are high index planes as shown in the TEM analysis. Growth mechanism along the $\langle 112 \rangle$ direction is shown in Fig. 5.11(h). The ridges along the $\langle 112 \rangle$ directions are the corrugated structures observable from the top view of the μ -CPBs (Fig 5.11(g)). Growth along the $\langle 110 \rangle$ and $\langle 112 \rangle$ contribute simultaneously to produce longer pentagonal bipyramids with corrugated surfaces. Ultra-slow precursor decomposition at 135 °C is also an important contributing factor. At higher temperatures, the differences in the growth rates in different directions may be small. The ten {111} facets at the tip remain almost unaffected from the seed decahedron to μ -CPBs as the growth on these planes is thermodynamically unfavourable. The longitudinal growth along the growth axis is relatively rapid whereas the side facets i.e., {100} are adsorbed with Ag which acts as a surfactant and thus the growth is inhibited. While Ag actively participates in the Au μ -CPBs growth, it does not become part of it. Following the Hume–Rothery rules (50), one would expect an alloy formation, as Ag has similar lattice parameters. Not quite surprisingly, Au-Ag alloy bipyramids (40–90 nm) have been reported in the literature starting with HAuCl₄, AgNO₃ and polyvinylpyrrolidone (PVP) as a capping agent (17). In the present method, clearly, Au and Ag though exist in atomic intimacy, did not form an alloy.

By virtue of such contributing factors at play, remarkably large multiply twinned particle (MTP) structures (Au μ -CPBs) have thus been observed which stand out from the known anisotropic structures till date. The MTP structures reported in literature are usually nanoparticles with decahedron or slightly elongated rice morphology else nanowires with five-fold tapered ends.

The μ -CPB particles reported here are unique in that the tips are made of MTP structure while the deeply corrugated surface is covered with high index facets. Large sized, micrometer to millimeter, MTP structures are not commonly reported in the literature. Penta twinned micron/millimeter size decahedrons and its derivative structures have been found under highly acidic conditions (51) but with little yield. Occasionally, they may be found in nature as well (52). Thus, the results presented here are of immense significance.

5.4.5 SERS, pick and probe measurements

The μ -CPBs host nanoscale topographic features in the form of ridges which form interesting sites for adsorption of molecules. Indeed, such confined nano-volumes act as plasmonic hot-spots where large electric fields can build up giving rise to enhanced light-molecule interaction such as SERS. The corrugated surface of the μ -CPB prompted us to use them as SERS substrates.

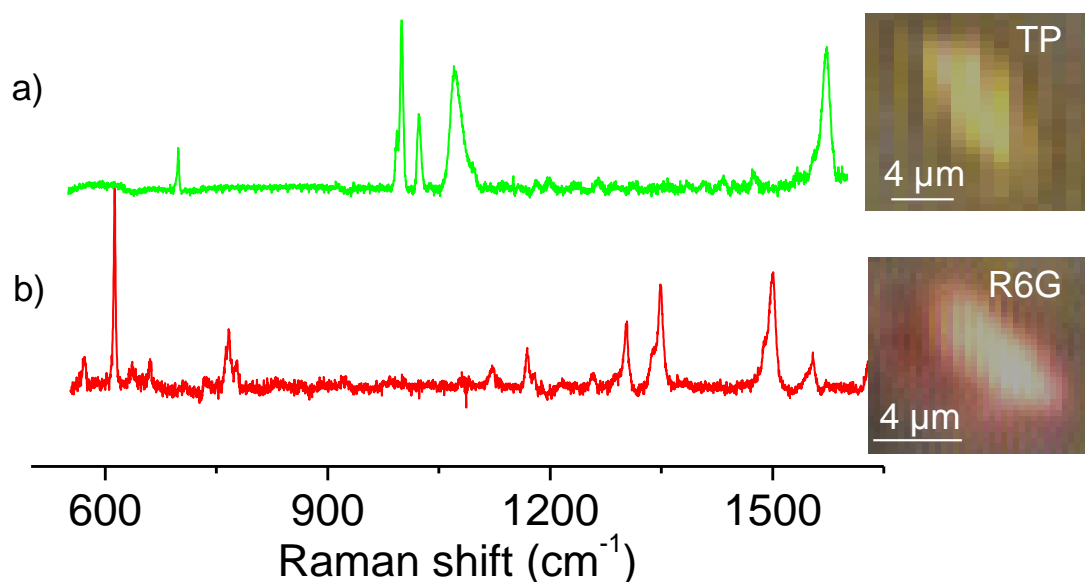


Figure 5.13 Raman spectra recorded from single μ -CPB adsorbed with the probe molecules; (a) thiophenol (TP) and (b) Rhodamine 6G (R6G). The optical images from the Raman spectrometer images are shown on the right. The μ -CPB particles were located on a glass substrate after treatment with the TP/ R6G solutions.

For this purpose, thiophenol (TP) (1 mM) and Rhodamine 6G (R6G) (1 mM) were used as Raman probe molecules. The Raman spectrum of TP recorded on an individual μ -CPB shown in Fig. 5.13(a), consists of intense peaks at 1000, 1023, 1070 and 1576 cm^{-1} , all assignable to various vibration modes in ring breathing, C-H bending, C-S stretching and C=C bond respectively of the aromatic ring (53). The Raman enhancement factor (G) calculated based on the peak intensity at 1576 cm^{-1} was found to be 4.4×10^6 for TP. In the spectrum shown in Fig. 5.13(b), the peaks are assignable to R6G vibrational modes; peak at 614 cm^{-1} corresponding to C-C stretching mode and the peaks at 1355 and 1509 cm^{-1} stand for the C-C stretching (54). Enhancement factor (also known as G-factor) was estimated to be 5.8×10^6 based on the peak at 614 cm^{-1} .

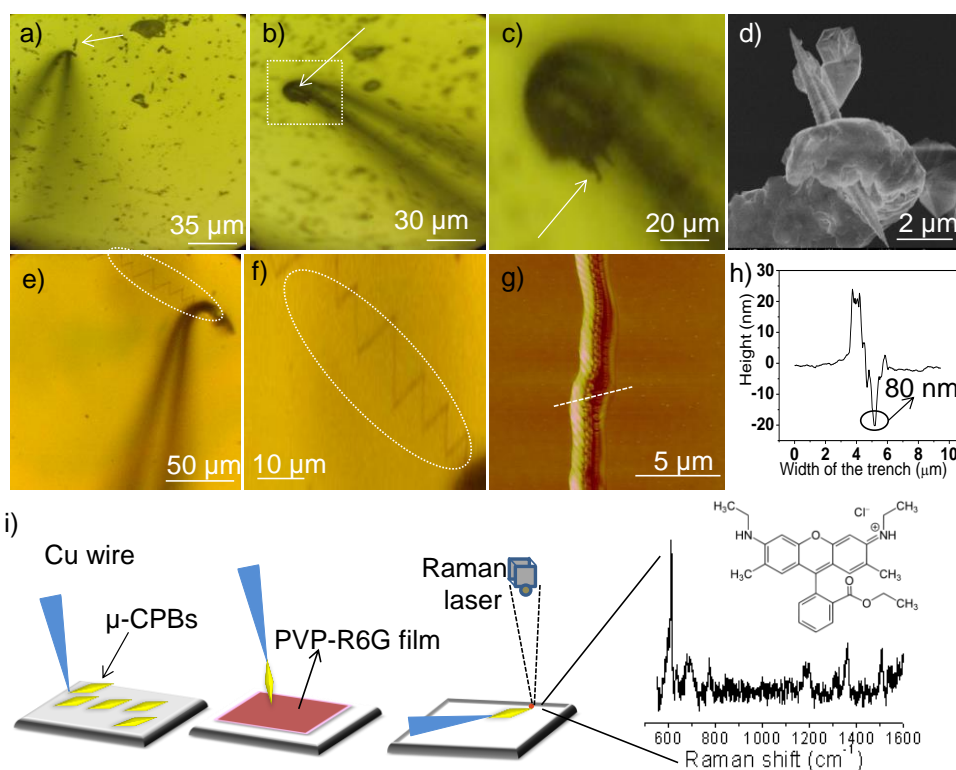


Figure 5.14 (a-c) μ -CPBs manipulation by a Cu wire on a Si substrate. Optical image showing (a) a Cu wire approaching the μ -CPB particle (shown by arrow), (b) μ -CPB held by the Cu wire and (c) shows a magnified view of the same. (d) FESEM image of a Cu wire carrying the μ -CPB, (e) zigzag line (marked by white circle) on a PVP-R6G film made by a μ -CPB carried by Cu wire (f) magnified view of zigzag line, (g-h) AFM image of zigzag line and its height profile

showing the depth of the line is ~ 20 nm and width of the line is ~ 80 nm which is roughly equal to tip of the μ -CPB ~ 60 nm. (i) Schematic illustration of pick and probe method.

Since μ -CPBs are sharp objects, the pick and probe technique was tried for molecules using single μ -CPB. A polymer (PVP) film containing probe molecules (R6G) was chosen, which was gently scratched with a μ -CPB mounted on a Cu wire using a micromanipulator (see Fig 5.14). A small amount of R6G-PVP blend was thus picked up on the μ -CPB tip. The spectrum collected from the tip of μ -CPB (see Fig. 5.14(i)) is relatively noisy and the peaks are broadened due to the inhomogeneous environment (55) of the analyte molecules on the μ -CPB surface. The number of adsorbed R6G molecules on the tip estimated based on the area of μ -CPB tip came out to be ~ 2700 . The above experiment illustrates the possibility of using μ -CPBs in sensitive SERS based detection.

5.4.6 Light propagation

The μ -CPBs were investigated for light propagation as they have corrugated, grating-type surface with minimal roughness at each step as well as tapered ends resembling tapered V-grooves (56). These structural features are important because the tips can facilitate localized optical fields while the corrugations on the surface facilitate effective conversion of free photons to surface plasmons with minimal scattering loss (57). With this hindsight, the plasmon assisted light propagation properties of Au μ -CPBs were tested. Figure 5.15(a) shows the dark-field optical image of an isolated Au μ -CPB. Upon focusing a 632.8 nm (2 μ m diameter) laser beam on one end of the Au μ -CPB (Fig 5.15(b)), out-coupling of light at the distal end of the microstructure was observed. This clearly indicated that the μ -CPB acts as a plasmonic waveguide. The incidence of visible light at one end of the structure causes the momentum of free photons convert into momentum of propagation plasmon polariton within the microstructure. This propagating plasmon reaches the distal end of the μ -CPB where again the plasmon polaritons are back-converted into free photons (see Figs. 5.15(b) and (c)).

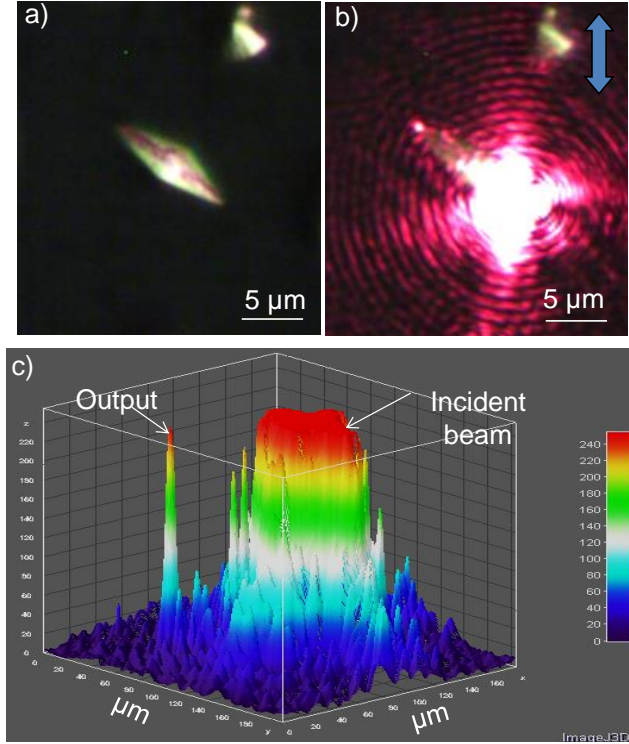


Figure 5.15 (a) Dark-field optical image of a μ -CPB. (b) Plasmon assisted light propagation at incident wavelength of 632.8 nm, the arrow indicates the polarization of the focused laser beam. (c) Three-dimensional projection of the image in b showing the incident beam and the out-coupled light at the distal end of the μ -CPB.

In order to quantify the performance of μ -CPBs as plasmon waveguides, the propagation loss was calculated for the structure. Propagation loss (α) is given by (58)

$$\alpha = (-10 \times \log(1/e)) / L_0 = 4.343 / L_0 \quad (4)$$

where L_0 is the propagation length, calculated using the formula

$$I(x) = I_0 \times \exp(-x / L_0) \quad (5)$$

where I_0 is the incident intensity, $I(x)$ is the intensity out-coupled light at distance x from the incident spot. For the Au μ -CPB of length 8.8 μm shown in Fig. 5.15(a), the calculated propagation loss was 2.32 dB/ μm . The propagation loss in the microstructure is both radiative

and ohmic. The nanoscale ridges may scatter the plasmon resulting in photon emission. One way to overcome the losses is to use smooth bipyramid-like structures (Fig. 5.15(a)), and further taper them down with a focused-ion beam or possibly by a chemical recipe. This will facilitate nano-tapered, single crystalline, low-loss plasmonic structures that can be utilized for efficient optical waveguiding. It is to be noted that ridges in our geometry do have an advantage as they can act as periodic hot-spots. Therefore, molecules confined to these ridges are subject to large electric fields. This can be further harnessed for sensitive detection of molecules at ultra-low concentrations. Furthermore, these microcrystals with controllable nanoscale features can be easily accessed and probed using far-field optical microscopy techniques. This is a major advantage when one needs to interface such structures with biological entities such as cells and tissues.

5.5 Conclusion

In conclusion, μ -CPBs were synthesized using a simple solid state synthesis route (i.e., unaided by any solvent). The current method is versatile in that it is a single step synthesis and can be carried out on almost any flat substrate that can withstand 130 °C with almost no organic impurities in the final product. The growth of μ -CPBs can be halted or resumed any time, by simply turning on and off the hot plate. The μ -CPBs being long enough can be easily observed using an ordinary optical microscope. Although the μ -CPBs are entirely made of Au, the presence of $(\text{AgBr}_2)^-$ ion in the reaction medium seems to play a key role in tuning the shape of the anisotropic particles. Shape and size of the μ -CPBs can be tailored by varying the mole ratio of Au(III) and Ag(I) in the precursor as well as by the thermolysis temperatures. The μ -CPBs serve as excellent SERS substrates. The efficiency of the tip of a μ -CPB was studied in a “pick and probe experiment”. The tip carrying only 2700 R6G molecules produced a measurable Raman signal. The tapered structure of μ -CPB facilitates concentration of the light at the tips with a propagation loss of 2.32 dB/ μm . Conventionally plasmonic nanoparticles that occupy small volumes are used for localized surface plasmon resonance, and one dimensional elongated structures such as plasmonic wires are utilized for optical waveguiding properties. The uniqueness of the geometry studied herein is that it can facilitate both localized and propagating plasmons on a single platform. As a ‘proof-of-concept’, the prepared nanostructures were harnessed for both surface enhanced Raman scattering which is a property based on localized

plasmons, and plasmon-assisted optical waveguiding which is based on propagating plasmon-polaritons. While the focus of the present study is on one anisotropic structure, the approach need not necessarily be limited; such synthetic routes involving single source precursors hold great promise for the synthesis of exotic anisotropic materials.

References

1. C. J. Murphy, T. K. Sau, A. M. Gole, C. J. Orendorff, J. Gao, L. Gou, S. E. Hunyadi, T. Li, *J Phys Chem B* **109**, 13857-13870 (2005).
2. A. Tao, F. Kim, C. Hess, J. Goldberger, R. He, Y. Sun, Y. Xia, P. Yang, *Nano Lett* **3**, 1229-1233 (2003).
3. Yu, S.-S. Chang, C. L. Lee, C. R. C. Wang, *J Phys Chem B* **101**, 6661-6664 (1997).
4. Y. Xia, Y. Xiong, B. Lim, S. E. Skrabalak, *Angew Chem Int Edit* **48**, 60-103 (2009).
5. X. Kou, W. Ni, C. K. Tsung, K. Chan, H. Q. Lin, G. D. Stucky, J. Wang, *Small* **3**, 2103-2113 (2007).
6. Liu, P. Guyot Sionnest, *J Phys Chem B* **109**, 22192-22200 (2005).
7. Y. Zheng, J. Tao, H. Liu, J. Zeng, T. Yu, Y. Ma, C. Moran, L. Wu, Y. Zhu, J. Liu, Y. Xia, *Small* **7**, 2307-2312 (2011).
8. M. Pelton, J. E. Sader, J. Burgin, M. Liu, P. Guyot-Sionnest, D. Gosztola, *Nat Nano* **4**, 492-495 (2009).
9. J. Burgin, M. Liu, P. Guyot-Sionnest, *J Phys Chem C* **112**, 19279-19282 (2008).
10. L. Rodríguez-Lorenzo, R. A. Álvarez Puebla, F. J. G. de Abajo, L. M. Liz-Marzán, *J Phys Chem C* **114**, 7336-7340 (2010).
11. N. Liu, M. L. Tang, M. Hentschel, H. Giessen, A. P. Alivisatos, *Nat Mater* **10**, 631-636 (2011).
12. W. Hasan, C. L. Stender, M. H. Lee, C. L. Nehl, J. Lee, T. W. Odom, *Nano Lett* **9**, 1555-1558 (2009).
13. H. Liang, H. Yang, W. Wang, J. Li, H. Xu, *J Am Chem Soc* **131**, 6068-6069 (2009).
14. L. Vigderman, E. R. Zubarev, *Langmuir* **28**, 9034-9040 (2012).
15. D. Senapati, A. K. Singh, P. C. Ray, *Chem Phys Lett* **487**, 88-91 (2010).
16. N. R. Jana, L. Gearheart, S. O. Obare, C. J. Murphy, *Langmuir* **18**, 922-927 (2002).

17. X. Zhang, M. Tsuji, S. Lim, N. Miyamae, M. Nishio, S. Hikino, M. Umezu, *Langmuir* **23**, 6372-6376 (2007).
18. S. Zhang, X. Kou, Z. Yang, Q. Shi, G. D. Stucky, L. Sun, J. Wang, C. Yan, *Chem Commun*, 1816-1818 (2007).
19. H.-L. Wu, C. H. Chen, M. H. Huang, *Chem Mater* **21**, 110-114 (2009).
20. H. M. Chen, R.-S. Liu, D. P. Tsai, *Cryst Growth Des* **9**, 2079-2087 (2009).
21. S. Lee, K. M. Mayer, J. H. Hafner, *Anal Chem* **81**, 4450-4455 (2009).
22. M. M. Kathryn, H. Feng, L. Seunghyun, N. Peter, H. H. Jason, *Nanotechnology* **21**, 255503 (2010).
23. H. Wang, D. W. Brandl, F. Le, P. Nordlander, N. J. Halas, *Nano Lett* **6**, 827-832 (2006).
24. T. T. Tran, X. Lu, *J Phys Chem C* **115**, 3638-3645 (2011).
25. E. Carbo-Argibay, B. Rodriguez-Gonzalez, I. Pastoriza-Santos, J. Perez-Juste, L. M. Liz-Marzan, *Nanoscale* **2**, 2377-2383 (2010).
26. H. Chen, L. Shao, K. C. Woo, T. Ming, H.-Q. Lin, J. Wang, *J Phys Chem C* **113**, 17691-17697 (2009).
27. M. I. Stockman, *Phys Rev Lett* **106**, 019901 (2011).
28. W. Hasan, J. Lee, J. Henzie, T. W. Odom, *J Phys Chem C* **111**, 17176-17179 (2007).
29. P. Nagpal, N. C. Lindquist, S.-H. Oh, D. J. Norris, *Science* **325**, 594-597 (2009).
30. S. Vedantam, H. Lee, J. Tang, J. Conway, M. Staffaroni, E. Yablonovitch, *Nano Lett* **9**, 3447-3452 (2009).
31. H. L. Offerhaus, B. van den Bergen, M. Escalante, F. B. Segerink, J. P. Korterik, N. F. van Hulst, *Nano Lett* **5**, 2144-2148 (2005).
32. N. C. Lindquist, P. Nagpal, A. Lesuffleur, D. J. Norris, S.-H. Oh, *Nano Lett* **10**, 1369-1373 (2010).
33. T. Ming, W. Feng, Q. Tang, F. Wang, L. Sun, J. Wang, C. Yan, *J Am Chem Soc* **131**, 16350-16351 (2009).
34. M. L. Personick, M. R. Langille, J. Zhang, C. A. Mirkin, *Nano Lett* **11**, 3394-3398 (2011).
35. B. Radha, M. Arif, R. Datta, T. Kundu, G. Kulkarni, *Nano Res.* **3**, 738-747 (2010).
36. G. Mettela, S. Siddhanta, C. Narayana, G. U. Kulkarni, *Nanoscale* **6**, 7480-7488 (2014).

37. B. d. Darwent, [Washington] U.S. National Bureau of Standards; for sale by the Supt. of Docs., U.S. Govt. Print. Off., 1970., (1970).
38. Z.-Y. Zhou, N. Tian, Z.-Z. Huang, D. J. Chen, S. G. Sun, *Faraday Discuss* **140**, 81-92 (2009).
39. C. J. Johnson, E. Dujardin, S. A. Davis, C. J. Murphy, S. Mann, *J Mater Chem* **12**, 1765-1770 (2002).
40. Z.-c. Zhang, F. Nosheen, J. c. Zhang, Y. Yang, P.-p. Wang, J. Zhuang, X. Wang, *ChemSusChem* **6**, 1893-1897 (2013).
41. J. L. Elechiguerra, J. Reyes-Gasga, M. J. Yacaman, *J Mater Chem* **16**, 3906-3919 (2006).
42. M. Tsuji, P. Jiang, S. Hikino, S. Lim, R. Yano, S.-M. Jang, S. H. Yoon, N. Ishigami, X. Tang, K. S. N. Kamarudin, *Colloids and Surfaces A: Physicochemical and Engineering Aspects* **317**, 23-31 (2008).
43. C. Kan, C. Wang, H. Li, J. Qi, J. Zhu, Z. Li, D. Shi, *Small* **6**, 1768-1775 (2010).
44. M. Tsuji, M. Ogino, R. Matsuo, H. Kumagae, S. Hikino, T. Kim, S. H. Yoon, *Crystal Growth & Design* **10**, 296-301 (2010).
45. D. Seo, J. H. Park, J. Jung, S. M. Park, S. Ryu, J. Kwak, H. Song, *J Phys Chem C* **113**, 3449-3454 (2009).
46. Y. Sun, *Nanoscale* **2**, 1626-1642 (2010).
47. H. H. Hassan, M. A. M. Ibrahim, S. S. Abd El Rehim, M. A. Amin, *International Journal of Electrochemical Science* **5**, 278-294 (2010).
48. J. Pérez-Juste, L. M. Liz-Marzán, S. Carnie, D. Y. C. Chan, P. Mulvaney, *Adv Funct Mater* **14**, 571-579 (2004).
49. G. W. Sławiński, O. S. Ivanova, F. P. Zamborini, *Langmuir* **27**, 13293-13301 (2011).
50. Raghavan.
51. C. H. Gammons, *Can Mineral* **34**, 1-8 (1996).
52. S. Dana Edward, in *Zeitschrift für Kristallographie - Crystalline Materials*. (1887), vol. 12, pp. 275.
53. C. E. Taylor, J. E. Pemberton, G. G. Goodman, M. H. Schoenfish, *Appl Spectrosc* **53**, 1212-1221 (1999).
54. D. Y. Wang, T. S. Teng, Y. C. Wu, Y. C. Lee, K. H. Chen, C. H. Chen, Y. C. Chang, C. C. Chen, *J Phys Chem C* **113**, 13498-13504 (2009).

55. K. Kneipp, Kneipp, H. & Bohr, H., **103**, 261–277 (Springer Berlin/Heidelberg, 2006).
56. J. Beermann, S. M. Novikov, T. Søndergaard, J. Rafaelsen, K. Pedersen, S. I. Bozhevolnyi, *J Opt Soc Am B* **28**, 372-378 (2011).
57. B. Wild, L. Cao, Y. Sun, B. P. Khanal, E. R. Zubarev, S. K. Gray, N. F. Scherer, M. Pelton, *ACS Nano* **6**, 472-482 (2012).
58. Y. Ma, X. Li, H. Yu, L. Tong, Y. Gu, Q. Gong, *Opt Lett* **35**, 1160-1162 (2010).

Ambient Stable Tetragonal and Orthorhombic Phases in Penta-Twinned Bipyramidal Au Microcrystals

Summary

Face-centered cubic (fcc) lattice is the only known crystal structure of bulk gold. In the present work, the presence of body-centered tetragonal (bct) and body-centered orthorhombic (bco) phases have been reported in bipyramidal Au microcrystals with penta-twinned tips. These microcrystals have been obtained by thermolysis of $(\text{AuCl}_4)^-$ stabilized with tetraoctylammonium bromide (ToABr) in air at about 220 °C for 30 min. Using a laboratory monochromatic X-ray source, the non-fcc phases could be readily detected. The remarkable occurrence of non-fcc phases of Au grown in the temperature window of 200-250 °C results from the geometrically induced strains in the bipyramids. Having derived first-principles theoretical support for the temperature-dependent stability of non-fcc Au structures under stress, the origin in soft modes is identified. Annealing at high temperatures relieves the stress, thus destabilizing the non-fcc phases.

6.1 Introduction

Cubic lattice structure preferred by noble metals (e.g., Au, Ag, Pd and Pt) is thermodynamically highly stable. Lower-symmetry crystal structures are not known to stabilize relative to the fcc bulk even at high pressures (1). Observing a structural transformation in these metals is therefore fundamentally exciting and can be possibly useful in tuning their otherwise noble behavior. Recent explorations in this direction have focused on nanocrystals as the energy needed for lattice distortion is relatively low when the size is few nanometers (2, 3). The presence of structural defects can further contribute to their stability (4).

Among the possible metastable phases, hexagonal close packed (hcp) structure is quite prevalent in Ag nanoparticles (4-13) under ambient conditions, rather infrequently in Au nanoparticles (14-17) (Table 6.1). Under high pressure, bct and trigonal phases have been identified in Ag and Pd

nanoparticles using high energy X-ray diffraction (XRD) and selective area electron diffraction (SAED) (see Table 6.1) (2, 18, 19). Au nanocrystals are not known to exhibit such phases even under pressure. However, fcc to bct phase transformation has been observed in small regions of Au nanocrystals under transmission electron microscope (TEM) during tensile fracture (20, 21).

Table 6.1 Summary of literature showing the conditions have been adopted to observe non-fcc phases.

S. No	Metal	Shape	Size (μm)	Pressure (GPa)	Observed non-fcc phase(s)	Techniques used	Ref
1	Ag	Prism	0.05 (L)	Ambient	hcp	XRD, TEM	(5)
2	Ag	Prism	0.04 (L)	Ambient	hcp	XRD	(6)
3	Ag	Plate	0.015 (T) x1(L)	Ambient	hcp	XRD, SAED	(7)
4	Ag	Nano rod	0.1(D) x sub-micron	Ambient	hcp	XRD, SAED	(8)
5	Ag	Nano Wire (NW)	0.04 (D)x50 (L)	Ambient	hcp	XRD, SAED	(4)
6	Ag	NW	0.03 (D)x10(L)	Ambient	hcp	XRD, SAED	(9)
7	Ag	NW	0.1 (D)	Ambient	Pure hcp (no fcc)	XRD, TEM	(10)
8	Ag	Rice	0.08 (D) x0.5 (L)	Ambient	hcp	XRD, SAED	(11)
9	Ag	Flower	0.4 (L)	Ambient	hcp	XRD, HRTEM	(12)
10	Au	Sheet	0.002 (T) x0.5 (L)	Ambient	hcp	SAED, XRD	(15-17)
11	Au	-	-	P=248 GPa T= 860 K	hcp	HESXRD	(14)
12	Pd	Cube	~ 0.01 (L)	24.3	bct	DAC, ADXRD	(18)
13	Ag	Plate	0.4 (L)	24	bct	DAC, ADXRD	(19)
14	Ag	Wire	0.085 (D) x20 (L)	Ambient	bct	HESXRD	(22, 23)

15	Ag	Irregular	2-3.5 and 0.05-0.1	33	Trigonal	DAC, ADXRD	(2)
16	Au	Film	0.006 (L) x0.004 (W)	<1	bct	TEM	(20, 21)
17	Au	Bipyramids	~ 1 (D) x3.5 (L)	Ambient	bco, bct	XRD, SAED	Present work

T: Thickness

L: Length

D: Diameter

W: Width

DAC - Diamond anvil cell

ADXRD - Angle dispersive synchrotron XRD

HESXRD - High energy synchrotron XRD

XRD - laboratory XRD source

Among the larger crystallites exhibiting lattice distortion, penta-twinned Ag nanowires are the most prominent (24). Along the length, the nanowire is enclosed with five {100} facets, while its tips are made of five {111} facets hosting twin planes at each boundary (25). It is proposed that the strain associated with twinning can give rise to bco (26) or bct (27) structure. The presence of bct phase in Ag nanowires has been confirmed using high-energy X-ray synchrotron measurements (22, 23). The internal strain induced by penta-twinning seems to grow with the lateral dimension of the nanowire making larger diameters implausible (28).

There have been theoretical investigations as well. An atomistic study of thin Au nanowires has revealed a stress-induced fcc to bct transformation for <100> orientation when external pressure is above 1 GPa (29). While the elastic stability of the bct phase is still debated (30), thermal vibrations can cause fcc <100> orientation to transform to bct (31, 32). Recently, large-scale simulations of five-fold twinned nanowires using modified embedded atom method have shown the occurrence of bco phase induced by large internal stresses concentrated at twin boundaries (30). Further, internal strains developed in nanowires have been shown to get relieved through the generation of dislocations, thus hindering the phase transition (31).

The possibility of inducing non-fcc phase formation is explored in highly twinned Au microcrystals, which in our previous study were obtained in fcc under certain synthetic conditions (33). In this work, the synthetic conditions were optimized to stabilize non-fcc phases. The present study has thus revealed the remarkable presence of significant proportions of bco and bct phases in Au bipyramids at ambient pressures, which could be detected easily using a

laboratory X-ray diffraction equipment. Through first principle theoretical study of temperature-dependent free energies of elastic distortions in the fcc structure, shown the presence of such phases and also present a soft mode-based mechanism that captures the trends in the stability of non-fcc phases of noble metals, in general.

6.2 Scope of the investigation

FCC is the only known crystal structure for bulk/nano Au. It is not surprising that FCC lattice is stable even at few hundreds of GPa pressure. Here, for the first time, the ambient stable body-centered tetragonal (bct) and body-centered orthorhombic (bco) phases have been reported in penta-twinned Au microcrystallites. The non-FCC phases were obtained at milder synthetic conditions and characterized using a laboratory XRD source. At ambient conditions, the non-FCC phases are stable for years; however, converted to FCC on annealing at high temperatures.

6.3 Results and discussion

6.3.1 Stabilizing the non-FCC phases

Penta-twinned Au microcrystals were prepared by subjecting few drops of AuAgToABr solution to different thermolysis temperatures on Si substrates (see Fig. 6.1). XRD patterns of the obtained crystallites showed something striking (Fig. 6.1(a)). While the 150 °C preparation showed sharp and symmetrical peaks that are indexable to bulk FCC with a lattice parameter of 4.081 Å (Au, 4.0804 Å, ICSD No. 180868), the diffraction pattern obtained from microcrystals prepared at 200 °C was not quite the same. Although all intense peaks correspond to bulk FCC structure, the emergence of new peak adjacent to FCC(200) at a slightly higher 2θ value (45.05°) is observed. Amazingly, all FCC peaks are seen considerably asymmetric and broad with the 220 °C preparation, some even exhibiting clear splitting near FCC(200) and (220). The peak shapes encountered here may be compared with those of penta-twinned Ag nanowires obtained using a high resolution synchrotron source (22). It appears that in our study, the Au microcrystals synthesized at 220 °C host significant amounts of non-FCC phases. Similar peak shapes have been observed under high pressures in other noble FCC metals (18).

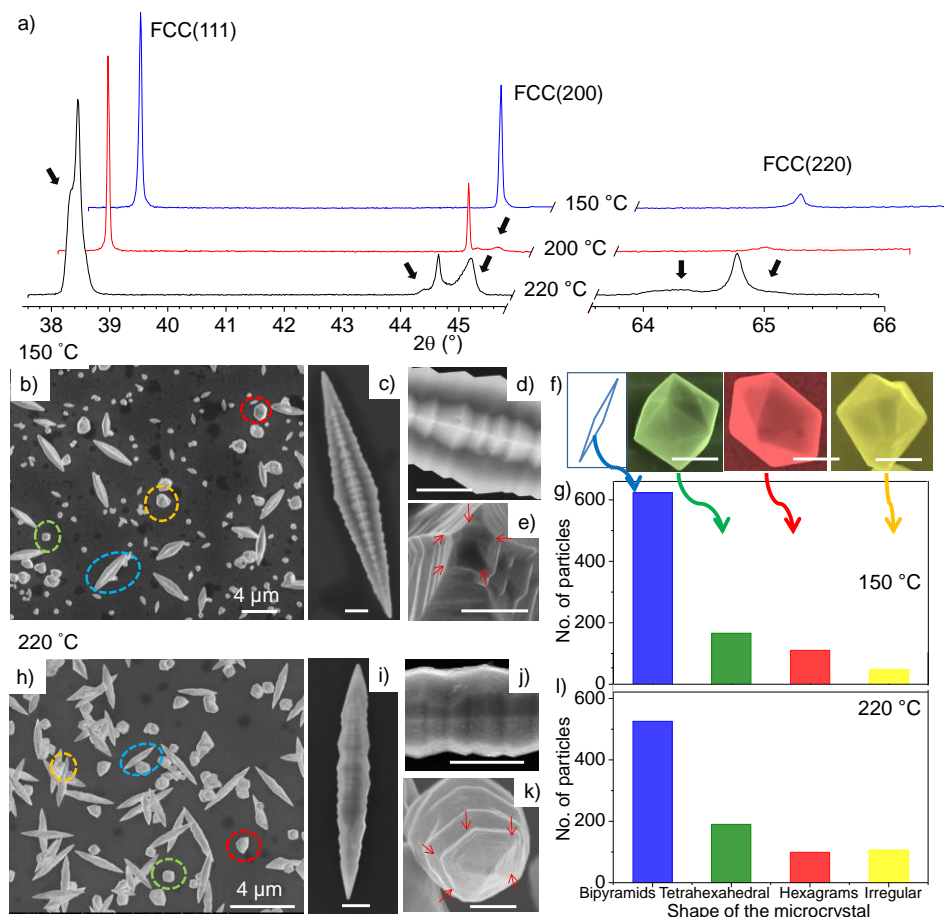


Figure 6.1 (a) XRD patterns obtained from Au microcrystals prepared at 150 °C, 200 °C and 220 °C. Black arrows indicate features arising out of distortions from the FCC cell. SEM images of Au microcrystals, prepared at (b) 150 °C and (h) 220 °C. Other images (c-e and i-k) correspond to different magnifications and orientations of bipyramids. (f) Typical magnified images of non-bipyramidal particles. Histograms of particle counts from (g) 150 °C and (l) 220 °C preparations. Scale bar where not indicated, is 500 nm.

To understand the morphological aspects of Au bipyramids hosting non-FCC phases, scanning electron microscopy (SEM) analysis was carried out (Fig. 6.1). From the SEM images in Fig. 6.1(b) and (h) corresponding to synthetic temperatures of 150 °C and 220 °C respectively, besides bipyramidal shaped particles (shown in blue circles), tetrahexahedral (green), hexagrams (red) and irregular microcrystals (yellow) were also seen. The average lengths of bipyramids prepared at 150 °C and 220 °C are 5.5 and 3.5 μm respectively (see Fig. 6.1(c) and (i)), which are enclosed with penta-twinned tips (Fig. 6.1(e) and (k)). In contrast to 150 °C preparation, the

bipyramids obtained at 220 °C has roughened surface and the edges are slightly rounded (Fig. 6.1(d) and (j)) perhaps due to rapid reduction of AuAgToABr at higher synthetic temperature. The bipyramid grows along the $\langle 110 \rangle$ direction starting from a decahedron by enclosing a highly corrugated region in between the penta-twinned tips (see Fig. 6.2(a)), as detailed out in our previous study (33).

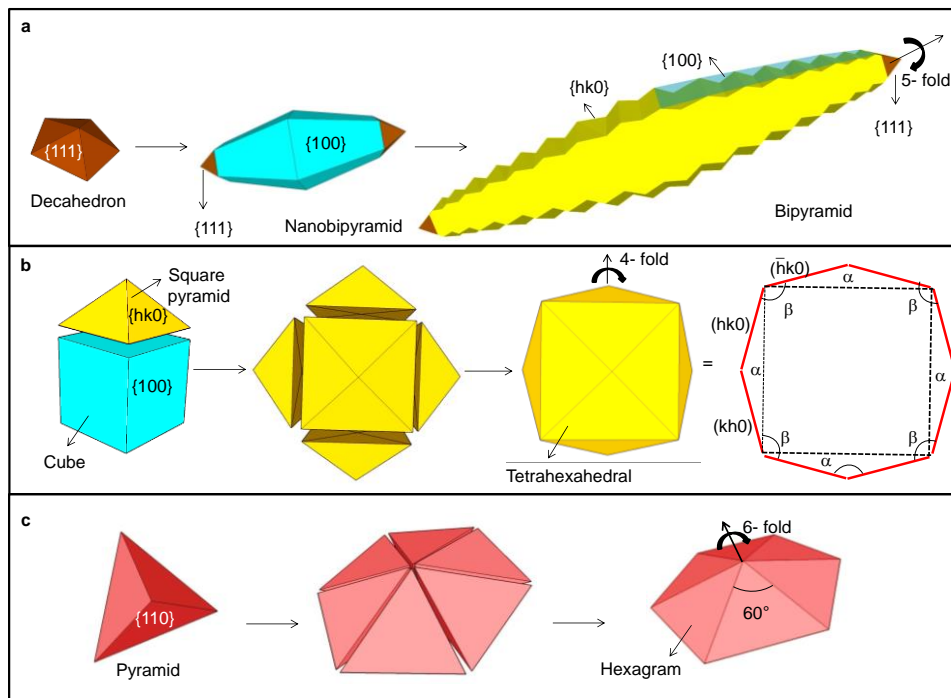


Figure 6.2 Schematic illustrating the formation of (a) bipyramids (b) tetrahexahedral and (c) hexagram. Growth of a decahedron along the $\langle 110 \rangle$ direction produces bipyramids. The $\{100\}$ facets eventually give way to high index facets resulting in a corrugated surface (Fig. 6.2(a)). Tetrahexahedral shape is considered as an assembly of a cube and six square pyramids. Each $\{100\}$ facet (cyan) of a cube capped with a square pyramid enclosed with $\{hk0\}$ type-high index facets (yellow).

Assembly of pyramids with $\{110\}$ (red) produces a hexagram. As schematically illustrated, the tetrahexahedral geometry is derived from a cube where each $\{100\}$ facet is capped with a square pyramid of $\{hk0\}$ facets (Fig. 6.2(b)), while hexagram can be considered as an assembly of six pyramids, sharing a common $\{110\}$ facet (see Fig. 6.2(c)). Both these structures are well known and are unstrained FCC structures (34, 35). Tetrahexahedral and hexagram crystallites possess 4 and 6-fold symmetries respectively. Hence, these crystallites are free of geometry induced,

unlike penta-twinned crystallites. Based on TEM analysis, the corrugations have been assigned to high index facets, $\{hk0\}$ where h or $k \geq 2$ (see Fig. 6.3).

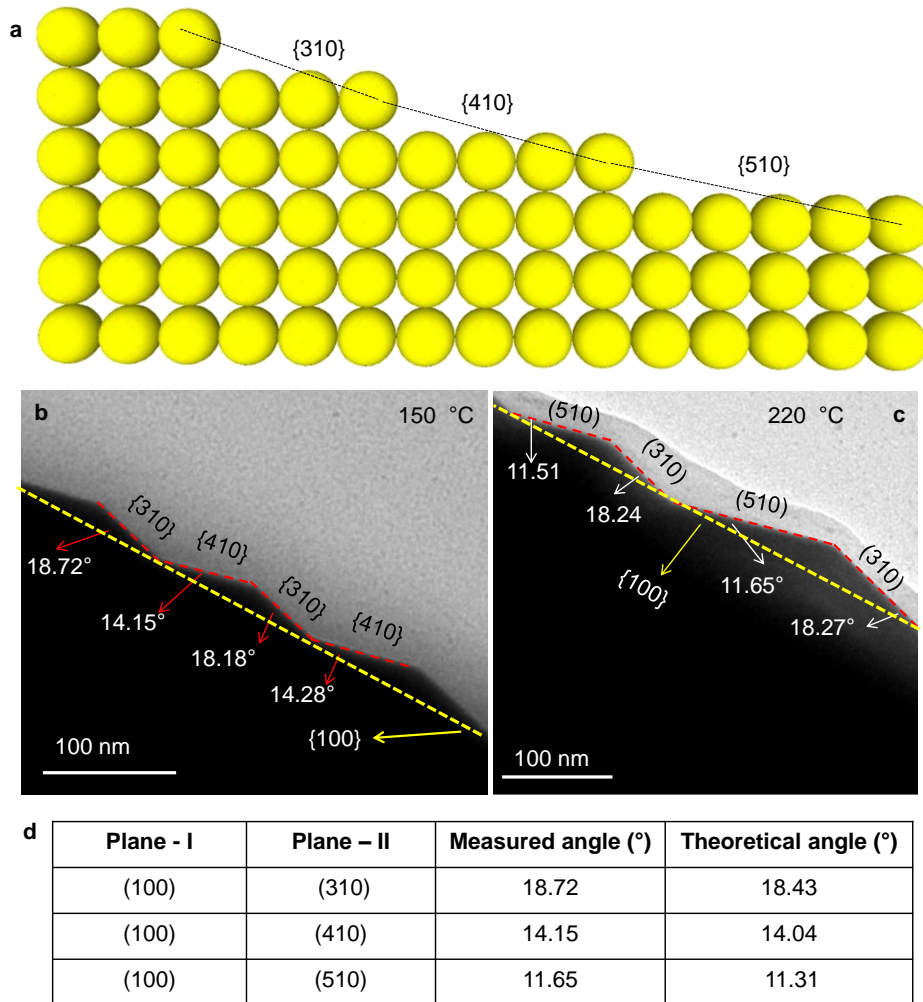


Figure 6.3 (a) Schematic illustrating the high-index facets of $\{hk0\}$ type. TEM images of bipyramids with measured angles, (b) 150 °C and (c) 220 °C preparation. (d) The angular relation of $\{100\}$ facet with $\{310\}$, $\{410\}$ and $\{510\}$ facets. The uncertainty in the measured angles is less than 0.3° .

The details of the assignments are discussed in ref (33).

Facet notation of high index facets is as follows.

$$\{310\} = \text{Au(S)}-[3(100) \times 1(110)]$$

$$\{410\} = \text{Au(S)}-[4(100) \times 1(110)]$$

$$\{510\} = \text{Au(S)}-[5(100) \times 1(110)]$$

Magnified images of the non- bipyramidal particles are shown in Fig. 6.1(f), where the irregular particle (image on the right) seems to exhibit a penta-twinned geometry on one side. From the histograms in Fig. 6.1(g) and (l), it is understood that the major product is bipyramids (~ 65% and ~ 57% respectively for 150 °C and 220 °C thermolysis) with tetrahedral (17% and 20%), hexagram (12% and 10%) and irregular particles (5% and 11%) as minor products. Interestingly, tetrahedral and hexagram crystallites observed in our study are relatively larger (~ 1 μ m) compared to previous studies (see Fig. 6.1(f) and Table 6.2).

Table 6.2. Literature examples of tetrahedral and hexagram shaped Au crystallites.

S. No	Shape	Size (nm)	Reference
1	Tetrahedral	154	(34)
2	Tetrahedral	124 \pm 8	(36)
3	Tetrahedral	150	(37)
4	Tetrahedral	188 \pm 5	(38)
5	Tetrahedral	300	(39)
6	Hexagram	400-800	(40)
7	Hexagonal bipyramids	300	(35)

To ascertain that the occurrence of additional peaks is not because of Ag, compositional purity of the Au microcrystals was carefully examined. From the energy dispersive X-ray spectra (EDS) of the 220 °C preparation, no Ag was detected (Fig. 6.4(a)). This was also the case with 150 °C preparation which is consistent with our previous studies (Fig. 6.4(b) (33)). In support of EDS observation, core-level spectra are dominated by the Au 4f signal while Ag 3d shows only weak signal (Fig. 6.4(c-d)), typical of a monolayer, which is rather expected as it stabilizes the high index facets (41). Further, Au microcrystals hosting non-FCC phases (prepared at 220 °C) were treated with conc. HNO₃ to dissolve away residual Ag on the surface (42). Not surprisingly, no Ag signal was found in XPS (Fig. 6.4(d)), while the microcrystals continued to exist in non-FCC phases (see XRD pattern in Fig. 6.4(f)) after HNO₃ treatment. Hence, it is clear that the additional peaks are due to the strained phases in the Au microcrystals coexisting with the FCC phase.

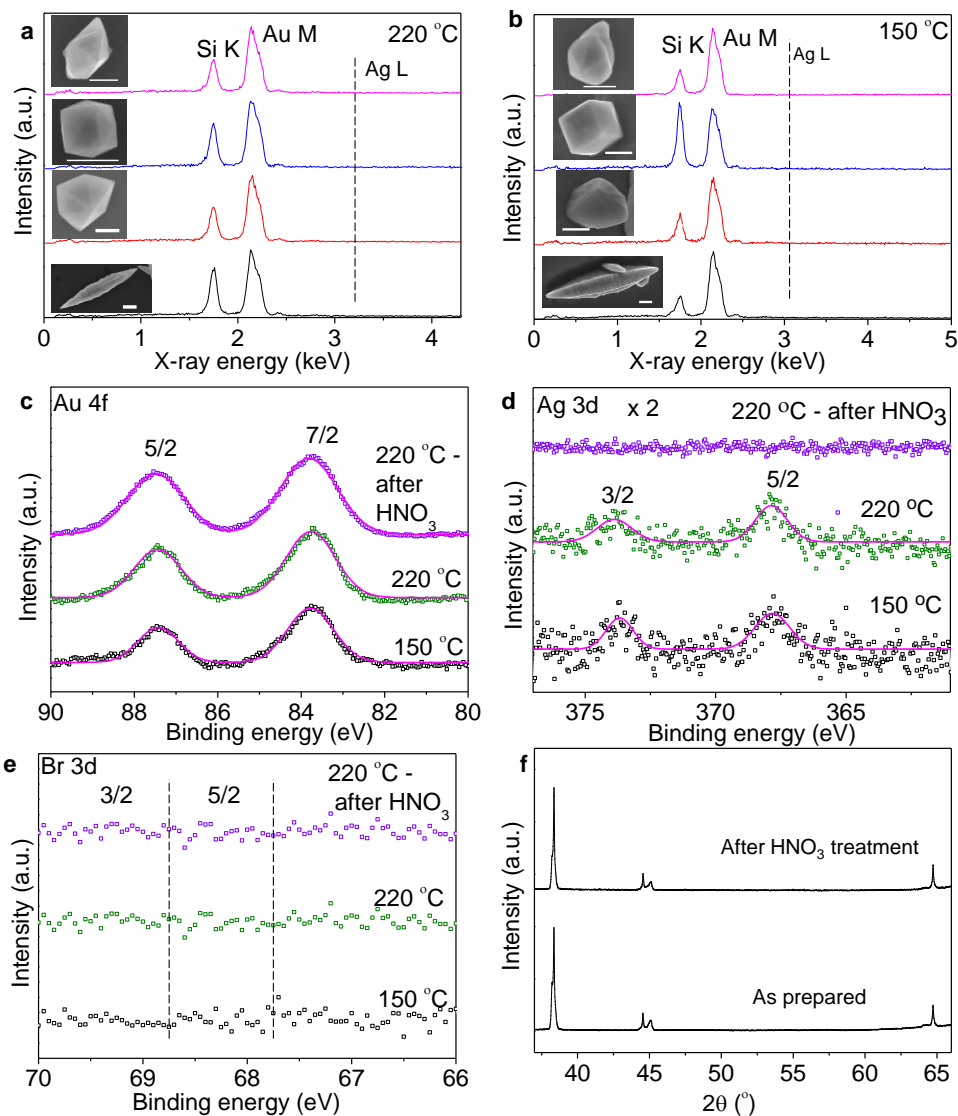


Figure 6.4 (a-b) EDS of individual microcrystals of various shapes from the 220 °C and 150 °C preparations. The corresponding images are shown on the left, from bottom- a bipyramid, a hexagram, a tetrahexahedral microcrystal and an irregular microcrystal (scale bar, 500 nm). Dashed line represents the Ag L position. Core-level spectra in the (c) Au 4f (d) Ag 3d and (e) Br 3d regions for microcrystals prepared at 150 °C, 220 °C and after HNO₃ treatment. For energy calibration, the C1s (284.4 eV) signal was used. (f) XRD patterns of Au microcrystals, as-prepared (220 °C) and after HNO₃ treatment. It may be noted that SEM imaging with high energy e-beam did not cause any noticeable changes in the XRD pattern.

In our previous study (33), it is discussed in detail how Ag(I) assists the bipyramidal morphology while not being part of the structure. Residual Ag from precursor which is surface bound, could be easily washed away not influencing the morphology and the non-FCC phases (see Fig. 6.4). Further, the bipyramidal morphology hosting non-FCC phases is found to be independent of the nature of the substrate employed (see Fig. 6.5). However, the nature of the halide ion seems to matter (see Fig. 6.6).

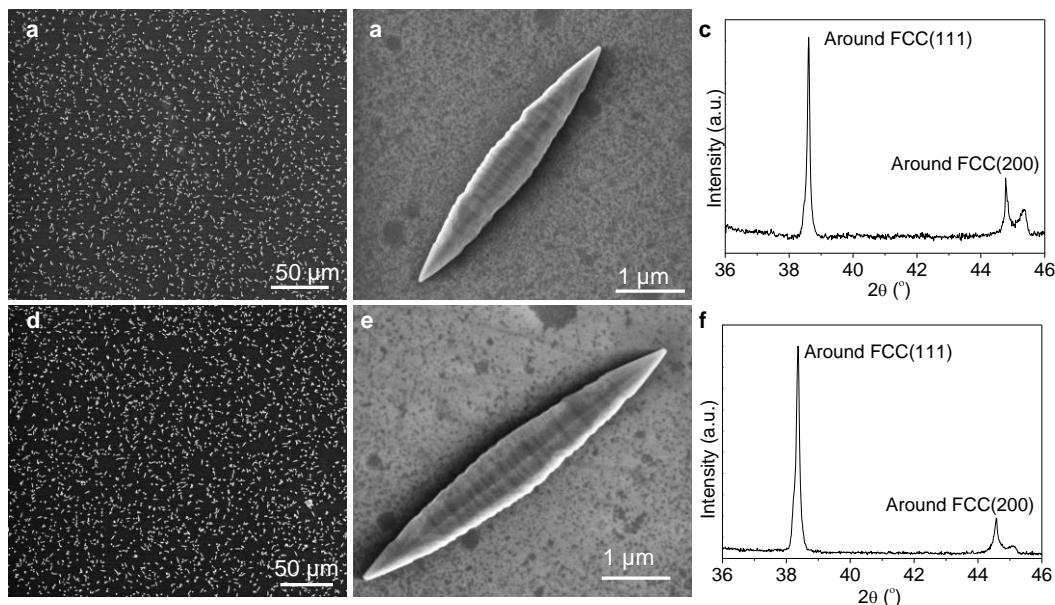


Figure. 6.5 SEM images and XRD patterns collected from Au microcrystals prepared on quartz (a-c) and glass (d-f).

Further, to eliminate possible substrate effects, Au microcrystals were prepared on glass and quartz substrates instead of Si. XRD patterns and shape of Au bipyramids prepared on Si (Fig. 6.1(a)), glass and quartz are found to be quite similar (see Fig. 6.5).

Attempts to stabilize the non-FCC phases using other halide quaternary salts such as ToACl and ToAI have not meet with success under the given synthetic conditions (see Fig. 6.6). Halide anions play an important role in controlling the shape of the Au crystals. It is found that from ToACl (Fig. 6.6), elongated bipyramids (~ 8 μm, javelin shaped Au microcrystals) with relative proportion of ~ 18%, are obtained in comparison to smaller (~ 3 μm) bipyramids (~ 65%) observed with ToABr. These observations are consistent with the recently report where the conversion of bipyramids to javelin shape was obtained by changing the halide anion from Br⁻ to Cl⁻ (43). The lower affinity of Cl⁻ towards Au surface and its high reactivity, allows the Au

bipyramids to grow longer. Yet the bipyramid count is poor due to the non-specific adsorption of Cl^- on Au surface (44).

With ToAI, longer Au bipyramids ($\sim 20 \mu\text{m}$) are obtained but in less proportion ($\sim 9\%$). The longer size of the Au bipyramids is due to the oxidation of Au surface by I_3^- obtained from the combination of I^- and I_2 . Due to the preferential adsorption of I^- , majority of the obtained particles are covered with $\{111\}$ facets (45). This argument is supported by the predominate $\{111\}$ peak in the XRD pattern of Au particles prepared from AuAgToABI. Under the synthetic conditions employed, the Au microcrystals obtained from AuAgToACl and AuAgToAI crystallize in FCC structure unlike those obtained from AuAgToABr, where significant proportion of non-FCC exists. This may be attributed to the dissociation rate of Au-halides; the dissociation energy order is $\text{AuCl} > \text{AuBr} < \text{AuI}$ (46).

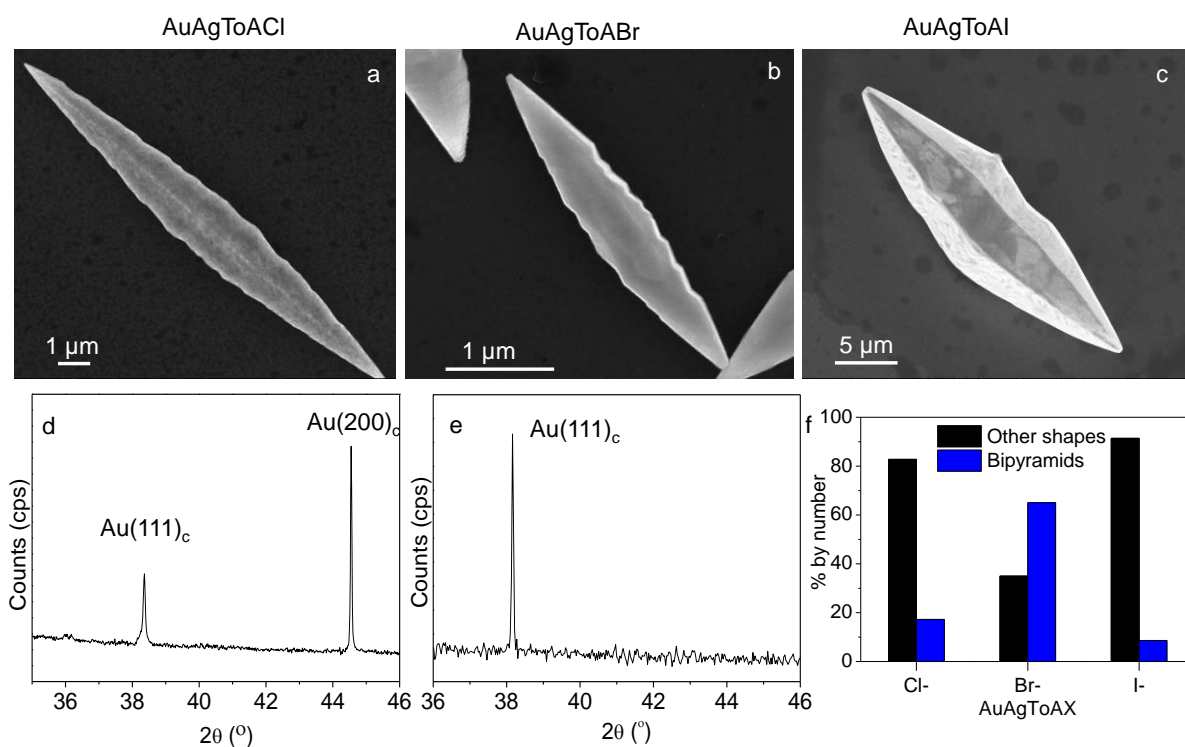


Figure 6.6 SEM images of Au bipyramids obtained from (a) AuAgToABr, (b) AuAgToACl and (c) AuAgToAI, other conditions being the same. (d) XRD of Au microcrystal obtained from (d) AuAgToACl and (e) AuAgToAI respectively. (f) Histogram of particle counts obtained from various halides.

6.3.2 TEM characterization

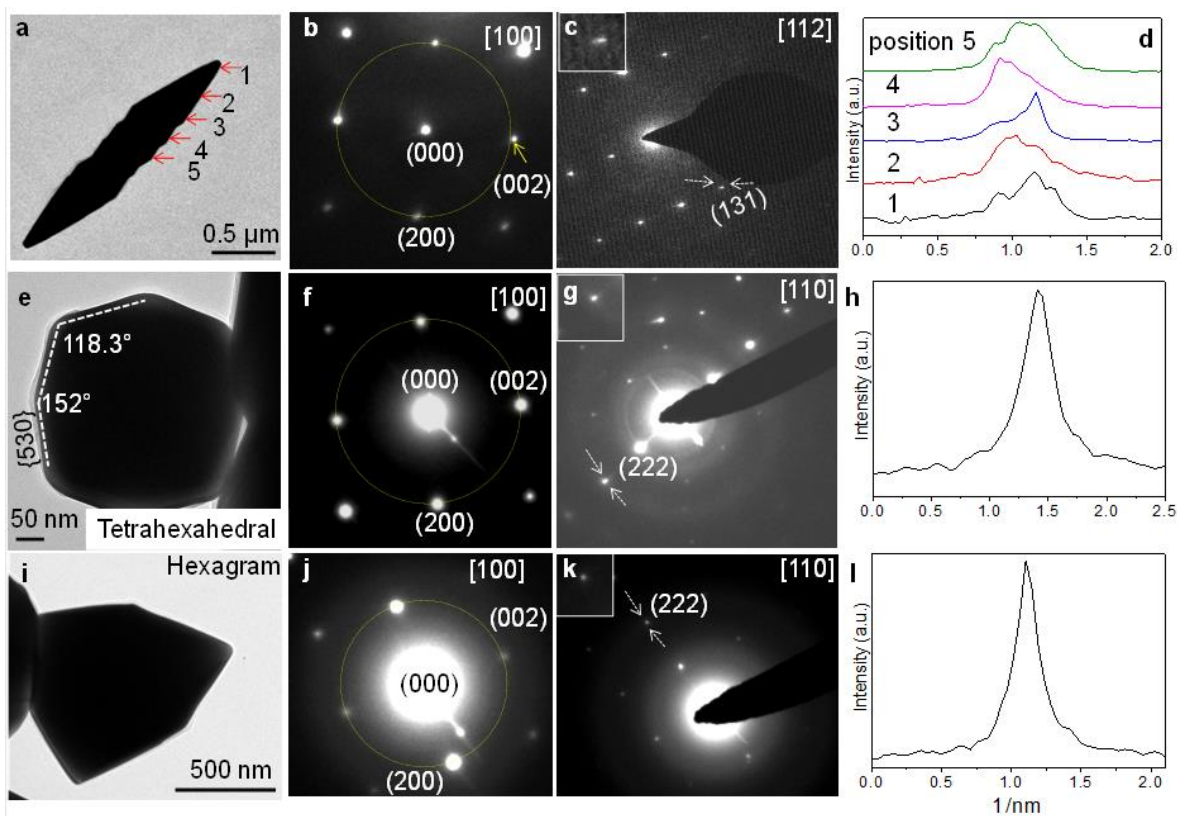


Figure 6.7 (a-c) TEM image of Au bipyramid and the ED patterns collected along the [100] and [112] directions. (d) Intensity profiles drawn along {113} spots from the regions 1 to 5 are shown in (d). (e, i) TEM images of Au tetrahedral and hexagram microcrystals, and their respective ED patterns collected along the [100] (f, j) and [110] (g, k) directions. (h) The intensity profile of (222) spot shown in (g) and, (l) of that shown in (k). The tetrahedral microcrystal shown in (e) is enclosed with the FCC {530} facets.

SAED was performed on different microcrystals from the 220 °C preparation (Fig. 6.7). Although the ED pattern obtained along the [100] direction (Fig. 6.7(b)) of a bipyramid (Fig. 6.7(a)) exhibits a nearly square symmetry, the *d*-spacings for the (002) and (200) reflections differ by ~ 3% (2.08 and 2.01 Å respectively), in contrast to the equal *d*-spacings observed from the 150 °C preparation (Fig. 6.8).

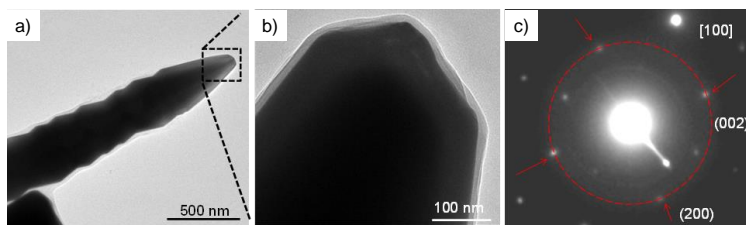


Figure 6.8 (a, b) TEM images of tip of Au bipyramid at different magnifications. (c) ED pattern collected from the tip oriented along the [100] zone axis.

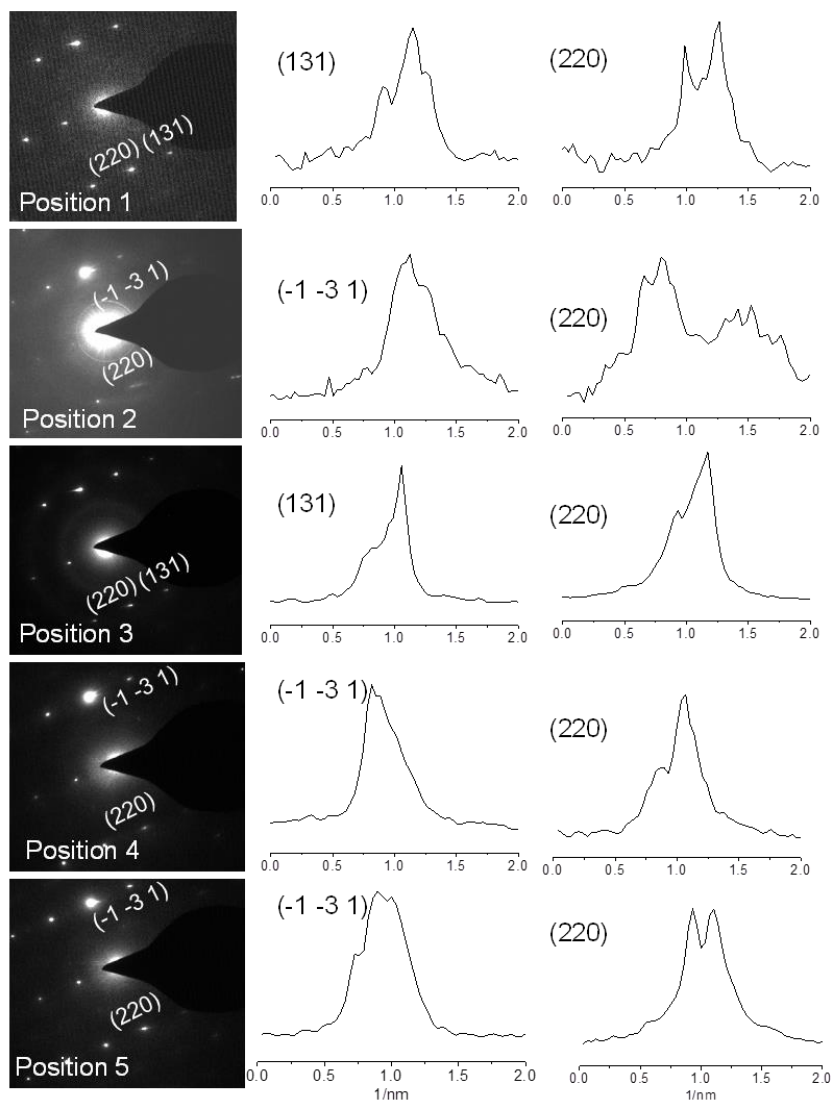


Figure 6.9 SAED patterns collected at an interval of ~ 200 nm along the [112] zone axis from tip (position 1) to center (position 5) of a Au bipyramid. Intensity profiles drawn along the family of {131} and {220} spots.

The observed difference in the former case is similar to the reported value in Ag nanowires (22). Such deviations from symmetry indicate the presence of non-FCC phases in the bipyramid. ED patterns along the $[112]$ axis have been collected between the tip and the center at an interval of 200 nm. In all the cases, it is observed that the $\{113\}$ and $\{220\}$ spots exhibited splitting in the intensity profiles (Fig. 6.7(d) and Fig. 6.9). It implies that the non-FCC phases are distributed all over, from tip to the center of the Au bipyramid. In tetrahedral (Fig. 6.7(e-h)) and hexagram (Fig. 6.7(i-l)) particles, neither non-uniform d -spacings nor non-uniform spots are observed. The surface induced strain, if any, should also be minimal in these microcrystals unlike in nanocrystals of similar shapes (47).

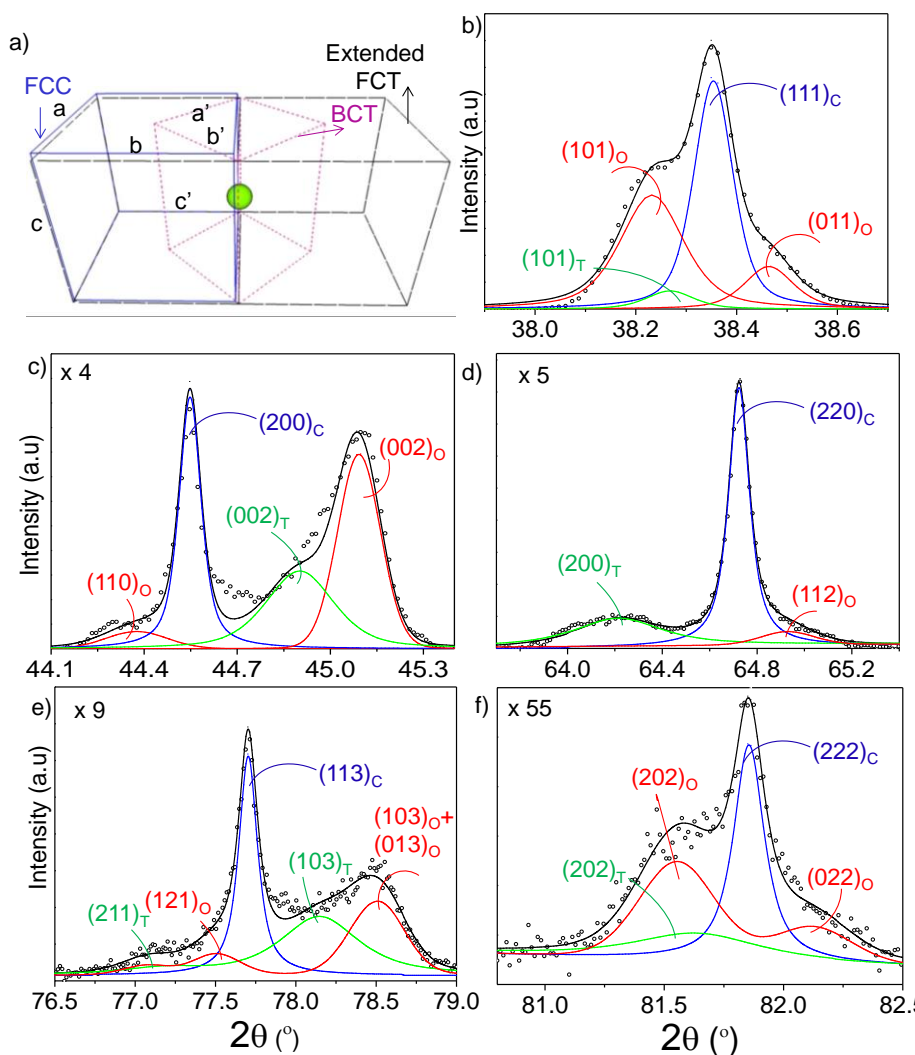


Figure 6.10 (a) Schematic illustrating FCC unit cell along with extended FCT and BCT unit cells. (b-f) Profile fitting of XRD peaks. The experimental data is in black circles. Blue, red and

green fitted curves represent cubic (marked as C), orthorhombic (O) and tetragonal (T) peaks respectively with their sum shown as black curve.

Having clues for the presence of non-FCC phase(s), attempted to fit the XRD patterns with combinations of crystal structures, iteratively using the WinPLOTR software. We embarked on three phase combinations among which, FCC + tetragonal (I4/mmm) + orthorhombic (Immm), produced the best fit with χ^2 of 3.16 (Fig. 6.10). XRD peak analysis revealed the presence of non-FCC phases with compression along c -axis and expansion along a and b axes. Fig. 6.10(a) shows the schematic of FCC, derived FCT along with BCT unit cells. Note that for BCT, $a' = b' = \frac{a}{\sqrt{2}}$ and $c' = c$, where a , b , and c are lattice parameters of FCT. For BCT form of FCC, $\frac{c'}{a'} = \sqrt{2}$. Experimentally obtained lattice parameters of the BCT are, $a' = b' = 2.9062 \text{ \AA}$ and $c' = 4.0503 \text{ \AA}$ with $\frac{c'}{a'} = 1.394$ (deviation of -1.44% from the FCC structure). Unequal strains along a , b and c axes result in a BCO structure. The calculated lattice parameters of BCO are $a' = 2.9165$, $b' = 2.8907$ and $c' = 4.0337 \text{ \AA}$ with $\frac{c'}{a'} = 1.383$ and $\frac{c'}{b'} = 1.395$ which indicate that the strain along the a -axis is higher than that along b (48). Finally, in terms of cell volume, BCT volume is 0.62% higher while that of BCO is higher by only 0.03% with reference to the unstrained BCT ($\frac{c'}{a'} = \sqrt{2}$) (see Table 6.3).

Table 6.3 Lattice parameters of various crystal structures and the corresponding c/a ratio.

	BCT form of FCC	c/a	BCT	c/a	BCO	$c/a, c/b$
Cell parameters (\AA)	$a=2.8862$ $b=2.8862$ $c=4.0811$	1.414	$a=2.9062$ $b=2.9062$ $c=4.0503$	1.3936	$a=2.9165$ $b=2.8907$ $c=4.0337$	1.3830, 1.3954
Volume (\AA^3)	33.99		34.2088		34.007	

As shown in Fig. 6.10(b), the asymmetrically broadened profile of the $(111)_C$ peak is fitted with $(101)_T$, $(101)_O$ and $(011)_O$ peaks. The non-FCC peaks are broader (particularly from BCT) due to the strain prevalent in these unit cells. This is more evident in the $(200)_C$ region where the non-FCC contribution is seen well separated, which has been fitted to $(002)_T$ and $(002)_O$ peaks (Fig. 6.10(c)). Indeed, the order of the peaks represents increasing compression of the c -axis. For instance, BCT(002) reflection appears in between FCC(002) and BCO(002) such that the order of c is $c_{\text{FCC}} > c_{\text{BCT}} > c_{\text{BCO}}$. Similar trends are seen in the other regions as well (see Fig. 6.10(d-f)).

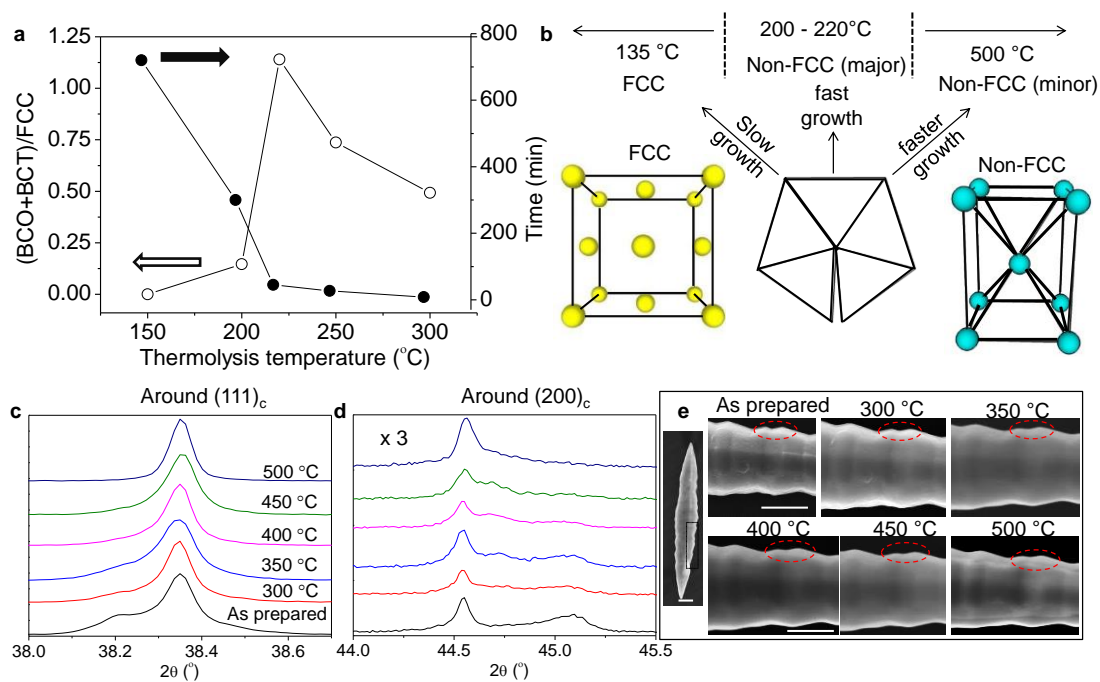


Figure 6.11 (a) Variation in the non-FCC/FCC ratio as derived from XRD peak areas for microcrystals synthesized at various thermolysis temperatures. The time taken to reach a steady wt% in TGA is also shown in each case. (b) Schematic illustrating the occurrence of non-FCC and FCC phases in Au bipyramids at low and high thermolysis temperatures. (c, d) XRD patterns from Au microcrystals annealed at various temperatures. (e) SEM images of a bipyramid on annealing at various temperatures. Scale bar, 500 nm. Annealing was carried out for 1 h in air at each temperature and the measurements were done after cooling to room temperature.

Based on the areas under the XRD peaks, the relative contributions of the different phases as FCC (46.7%), BCT (16.94%) and BCO (36.30%) was estimated. Based on TEM results (Fig. 6.7), it is clear that the non-FCC fraction (BCT+BCO = 53.3%) comes mainly from the Au

bipyramid, while other shaped particles contribute to the FCC fraction. These proportions are sensitive to the synthetic temperature (Fig. 6.11). Only around 220 °C thermolysis, the (BCO+BCT)/FCC ratio is significant; at lower or higher thermolysis temperatures the non-FCC phases formation is not favored (see Fig. 6.1). This trend may be related to the pace of thermolysis at different temperatures. From the isothermal TGA data collected at 150 °C (Fig. 6.12), it is seen that the weight loss was gradual and a steady state was not reached even after 720 min, indicating a slow decomposition of the precursor. With 200 °C TGA, complete decomposition occurred at around ~ 300 min to reach a steady weight of ~ 7% of the initial.

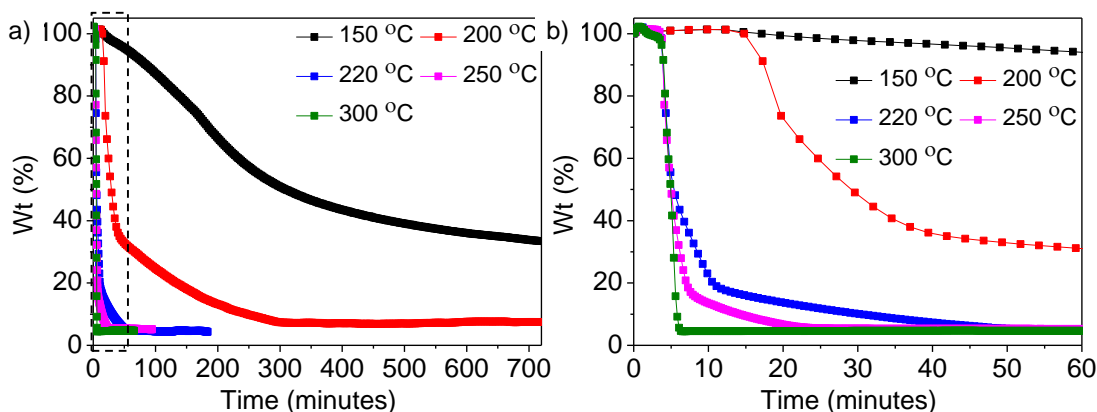


Figure 6.12 (a) TGA plots of the AuAgToABr precursor at various temperatures. (b) Magnified view of the highlighted region in a.

The time taken to reach the steady state decreased rapidly at higher TGA temperatures as shown in Fig. 6.11(a). Interestingly, the change in this trend occurs around ~ 200 °C similar to the change seen with the (BCO+BCT)/FCC ratio. At lower temperatures (< 200 °C), the precursor decomposition and hence bipyramid growth is slow, and the stress developed due to penta-twinning could be accommodated in the FCC lattice itself. At much higher temperatures, though the growth of bipyramid is faster, the internal stresses get annealed due to the abundant thermal energy available. In the intermediate temperature range (~ 200-250 °C) however, the thermal annealing seems incompetent to cope up with the speedy growth leading to preservation of the strain in the form of non-FCC phases (Fig. 6.11(b)) which begin to nucleate even at small sizes (Fig. 6.13). Like in the case of Ag nanowires (22), the non-FCC phases may reside at the core while FCC forms the shell.

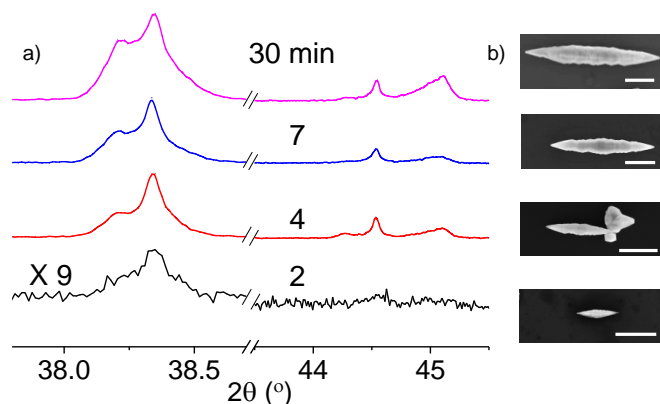


Figure 6.13 XRD patterns obtained from the Au microcrystals prepared at various times of thermolysis, at 220 °C. Typical Au microcrystals from these preparations are shown in the insets. Scale bar, 1 μm .

It appears that during the bipyramid growth, the non-FCC phases begin to nucleate at the very beginning, possibly as a nanodecahedron (22, 33) and the non-FCC peaks are clearly seen just after 4 minutes of thermolysis at 220 °C (Fig. 6.13). It is noteworthy that these interesting non-FCC phases in Au bipyramid are highly stable in ambient conditions (Fig. 6.14). Their stability under harsh chemical environments and e-beam conditions is already established, the latter aspect assumes significance with regard to HCP Au nanosheets (15).

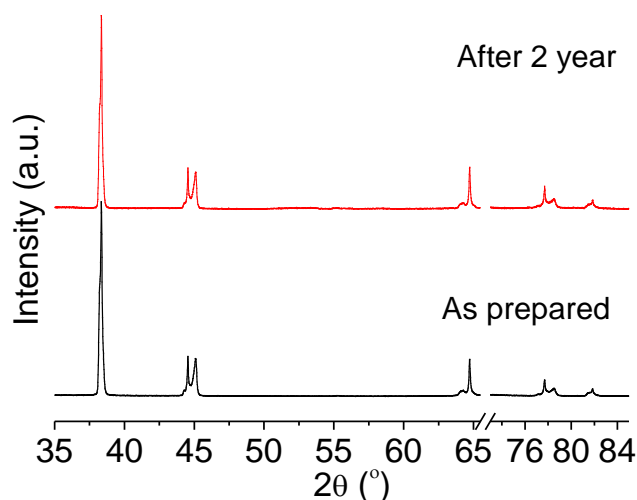


Figure 6.14 XRD patterns obtained from Au microcrystals, as prepared and after two years.

However, the strain in the bipyramids could be released by annealing at elevated temperatures (see Fig. 6.11(c, d)) with little change in morphology (Fig. 6.11(e)). The XRD pattern obtained at 500 °C is indexable entirely to FCC. The conversion to FCC results in the reduction of volume of

non-FCC unit cells, which in turn reduced the length and width of the bipyramid by 6.12% and 4.54% respectively (Fig. 6.15).

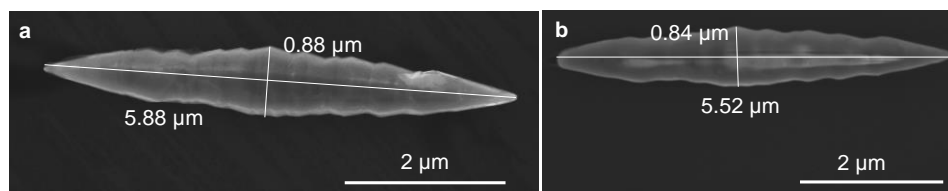


Figure 6.15 (a-b) SEM images of a bipyramidal microcrystal before and after annealing at 500 °C for 1hr.

Further, the free energy of non-fcc phases has been calculated using first-principles calculations. In this regard, the non-fcc phases are treated as strained forms of its fcc structure. Density functional theory (DFT) calculations show that the free energy of strained systems increases with temperature (48).

6.4 Conclusion

The present study involves thermalizing the precursor (AuAgToABr) in air to a range of thermolysis temperatures (150 - 220 °C). This yields distinctly shaped Au microcrystals namely bipyramids, tetrahedral and hexagrams. The bipyramids are typically $\sim 3.5 \mu\text{m}$ long with tip diameter of $\sim 120 \text{ nm}$ and are faceted with a high index corrugated surface, with penta-twinned $\{111\}$ facets at the tips. This five-fold symmetry along the length introduces internal strains, which are essentially absent in other shapes. Interestingly, the samples obtained above 200 °C (particularly at 220 °C) reveals the presence of non-FCC phases (BCT (I4/mmm) and BCO (Immm)) in significantly high proportions ($\sim 55\%$) at ambient pressure, and can be easily detected using a laboratory monochromatic X-ray source. These non-FCC phases have been hitherto known to occur in nanowires or nanosheets of noble metals, only at high pressures. The kinetics of thermolysis seems to be critical in the existence of the non-FCC phases in Au bipyramids. At lower temperatures ($< 200 \text{ }^\circ\text{C}$), the decomposition of the precursor being slow yields only the FCC phase in the bipyramids, while between 200-250 °C the reaction kinetics locks the strains to form the non-FCC phases. Annealing at higher temperatures (above 300 °C) unlocks the strains and results in nearly FCC phase at 500 °C. Theoretical calculations elucidate temperature-dependence of the free energies of certain non-FCC (BCT and BCO) structures.

References

1. M. I. McMahon, R. J. Nelmes, *Chem Soc Rev* **35**, 943 (2006).
2. Q. Guo, Y. Zhao, Z. Wang, S. E. Skrabalak, Z. Lin, Y. Xia, *J Phys Chem C* **112**, 20135 (2008).
3. Au cluster compounds are known to exhibit non-FCC metal clusters bonded with ligands. However they are different class of materials. See for example, H. Qian, W. T. Eckenhoff, Y. Zhu, T. Pintauer, R. Jin, *J Am Chem Soc* **132**, 8280 (2010).
4. B. Wang, G. T. Fei, Y. Zhou, B. Wu, X. Zhu, L. Zhang, *Cryst Growth Des* **8**, 3073 (2008).
5. D. Aherne, D. M. Ledwith, M. Gara, J. M. Kelly, *Adv Funct Mater* **18**, 2005 (2008).
6. V. Bansal, V. Li, A. P. O'Mullane, S. K. Bhargava, *CrystEngComm* **12**, 4280 (2010).
7. D. V. Zhelev, T. S. Zheleva, *J Appl Phys* **115**, 044309 (2014).
8. T. Liu, D. Li, D. Yang, M. Jiang, *Chem Commun* **47**, 5169 (2011).
9. X. Liu, J. Luo, J. Zhu, *Nano Lett* **6**, 408 (2006).
10. A. Singh, A. Ghosh, *J Phys Chem C* **112**, 3460 (2008).
11. H. Liang, H. Yang, W. Wang, J. Li, H. Xu, *J Am Chem Soc* **131**, 6068 (2009).
12. T. Liu, D. Li, D. Yang, M. Jiang, *Langmuir* **27**, 6211 (2011).
13. I. Chakraborty, D. Carvalho, S. Shirodkar, N., S. Lahiri, S. Bhattacharyya, R. Banerjee, U. Waghmare, P. Ayyub, *J Phys: Condens Matter* **23**, 325401 (2011).
14. L. Dubrovinsky, N. Dubrovinskaia, W. A. Crichton, A. S. Mikhaylushkin, S. I. Simak, I. A. Abrikosov, and et al, *Phys Rev Lett* **98**, 045503 (2007).
15. X. Huang, S. Li, Y. Huang, S. Wu, X. Zhou, S. Li, C. L. Gan, F. Boey, C. A. Mirkin, H. Zhang, *Nat Commun* **2**, 292 (2011).
16. X. Huang, S. Li, S. Wu, Y. Huang, F. Boey, C. L. Gan, H. Zhang, *Adv Mater* **24**, 979 (2012).
17. X. Huang, H. Li, S. Li, S. Wu, F. Boey, J. Ma, H. Zhang, *Angew Chem Int Ed* **50**, 12245 (2011).
18. Q. Guo, Y. Zhao, W. L. Mao, Z. Wang, Y. Xiong, Y. Xia, *Nano Lett* **8**, 972 (2008).
19. Y. Sun, W. Yang, Y. Ren, L. Wang, C. Lei, *Small* **7**, 606 (2011).
20. H. Zheng, A. Cao, C. R. Weinberger, J. Y. Huang, K. Du, J. Wang, Y. Ma, Y. Xia, S. X. Mao, *Nat Commun* **1**, 144 (2010).
21. A. Nie, H. Wang, *Mater Lett* **65**, 3380 (2011).

22. Y. Sun, Y. Ren, Y. Liu, J. Wen, J. S. Okasinski, D. J. Miller, *Nat Commun* **3**, 971 (2012).
23. Z. Li, J. S. Okasinski, J. D. Almer, Y. Ren, X. Zuo, Y. Sun, *Nanoscale* **6**, 365 (2014).
24. Y. Sun, B. Mayers, T. Herricks, Y. Xia, *Nano Lett* **3**, 955 (2003).
25. Y. Sun, *Nanoscale* **2**, 1626 (2010).
26. B. G. Bagley, *Nature* **208**, 674 (1965).
27. C. Y. Yang, *J Cryst Growth* **47**, 274 (1979).
28. W. Zhang, Y. Liu, R. Cao, Z. Li, Y. Zhang, Y. Tang, K. Fan, *J Am Chem Soc* **130**, 15581 (2008).
29. M. Durandurdu, *Phys Rev B* **76**, 024102 (2007).
30. Y. Zhou, K. A. Fichthorn, *J Phys Chem C* **118**, 18746 (2014).
31. J. Diao, K. Gall, M. L. Dunn, *Nat Mater* **2**, 656 (2003).
32. J. Diao, K. Gall, M. L. Dunn, *Phys Rev B* **70**, 075413 (2004).
33. G. Mettela, R. Boya, D. Singh, G. V. P. Kumar, G. U. Kulkarni, *Sci Rep* **3**, 1793 (2013).
34. J. Li, L. Wang, L. Liu, L. Guo, X. Han, Z. Zhang, *Chem Commun* **46**, 5109 (2010).
35. M. L. Personick, M. R. Langille, J. Wu, C. A. Mirkin, *J Am Chem Soc* **135**, 3800 (2013).
36. C. Zhengbo, G. Junxia, L. Jing, G. Lin, *Nanotechnology* **24**, 295501 (2013).
37. X. Lang, T. You, P. Yin, E. Tan, Y. Zhang, Y. Huang, H. Zhu, B. Ren, L. Guo, *Phys Chem Chem Phys* **15**, 19337 (2013).
38. T. Ming, W. Feng, Q. Tang, F. Wang, L. Sun, J. Wang, C. Yan, *J Am Chem Soc* **131**, 16350 (2009).
39. D. Y. Kim, S. H. Im, O. O. Park, *Cryst Growth Des* **10**, 3321 (2010).
40. Q. Jiang, Z. Jiang, L. Zhang, H. Lin, N. Yang, H. Li, D. Liu, Z. Xie, Z. Tian, *Nano Res* **4**, 612 (2011).
41. Liu, P. Guyot-Sionnest, *J Phys Chem B* **109**, 22192 (2005).
42. L. L. Martínez, M. Segarra, M. Fernández, F. Espiell, *Metall Trans B* **24**, 827 (1993).
43. D. Chateau, A. Liotta, F. Vadcard, J. R. G. Navarro, F. Chaput, J. Lerme, F. Lerouge, S. Parola, *Nanoscale* **7**, 1934-1943 (2015).
44. O. M. Magnussen, *Chem Rev* **102**, 679 (2002).
45. J. S. DuChene, W. Niu, J. M. Abendroth, Q. Sun, W. Zhao, F. Huo, W. D. Wei, *Chem Mater* **25**, 1392 (2012).

46. J. R. Brown, P. Schwerdtfeger, D. Schröder, H. Schwarz, *J Am Soc Mass Spectrom.* **13**, 485 (2002).
47. I. Robinson, R. Harder, *Nat Mater* **8**, 291 (2009).
48. The theoretical calculations are borne out of collobaration, for details see *J Am Chem Soc* **137**, 3024-3030 (2015).

Nanocrystalline Ag microflowers as versatile SERS platform

Summary

Herein, the synthesis of Ag microflowers for use as manipulable and reusable substrates in surface enhanced Raman spectroscopy (SERS), is demonstrated, working with ultra-low volumes of an analyte. Flower-like AgBr crystallites with a growth direction of $\langle 110 \rangle$ were first obtained by thermolysing a complex obtained by the stabilization of $(\text{AgCl}_2)^-$ anion with tetraoctylammonium bromide (ToABr). NaBH_4 reduction leads to the formation of porous Ag microflowers (50-100 μm) with interconnected nanoparticles. The coupling of the nanoparticles in the microflower results in broadband extinction from visible to IR wavelengths, facilitating SERS using both red and green wavelengths. Using thiophenol as test analyte, uniform SERS enhancement factors in the range of $10^6 - 10^8$ have been achieved from different parts of the microflower. The microflowers have been used for labeled and non-labeled detection of both single and double stranded DNA and using simple manipulation techniques, SERS data has been collected from ultra-low volumes of analyte solution (~ 0.34 nL). The reusability of the substrate for SERS over multiple cycles involving fast and efficient wet chemical cleaning procedure is also demonstrated. Finally, by placing the microflower in a microfluidic device, chemical reactions have been examined in-situ.

7.1 Introduction

Noble metal nanostructures hosting high mobility electrons in confinement give rise to surface plasmon-polaritons which can generate intense electromagnetic fields in the vicinity (1). The extraordinary ability of surface enhanced Raman spectroscopy (SERS) comes from this electromagnetic enhancement when the analyte molecule is in the neighborhood of a plasmonic nanostructure (2). Coupled with chemical enhancement and other surface effects, high enhancement factor, G of the order of 10^6 - 10^8 can be reached (2, 3). Thus, SERS has come a long way in the past few decades as an alternative to

fluorescence for ultrasensitive detection of trace amount of molecules (3, 4). Extremely high enhancement factors ($G > 10^{13}$) can also be achieved by subjecting a few molecules inside nanoparticle junctions to intense electric field intensity, known as hotspots (5); but these are difficult to engineer. Although SERS has been extensively researched in recent years, it still faces significant challenges to become a commercially viable analytical tool. For instance, the presence of hot spots on a SERS substrate can be detrimental to its performance (5), as uniformity of G factor across the substrate cannot be ensured (6). A plasmonic structure with uniform and reproducible enhancement across the substrate area is an essential requirement (7). Secondly, the technique should minimize the volume of the analyte used and localize it to the probe volume (8), as biologically relevant analytes are often retrieved only in trace amounts. Further, designing broadband extinction substrates will make the use of different laser wavelengths possible (9). Importantly, reusability of the substrates would make the analytical process resource intensive and cost effective. Finally, the substrate should provide the comfort of easy handling at least at μm level without compromising on the nanostructure required for the plasmonic activity. These issues have been addressed in this study and have come up with a competent SERS substrate.

The SERS G factor can be hiked by fine-tuning the substrate morphology in terms of the size (10), shape (11) and interconnectivity of the nanostructures involved (6). Typically, Au and Ag metal nanostructures are used due to their high plasmonic activity in the visible to near infra-red regions (12). Significant advances have been made in the recent past, to chemically synthesize nanoparticles of various shapes- rods (13), hexagons (14), cups (15), stars (16), dendrites (17), tapered structures (18), granular films (19), flowers (20), urchin (21) and other 3D structures (22) and other geometric shapes (23), and realize SERS from them. Particles with sharp edges and tips with extinction band in $\sim 500\text{-}1000$ nm range are preferred (23). Besides individual nanoparticles, there have been studies on coupled nanoparticles with defined interconnectivity (24). However, these structures are limited in extension for analyte dosing and easy manipulation under a Raman setup. Active regions extending to few microns matching the size of the laser beam have been produced by template assisted synthesis (25) or by physical methods involving patterning

(26). However, these methods make use of sophisticated lithography techniques or involve multi-step chemical processes. What is desirable is a simple fabrication process for easily manipulable nanostructured SERS substrates.

7.2 Scope of the investigation

Fabrication of a manipulable and reusable SERS substrate that exhibits wavelength independent SERS activity is still a major challenge. In addition, providing a simple solution based route for recycling of SERS substrate is another important aspect related to applications. In this chapter, a two-step chemical process is reported for flower-like microstructures (~ 100 μm) made of interconnected Ag nanoparticles. G-factors have been estimated for various analytes at ultra-low volumes and concentrations for 532 and 632.8 nm. The SERS substrates have been tested over 10 cycles by repeatedly treating them with HCl and NH_3 . The possibility of using the microflowers as microfluidic platforms is also demonstrated.

7.3 Experimental Section

7.3.1 Materials

Silver nitrate (AgNO_3), tetraoctylammonium bromide (ToABr), Sodium chloride (NaCl), HCl, IPA, H_2O_2 toluene were obtained from S. D fine and o-Phenylenediamine (OPD) from Sigma-Aldrich. Water used in this study was double distilled and deionized. Si and glass substrates were cleaned with water, IPA, toluene and dried under N_2 gas. Single stranded oligonucleotides; oligoA (5'CGTGGCCTGGGCGGGACTGGGTCCGTCTGTTGTGTGTGACTCTGGTAACT; G%, 39), (5'cy5AGTTACCAGAGTCACACACAACAGACGG), oligo B (5'CTAAGTGAAGATCCTTGCATAAAGTC; G%, 19), oligo C (5'CCATTAACATTTGGATGGTGCTGTCCCTGTTGTGGACTCTGGTAACT; G%, 24.4) were obtained from Bio-serve Biotechnologies India Pvt. Ltd. and salmon sperm DNA were obtained from Sigma-Aldrich.

7.3.2 AgToABr complex preparation

A 1 mL of AgNO_3 solution (25 mM) was added to 1 mL of saturated NaCl solution under stirring to give rise to a white color colloidal dispersion of AgCl. To this 2 mL of ToABr

(50 mM in toluene) was added and stirring was continued until AgCl got phase transferred to the organic phase. The AgToABr complex was separated from the organic phase for further use and characterization. The decomposition of AgToABr starts at ~ 165 °C and completes at 230 °C.

7.3.3 Preparation of AgBr microflowers and reduction

A 100 μL of AgToABr was drop coated on Si substrate and thermalized at 250 °C on a hot plate for 1h in air. The sample was washed with toluene to remove the unreacted precursor and the AgBr microflowers obtained were reduced to Ag by dipping in NaBH_4 solution (17 mM).

7.3.4 Manipulation of single microflower

A carbon fiber (~ 9 μm diameter) was used for manipulating the microflowers individual microflowers. Two approaches were followed. In one case, a single microflower was lifted using the carbon fiber and transferred to a desired position after soaking it in a 200 nL of 1 μM R6G solution in DMSO for few seconds. In the second approach, the bare tip of a carbon fiber was dipped in a 200 nL of 1 μM R6G solution in DMSO. The microdroplets sticking to the fiber were transferred to the single microflower by gently touching the latter under a microscope. In both cases the microflowers were washed with ethanol and dried before collecting SERS spectra. A 180° backscattering Raman geometry was used with a source of 532 nm to collect Raman spectra. The details of the instrumentation can be found elsewhere (27). The instrument resolution is 2 cm^{-1} .

7.3.5 Reusing the Ag microflowers for SERS

After the acquisition of SERS spectra of R6G (1 μM) the microflowers were treated with concentrated HCl for 5 minutes and rinsed thoroughly with water. Subsequently, the substrate was again treated with ammonia solution (30% aqueous solution) for 5 minutes and then rinsed with water. R6G was again adsorbed on to the microflowers for the acquisition of SERS spectra. This procedure was repeated for 10 cycles to demonstrate the reusability of the substrate. In each cycle, volumes of the R6G solution, conc. HCl and

ammonia solution used were 200 nL. Raman spectra were collected after the HCl and ammonia solution treatment cycles to monitor the removal of R6G molecules.

7.3.6 Fabrication of a microchannels mold for immunoassay test

A mould made of polydimethylsiloxane (PDMS) was prepared in the following manner. On a thin cover slip, Cu wires with ~ 50 μm diameters were arranged to form a cross and a PDMS solution (elastomer and curing agent in 10:1 volume ratio) was poured and baked at 70 °C for 4 hrs. After curing of the elastomer, the baked sample was cooled down to room temperature and the Cu wires and glass were removed. Ag microflower lifted with a carbon fiber was gently placed across the channel. 20 μL s of o-Phenylenediamine (OPD) and H_2O_2 were injected in the channels and the oxidation of OPD at the center produced azoaniline dye. The dye adsorbed on Ag microflower was detected by SERS.

7.3.7 FDTD simulations

2D FDTD simulations (Lumerical Solutions Ltd.) were carried out to calculate the near-field intensities around the nanoparticles present in the Ag microflower. A plane wave polarized light of wavelength 532 nm was used along the y-axis. In order to maximize field enhancement resolution, the mesh override region was kept at 0.5 nm. The simulation time was 100 fs.

7.4 Results and discussion

7.4.1 Characterization of AgToABr

The phase transferred organic phase (henceforth termed as Ag-ToABr) was separated using a micropipette. After the evaporation of solvent, the isolated solid precursor was characterized using IR spectroscopy, XRD and TGA (Fig. 7.1)

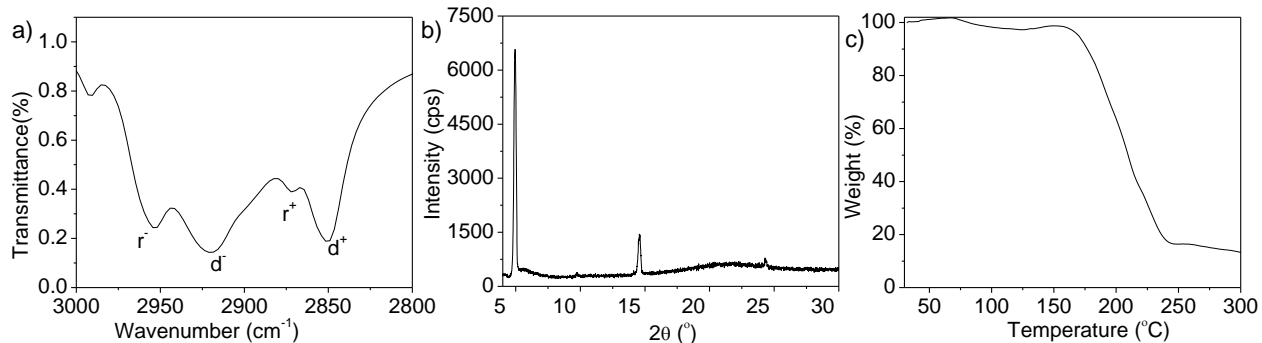


Figure 7.1 (a) IR spectrum, (b) XRD and (c) TGA of AgToABr.

As shown in thermo gravimetric analysis (TGA) plot (Fig. 7.1(c)), the decomposition of AgToABr starts at ~ 165 °C and completes at 230 °C. Weight loss occurs in two steps - region I ($\sim 3\%$) corresponding to solvent evaporation and regions II ($\sim 81.35\%$) corresponding to decomposition, and desorption of ToABr, ToA, chlorine, bromine. The AgBr residue is ~ 15.65 wt%.

$$\begin{aligned}
 \text{Molecular weight of ToABr} &= 546.79 \text{ g/mol} \\
 \text{Molecular weight of AgBr} &= 187.77 \text{ g/mol} \\
 \text{AgCl molecular weight} &= 143.32 \text{ g/mol} \\
 15.65 \text{ wt\%} = \text{AgBr} &= 187.77 \text{ g/mol} \\
 100 \text{ wt\%} = x &= 1199.8 (\sim 1200) \text{ g/mol} \\
 (\text{AgCl}_2)^- + \text{ToA}^+ + \text{ToABr} &= 178.92 + 466 + 546.79 = 1192 \approx 1200
 \end{aligned}$$

Hence, the empirically derived formula is $(\text{AgCl}_2)^-\text{ToA}^+\cdot\text{ToABr}$, which in a simplified way, is written as AgToABr that shows lamellar structure (fig. 7.1(b)).

7.4.2 Growth of Ag microflowers

Figure 7.2(a) is the schematic illustration of Ag microflower synthesis. Thermolysis of AgToABr at 250 °C led to the formation of pale yellow colored moieties on the substrate. The SEM image obtained from the substrate (Fig. 7.2(b)) showed star-like structures with 3 to 8 branches (majority with four branches), the overall size being around 50 - 100 μm . Under high magnification, one can see dendrimeric growth on the branches (Fig. 7.2(c)). The surface of the microflowers was smooth and nonporous (Fig. 7.2(d)). These structures are essentially AgBr crystallites (Fig. 7.2(i)) as revealed by the EDS analysis (Ag:Br, 55:45

at%). The crystalline nature of the obtained microflowers was confirmed by XRD and the peaks matched well with that of polycrystalline cubic AgBr (JCPDS No. 40784) (see Fig. 7.2(j)).

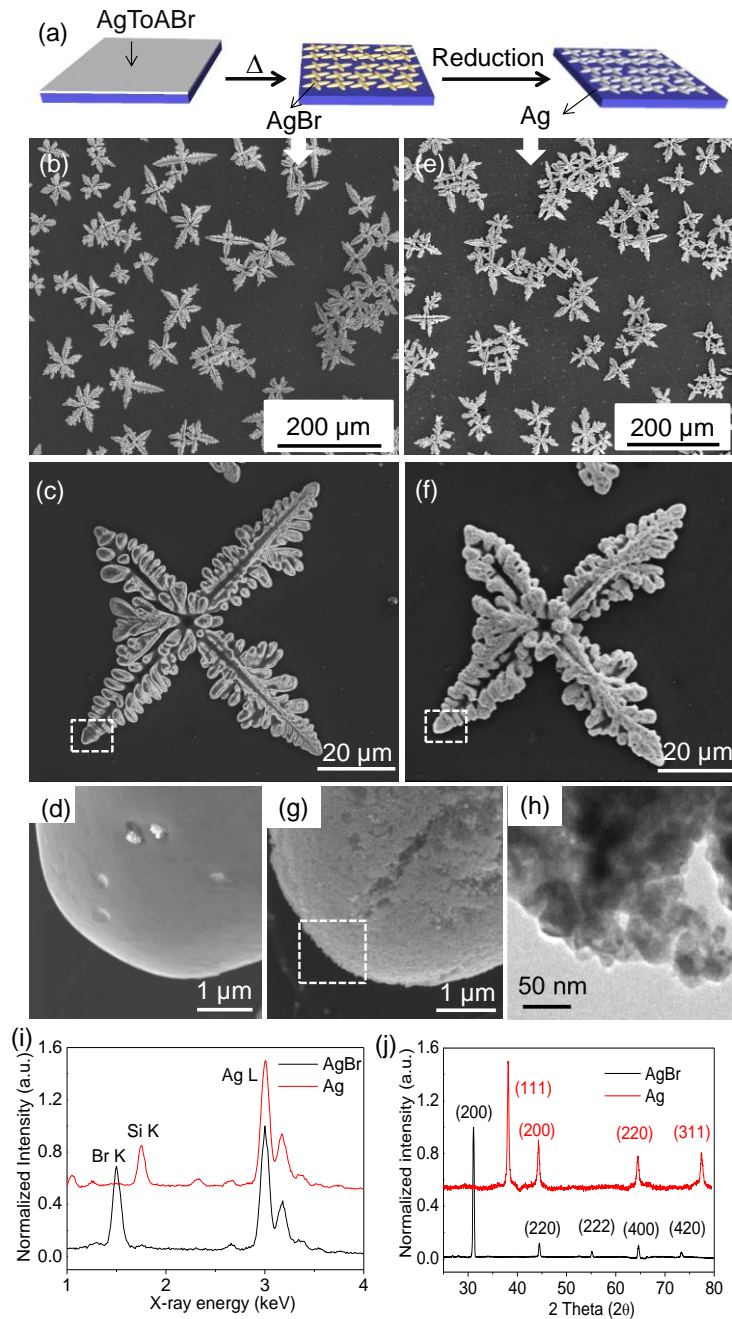


Figure 7.2 (a) Schematic illustrating the thermolysis of AgToABr leading to AgBr microflowers followed by NaBH₄ reduction to form Ag microflowers. FESEM images of (b-d) AgBr microflowers (as prepared) and (e-g) Ag microflowers (post NaBH₄ reduction) at

different magnifications. Inset is the magnified view of the marked area. (h) TEM image from the same region. (i) EDS spectra collected from a microflower before and after reduction. (j) XRD patterns of substrates contain AgBr and Ag flowers.

The reduction of AgBr was performed with 17 mM NaBH₄ solution resulting in the formation of Ag while maintaining the flower-like morphology (Fig. 7.2(e-f)). The flower structures formed were rough and porous (Fig. 7.2(g)) consisting of interconnected Ag nanoparticles of 25-40 nm as revealed by TEM images (Fig. 7.2(h)). Usually, reduction of metal salts with strong reducing agent like NaBH₄ induces porosity (9). The EDS spectrum shown in Fig. 7.2(i), confirmed the presence of Ag with no detectable trace of Br. Indeed, this synthetic procedure does not involve any capping agent and therefore the Ag surface is kept chemically accessible. The metallic Ag microflowers were found to be polycrystalline and the XRD pattern was found to match with that of polycrystalline Ag (JCPDS 4-0787) (see Fig. 7.2(j)).

A detailed investigation of the role of thermolysis temperature was carried out. Thermogravimetric analysis (TGA) shows that the decomposition of AgToABr takes place above 170 °C (Fig. 7.1). The reaction was performed at temperatures ranging from 200 to 240 °C. At lower thermolysis temperatures (200-210 °C), the formation of AgBr cubes was predominant and the size increased with temperature. While cube-like structures were observed at 200 °C (Fig. 7.3(a, f)), the cubes gained sharp edges at 210 °C (Figs. 7.3b and g). A higher temperature (220 °C) gave rise to a combination of distorted cubes and small microflowers as shown in Figs. 7.3(c) and (h). Complete microflower formation occurred at temperatures higher than 220 °C (see Figs. 7.3(d, e, i and j)) and with increasing temperature till 250 °C, the size of the AgBr microflowers also increased. It is therefore evident that the thermolysis temperature plays a vital role in tuning the morphology of AgBr crystals and the shape can be controlled and tuned from cube-like to microflowers. At temperatures higher than 250 °C, there was no observable change in the morphology of the AgBr microflowers. Importantly, as the microflowers are of several tens of μm in size, they can be easily addressed and manipulated under a common optical microscope.

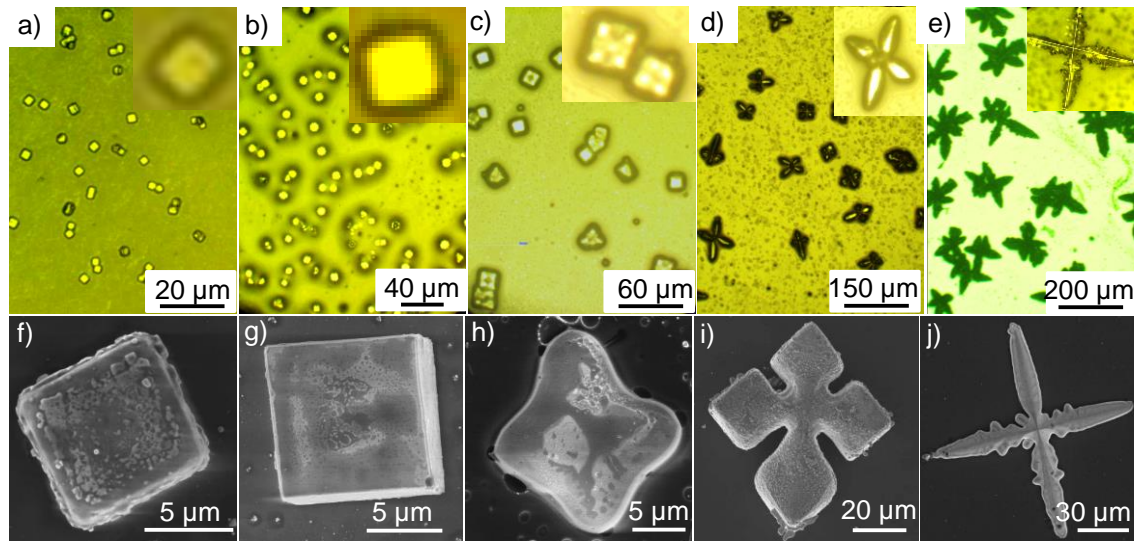


Figure 7.3 (a-e) Optical microscopy images of AgBr crystals prepared at different temperatures (200-240 °C) with magnified images in the insets. The images were recorded in the reflection mode by illuminating the substrate (n-Si(100)) with yellow light. The corresponding SEM images are shown in images f-j.

The growth process of AgBr microflower is indeed interesting. In order to monitor the intermediate stages associated with the growth of microflower, real time SEM imaging was carried out in situ, by employing a similar procedure. The deposited AgToABr formed a continuous film, whereas high magnification imaging showed fibril-like structure (Fig. 7.4(a, b)). Heating the film to 240 °C resulted in the formation of isolated drops due to the dewetting of the film (Fig. 7.4(c)). On decomposition of AgToABr, the drops gave rise to AgBr cubes with edge lengths of $\sim 2-3 \mu\text{m}$ (Fig. 7.4(d)). Subsequently, the corner regions protruded out (Fig. 7.4(e)) and gave rise to flower-like morphology (see Fig. 7.4(g)). The observed growth mechanism can be attributed to the different surface energies associated with the AgBr facets. The surface energy of (111), (110) and (100) planes of AgBr are 1.253, 0.561 and 0.495 J/m^2 respectively (28). Accordingly, {100} facets with lowest surface energy are favored to form a cube (see schematic in Fig. 7.4(d)). At elevated temperatures ($> 210 \text{ }^\circ\text{C}$), the surface energy of {110} may become more favorable leading to the interesting morphology observed. To our knowledge, this is the first time that such growth has been observed in the case of AgBr.

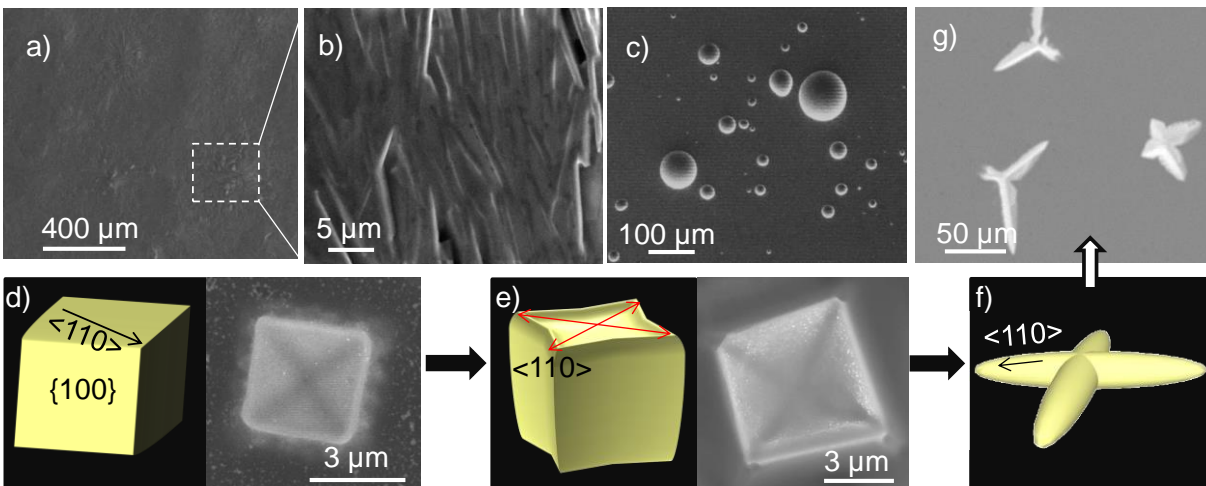


Figure 7.4 SEM images of (a-b) AgToABr film at different magnifications, (c) dewetting of AgToABr film on heating to 240 °C. SEM image of a AgBr microcrystals in the initial stage of thermolysis (240 °C), recorded in-situ. (e) The microcrystals in d after ~ 1 min. The crystallographic directions are indicated in the schematic shown alongside. This crystal was degraded with further e-beam exposure. (f) Schematic of a AgBr microcrystal which transformed into a microflower at the end of thermolysis corresponding to that shown in g.

7.4.3 Ag microflowers as SERS substrate

SERS Enhancement factor and wavelength independence

As Ag microflowers are free-standing and devoid of any surface capping agents, they present an interesting case for use in SERS, which is predominantly a surface phenomenon. The interconnected nanoparticles (Fig. 7.5i) host hotspots spread all over the microflower, which are regions of high electric field. Thus, these hotspots are expected to cause significant SERS enhancement. A representative FDTD calculation (Fig. 7.5(j)) reveals the presence of the hot spots located between adjacent nanoparticles. Thiophenol was chosen as an analyte, which chemisorbs on the Ag surface and is a non-resonant molecule. Raman spectrum of neat thiophenol on glass substrate is shown in Fig 7.5(b). The SERS spectra collected from a Ag microflower exposed to 1 mM thiophenol are shown in Figs 7.5(c) and (d), excited with green (532 nm) and red (632 nm) wavelengths, respectively.

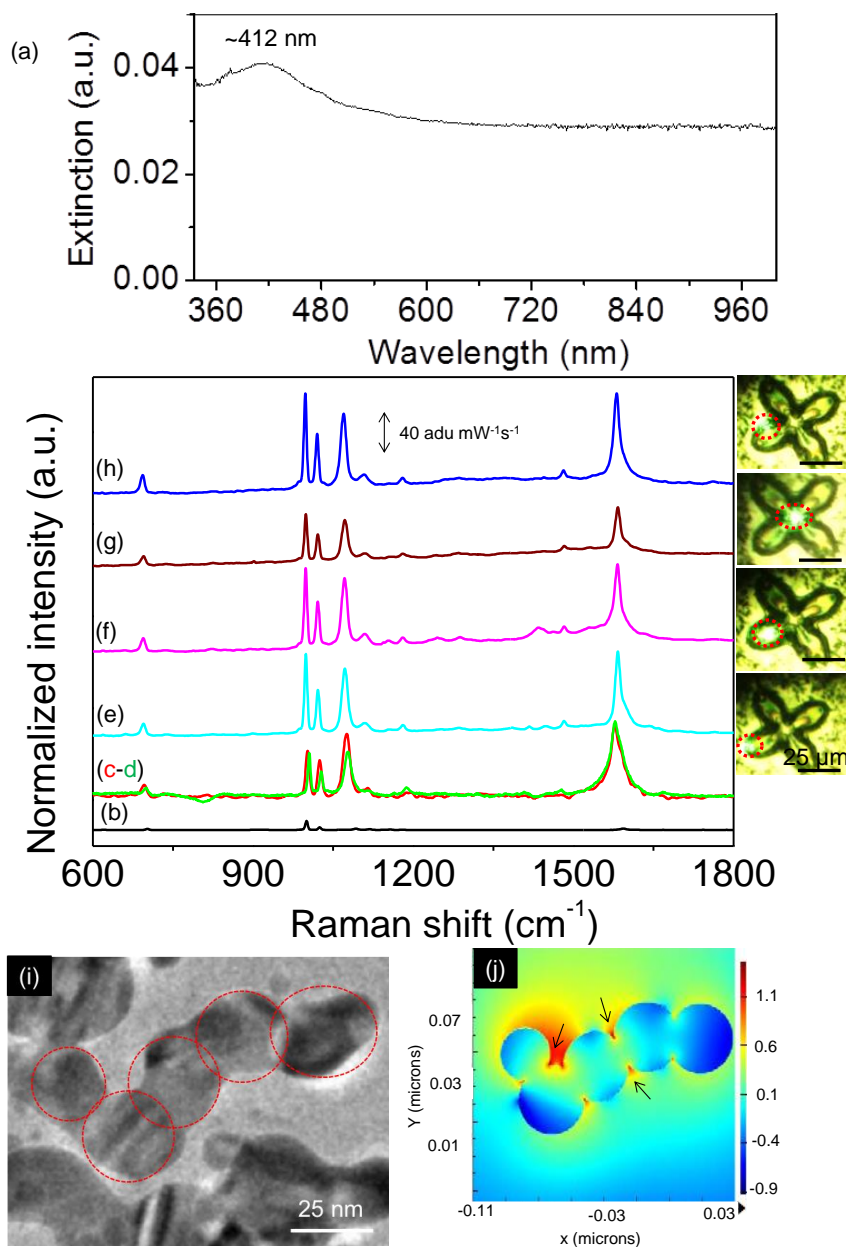


Figure 7.5 (a) Extinction spectrum of the Ag microflowers. (b) Raman spectrum of neat thiophenol placed on a glass substrate. SERS spectra of thiophenol (c, d) from a microflower excited with green (532 nm) and red (632.8 nm) lasers, respectively. Prior to measurements, the microflower was adsorbed with 1 mM thiophenol. (e-h) spectra collected from different regions of the microflower. Optical microscopy images of the microflower are shown on the right with the laser spot positions marked. All the spectra are normalized with reference to power of the laser and the accumulation time. The laser spot area of the Raman setup is approximately 4 μm². The spectra have been normalized to per mW of the

laser power and per second accumulation time. (i) TEM image of interconnected Ag nanoparticles in a microflower. (j) The near field intensity in the vicinity of Ag nanoparticles obtained by FDTD simulations. The Ag nanoparticles in FDTD simulations are representative of the nanoparticles highlighted in (i) with same dimensions. The hotspots (indicated by arrows) can be seen at the junctions of the nanoparticles, which have high electric field intensity.

The relative ratios of peaks at 1000 and 1578 cm^{-1} are 1.05 and 0.93 for red and green lasers respectively, both being nearly equal to 1. Therefore, the dependence on the exciting wavelength is nearly absent in the given range, which is also evident from the extinction spectrum shown in Fig 7.5(a). The spectrum exhibits clearly a peak around 412 nm which is due to the localized surface plasmon of Ag nanoparticles (consistent with the TEM images shown in Fig 7.2(h)). A broad band absorption is seen arising due to nanoparticle coupling⁹ in the microflower aggregation. This broad absorption enables one to perform SERS using different wavelengths, particularly suited to biomolecules.

SERS data were collected from four different places of a single microflower (see Fig. 7.5 (d-g)). The G factors calculated by the method of Yu et al. (29) for the 1578 cm^{-1} band collected from various parts of the microflower are all quite comparable- tip (1.4×10^7), center (8.1×10^7), arm centre (1.2×10^7) and arm edge (1.6×10^7). Indeed, there is a 6 to 7 fold increase in the enhancement at the center compared to other parts. It appears that the confluence of four lobes at the center of the microflower creates a favorable condition for maximum cumulative electromagnetic field intensity on the molecules adsorbed near the center of the microflower. This leads to the higher SERS activity at the center compared to the other parts. As an example of a molecule forming no specific chemical bond with Ag surface (and also non-resonant), SERS on 1,2,3-benzotriazole was done (see Fig. 7.6)

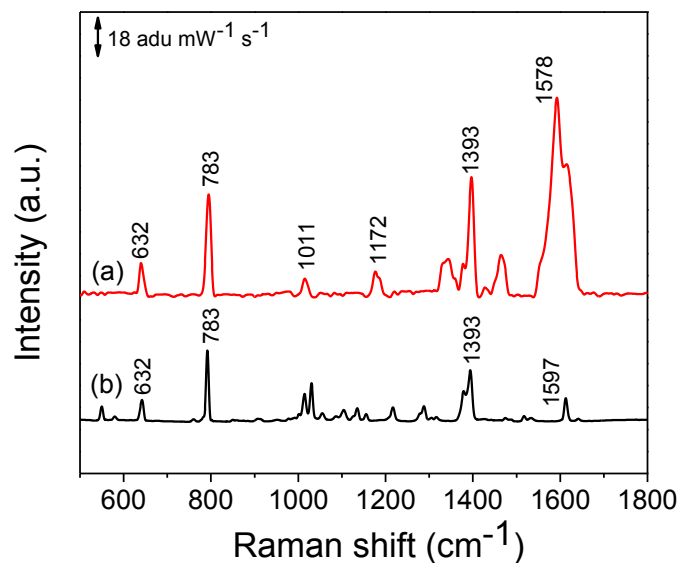


Figure 7.6 (a) SERS (1 μM) and (b) normal Raman spectra (bulk) of 1,2,3- benzotriazole.

In this case as well, enhancement factor of $\sim 10^6$ was obtained. With a resonant dye, R6G, much lower concentrations, down to attomolar could be detected (see Fig. 7.7).

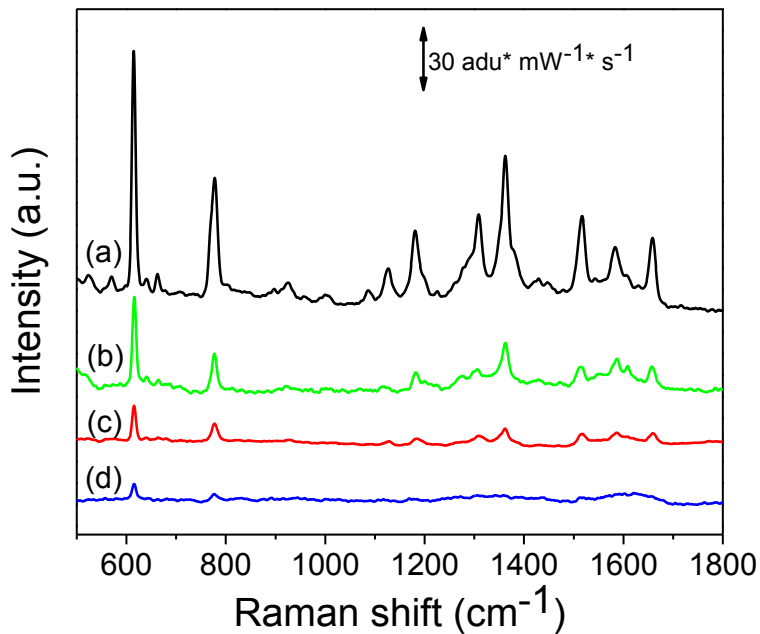


Figure 7.7 SERS of R6G solution of (a) 10^{-9} , (b) 10^{-12} , (c) 10^{-15} and (d) 10^{-18} M concentrations. In each experiment, 200 nL of the solution was used.

SERS of biomolecules

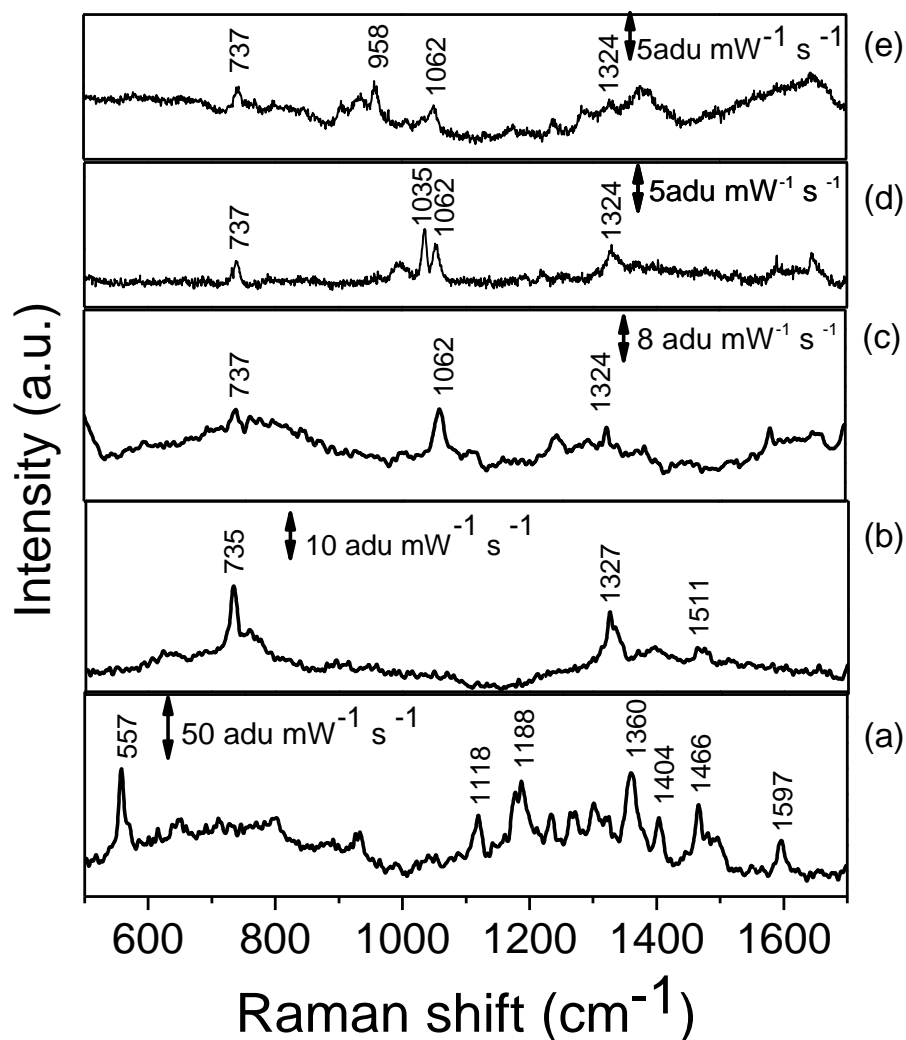


Figure 7.8 (a)-(c) SERS of Cy5 labeled oligonucleotide, label-free double stranded salmon sperm DNA and oligo A obtained from 1 ng/ μ L concentration. SERS of (d)-(e) oligo B and oligo C obtained from 1 pg/ μ L. The experiments were performed using 200 nL of solution.

Development of fast and cost effective methods for nucleic acid analysis is high in demand in biomedical research as well as in industry. The Ag microflowers explored for SERS detection of labeled and non-labeled single stranded oligonucleotides (< 60 base pairs) as well as of double stranded genomic DNA obtained from salmon sperm (~ 2000 base pairs).

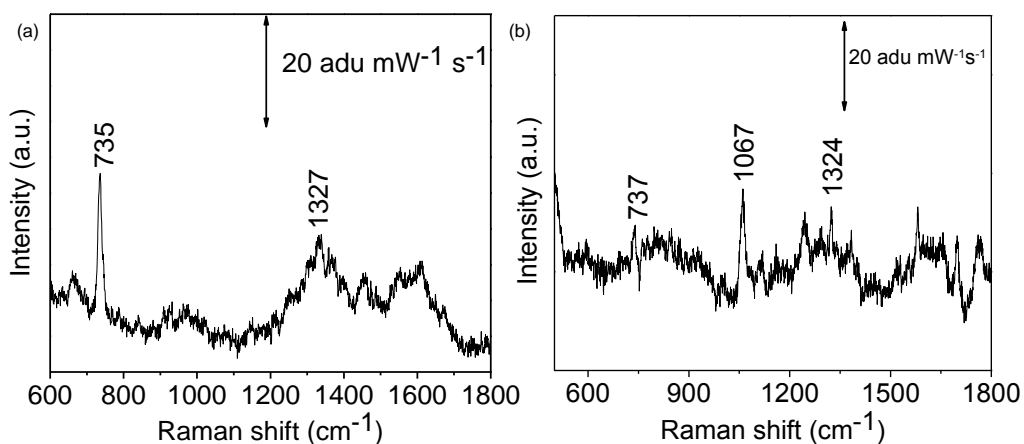


Figure 7.9 SERS of (a) salmon sperm DNA adsorbed from a solution of concentration, 0.75 nM. (b) single stranded oligonucleotide (oligo A). Solution of concentration, 67 nM.

Raman spectra obtained from these molecules are given in Fig. 7.8. The label-free double stranded (Fig. 7.8(b)) and label-free single stranded DNA (Fig. 7.8(c-e)) gives exhibit two major bands due to the ring breathing mode of adenine (30) around 737 and 735 cm⁻¹ in case of single and double stranded species, respectively. The 1324 and 1327 cm⁻¹ bands correspond to mixed in-plane stretching motions of the adenine ring (Figures 7.8b-e). Other bands arise mostly from bases namely guanine, cytosine and thymine with a phosphate backbone stretching band seen prominently in case of single stranded oligonucleotide at around 958 as well as at 1062 cm⁻¹. For Cy5 labeled oligonucleotide, the SERS spectrum is dominated by bands from the Cy5 molecule (Fig. 7.8a) (31). SERS obtained from relatively higher concentration of DNA (1 ppm, Figures 7.8b and c) were comparable to those obtained from low nM concentrations (Fig. 7.9). The SERS spectra of oligonucleotides with lower G base percentages (oligo B and C) and shorter length (oligo C) have been provided in Figures 7.8d and e. These spectra shows that the larger sizes and G percentages (greater propensity to form secondary structures) do not have significant effect on the SERS detection. The ability to detect the different nucleobase components of single and double stranded oligonucleotides presents an interesting prospect of using these substrates for direct, cost effective and label-free detection as the need for tagging the 3' or 5' end of the oligonucleotide with fluorophores, is eliminated.

SERS using low analyte volumes

Although SERS substrates exhibit high enhancement factors, the volume of analyte required for a single experiment is often quite large (\sim few μL of sub μM) (32-41). There have been efforts to localize the analyte volume to a spot without spreading as well as to minimize the drop size (8). The nanostructures are also functionalized in order to capture few desired molecules from the target solution resulting in higher sensitivity of detection (42). Even a drop of 200 nL made by a micropipette covers an area of around $\sim 1.2 \text{ mm}^2$ which is almost 10^6 times more than the area covered by the laser spot ($\sim 4 \mu\text{m}^2$). Further, the drop volume can cover several microflowers (~ 20) rather than being localized around a given microflower. Therefore, instead of pouring solution over the microflowers, a single microflower was picked using a carbon fiber and put in contact with a small drop of R6G solution (200 nL) for 5 min and Raman measurements were performed (Fig. 7.10a). This way, the manipulable nature of the SERS substrate was utilised. In another approach, the R6G solution transferred to the microflower surface by gently touching using a carbon fiber (Fig. 7.10b). By an estimate, $\sim 0.34 \text{ nL}$ of R6G solution was transferred to the Ag microflower. In both the cases, detectable SERS signals of the R6G molecules could be obtained. This is a fine example of using very low volumes of the analyte for SERS detection (Fig. 7.10c), a feature of particular significance in bio-detection as well as in industries using expensive chemicals.

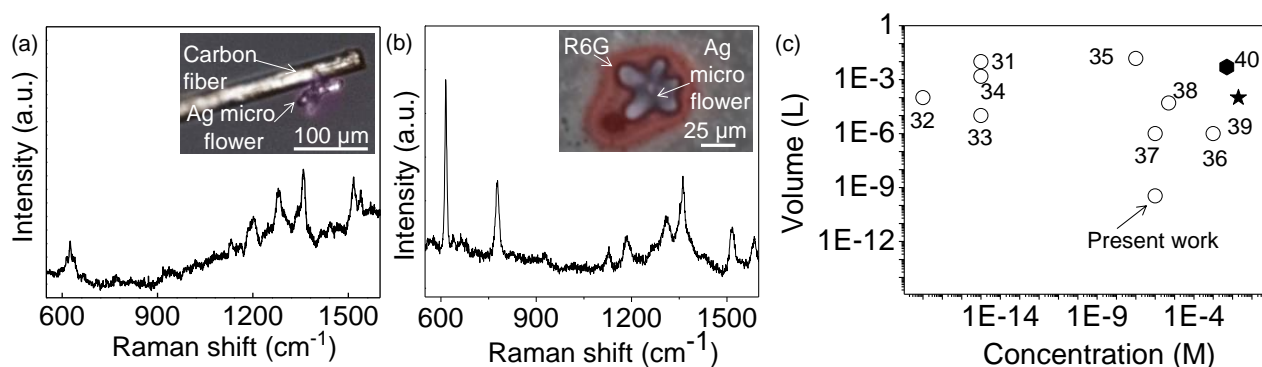


Figure 7.10 SERS spectra obtained after (a) dipping a single Ag microflower attached to carbon fiber in 200 nL of R6G solution and (b) drop coating of $\sim 0.35 \text{ nL}$ R6G solution on a single microflower. The concentration of R6G solutions used was $1 \mu\text{M}$. The optical

microscopy images of the microflowers used to obtain SERS spectra in (a) and (b) are shown in the inset. (c) Comparative values of concentrations and volumes of analytes mentioned in literature and the present work. Circles, filled hexagon and star represent

Reusability of Ag microflowers for SERS

Reusability of a SERS substrate is of foremost importance in making the technique commercially viable. There are only a few methods reported in the literature to make the substrates reusable, for example, heating the substrate at a higher temperature for removing the adsorbed organic moieties (43), illuminating with visible light for longer time (44) and UV ozone (UVO) treatment (45). Although these methods are efficient in rendering the substrate reusable over a few cycles (~ 5), there have been issues related to retaining the SERS activity, as heating at higher temperatures leads to the sintering of the nanostructures. Further, a solution treatment method was explored for recycling Ag microflowers (see Fig. 7.11).

Chloride ions interact efficiently with Ag(0) to form Ag/AgCl core-shell structure (46). Ag microflowers were treated with HCl to form few nm thick AgCl layer. Raman spectra collected from the Ag/AgCl microflower shows drastic quenching of the R6G peaks. A predominant peak at around 230 cm^{-1} confirmed the AgCl formation (Fig. 7.11c). In the next step, the AgCl layer was washed away with aqueous NH_3 solution (47) (see Fig. 7.11a) and correspondingly, the peak at 230 cm^{-1} disappeared, as also the remnant traces of the R6G (Fig. 7.11d). This was due to the removal of the AgCl layer which forms a soluble complex with ammonia which get removed during washing with ethanol and water. The reusability process commenced after R6G molecules were adsorbed on the same microflower followed by SERS data collection (Fig. 7.11b). The recycling process took 15 minutes in all. The G factor estimated using the 1654 cm^{-1} peak (1.4×10^8), compares well with the value obtained prior to AgCl formation (2×10^8). Thus, the first cycle of reusability of the microflower substrate was demonstrated. It is indeed interesting to note that the G-factors calculated for the successive 10 cycles varied in the range, 0.8 - 2 folds (Fig. 7.11e), which is acceptable. Through the recycling process, there were only

minimal changes in the overall structure of the microflower as revealed by the FESEM images, though the porosity increased slightly (Figs. 7.11(f, g)).

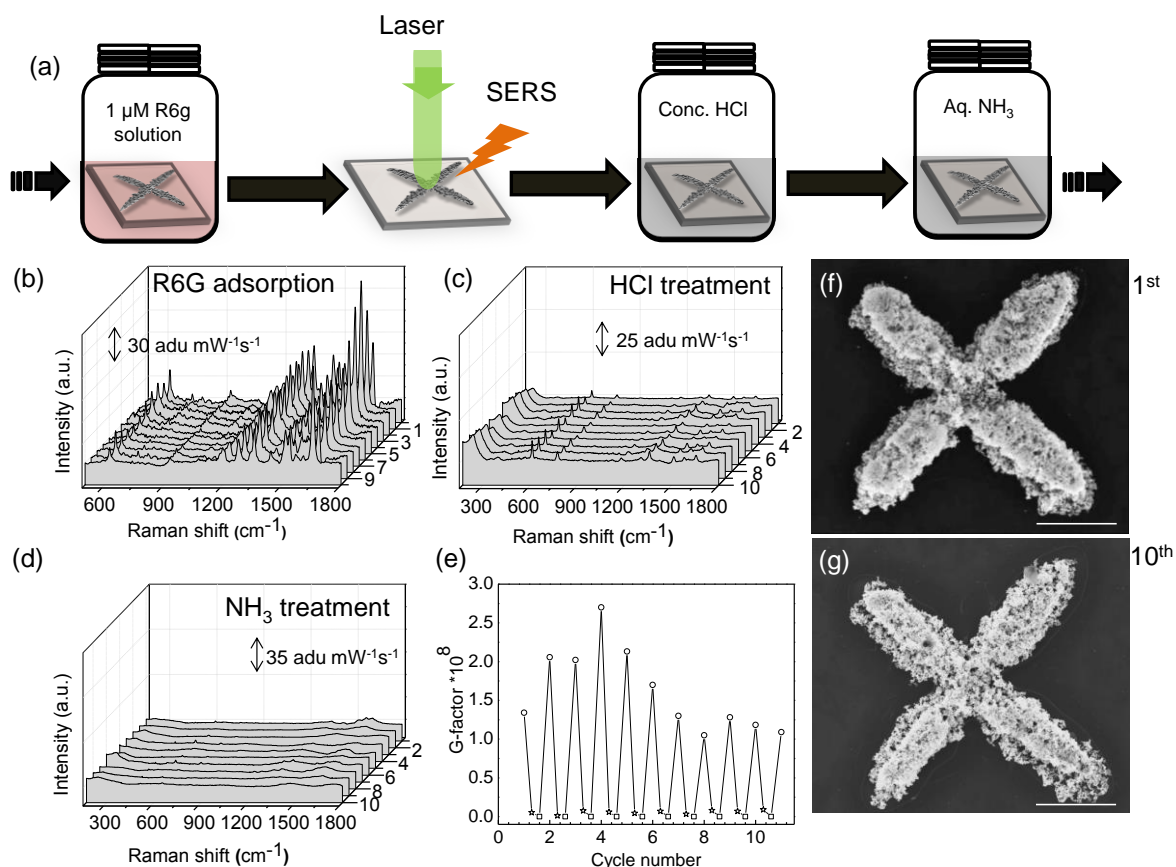


Figure 7.11 (a) Schematic illustrating reusability of Ag microflowers. The reusability is shown over 10 cycles. Spectra were taken after $1\mu\text{M}$ R6G adsorption (b), concentrated HCl treatment (c) and aqueous ammonia treatment (d) in each cycle and are numbered accordingly (1-10). (e) Variation in the intensity of the 1654 cm^{-1} band after each treatment step (R6G adsorption, circles; HCl treatment, star, Aq. Ammonia treatment, triangles). SEM images of the microflower after 1st (f) and 10th (g) cycles. Scale bar, $10\ \mu\text{m}$.

EDS and XRD measurements were performed on the microflowers which had undergone 10 cycles of washing (Fig. 7.12). In both EDS and XRD, the intensities of the Ag peaks are seen to decrease after recycling, but importantly no other feature due to impurities is seen. This goes well with the continued SERS activity from the microflower. What is noteworthy is that this is a fast recycling process taking only few minutes. A gap of few

hours did not seem to diminish the activity, as it is known that Ag nanostructures undergo slow oxidation under ambient conditions (48). In order to avoid surface oxidation influencing analyte adsorption, freshly reduced Ag microflowers from AgBr templates were commonly used. Importantly, the method of SERS substrate preparation presented in this study, allows one to crystallize and store AgBr microflowers for subsequent usage as Ag microflowers with one-step reduction process with practically no change in morphology. The above features make our microflower substrate quite unique among the literature reports.

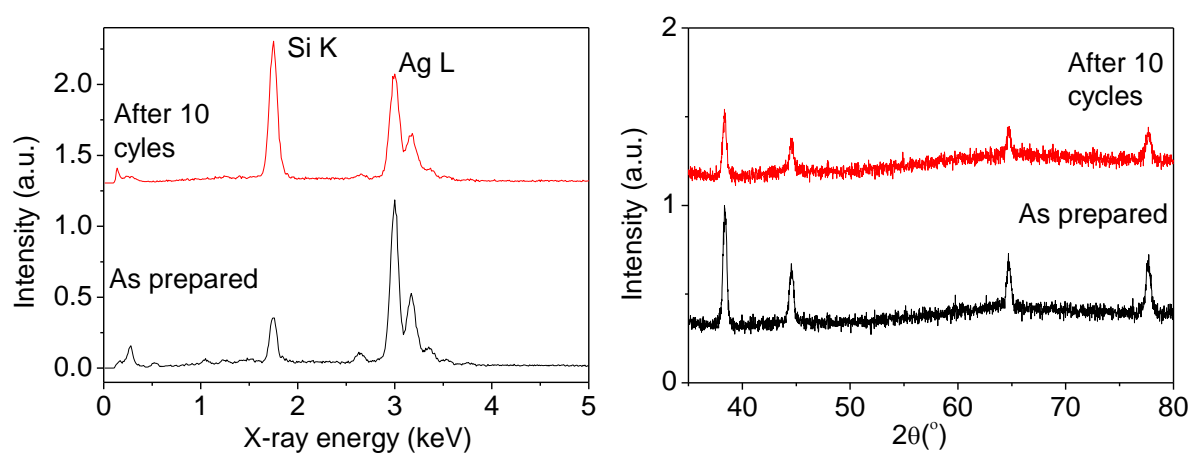


Figure 7.12 (a) EDS and (b) XRD of as-prepared Ag microflowers and after 10 cycles of washing.

Ag microflower in a microfluidic device

The oxidation–condensation reaction between hydrogen peroxide and o-Phenylenediamine (OPD) to form a fluorescent product is popularly used in biochemical assays like enzyme-linked immunosorbent assay (ELISA) (49) for detection of human immunodeficiency virus (HIV) infection. Here, as a proof-of-concept the reaction between OPD and hydrogen peroxide is demonstrated (which is the final step of ELISA) inside a microfluidic channel where a microflower was placed at the point of mixing of the reactants (Figures 7.13a and b) and the subsequently, the product formation was monitored through SERS (see chemical reaction in Fig. 7.13c). The formation of the azoaniline was monitored through the formation of the azo bond, characterized by the

appearance of the N=N stretching mode at around 1460 cm^{-1} (Fig. 7.13d) in SERS. This experiment shows the possibility of utilizing Ag microflowers in in-vitro immunoassays.

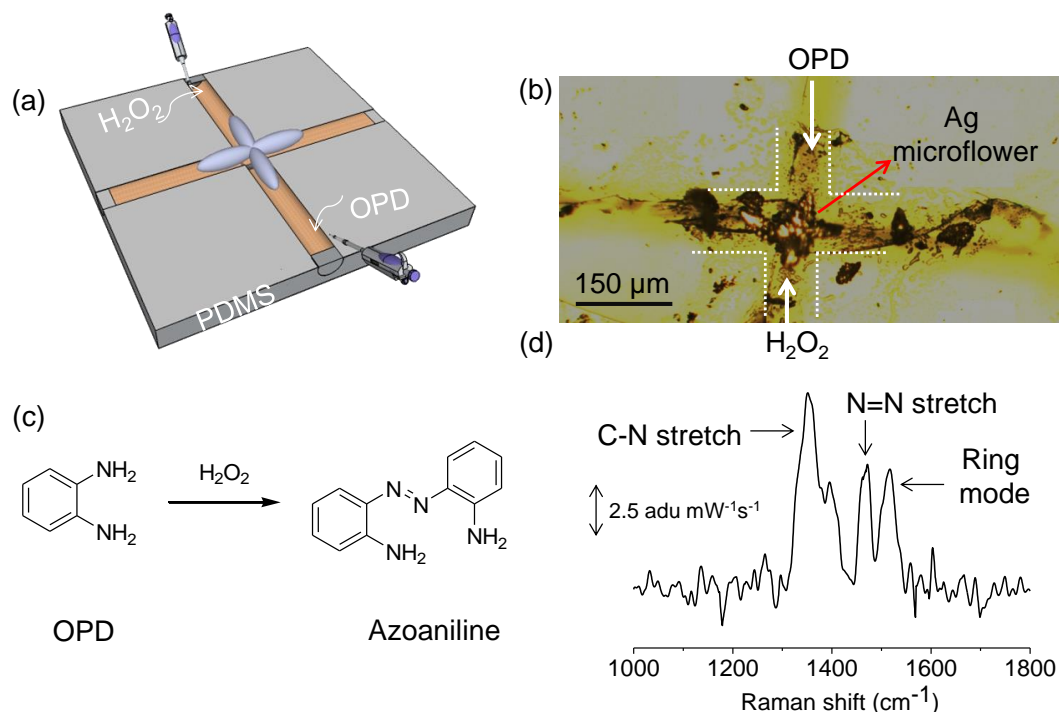


Figure 7.13 (a) Schematic of a microfluidic device with Ag microflower at the center. (b) Optical microscopy image of the Ag microflower placed firmly at the junction of orthogonal channels. (c) Chemical reaction of o-Phenylenediamine (OPD) with H_2O_2 leading to the formation of azoaniline dye (d) SERS of the dye adsorbed on the Ag microflower (accumulation time, 60 s). OPD and H_2O_2 , each $20\ \mu\text{L}$, were injected in the channels in opposite direction.

7.5 Conclusion

In conclusion, large Ag microflowers were fabricated ($\sim 50\text{--}100\ \mu\text{m}$) by thermal decomposition of a Ag-organic complex, followed by chemical reduction. Initially, cube-like AgBr crystallites nucleate and grow into star or flower-like geometry with time. The shape and size are dependent on the thermolysis temperature. This interesting growth aspect is being reported for the first time. Upon reduction using NaBH_4 , the crystallites developed into nanostructured Ag surface, which showed high SERS enhancement factor

($\sim 10^6$ - 10^8). The Ag microflowers were found to be novel in many ways. The nanostructuring of the surface was uniform all over which ensured reasonably uniform SERS enhancement factor. They could be used as SERS substrates repeatedly after appropriate washing steps, while the SERS enhancement remained practically similar. Their reusability and stability are truly remarkable. These are key factors in the fabrication of any commercial SERS detection platforms particularly for biomolecules as demonstrated in this study through SERS of various types of DNAs. Being large in size, the microflowers enabled easy handling for analyte adsorption and subsequent Raman measurements. Even nL volumes of nM concentrations were sufficient for detection. By positioning a single microflower in a microchannel and monitoring a reaction from the adsorbed product analyte, have demonstrated the usefulness of the microflowers in microfluidic applications.

References

1. S. Link, M. B. Mohamed, M. A. El-Sayed, *J Phys Chem B* **103**, 3073-3077 (1999).
2. P. L. Stiles, J. A. Dieringer, N. C. Shah, R. P. Van Duyne, *Annu Rev Anal Chem* **1**, 601-626 (2008).
3. K. A. Willets, R. P. Van Duyne, *Annu Rev Anal Chem* **58**, 267-297 (2007).
4. J. Kneipp, H. Kneipp, K. Kneipp, *Chem Soc Rev* **37**, 1052-1060 (2008).
5. C. Farcau, S. Astilean, *J Phys Chem C* **114**, 11717-11722 (2010).
6. H. Liu, L. Zhang, X. Lang, Y. Yamaguchi, H. Iwasaki, Y. Inouye, Q. Xue, M. Chen, *Sci. Rep.* **1**, 112 (2011).
7. X. Tang, W. Cai, L. Yang, J. Liu, *Nanoscale* **5**, 11193-11199 (2013).
8. F. De Angelis, F. Gentile, F. Mecarini, G. Das, M. Moretti, P. Candeloro, M. L. Coluccio, G. Cojoc, A. Accardo, C. Liberale, R. P. Zaccaria, G. Perozziello, L. Tirinato, A. Toma, G. Cuda, R. Cingolani, E. Di Fabrizio, *Nat Photonics* **5**, 683-688 (2011).
9. K. S. Krishna, C. S. S. Sandeep, R. Philip, M. Eswaramoorthy, *Acs Nano* **4**, 2681-2688 (2010).
10. R. Boyack, E. C. Le Ru, *Phys Chem Chem Phys* **11**, 7398-7405 (2009).
11. T. Abdallah, T. A. El-Brolosy, M. B. Mohamed, K. Easawi, S. Negm, H. Talaat, *J Raman Spectrosc* **43**, 1924-1930 (2012).

12. M. Rycenga, C. M. Cobley, J. Zeng, W. Y. Li, C. H. Moran, Q. Zhang, D. Qin, Y. N. Xia, *Chem Rev* **111**, 3669-3712 (2011).
13. Y. Yang, L. M. Xiong, J. L. Shi, M. Nogami, *Nanotechnology* **17**, 2670-2674 (2006).
14. D. Jana, A. Mandal, G. De, *ACS Appl Mater Inter* **4**, 3330-3334 (2012).
15. T. Bhuvana, G. U. Kulkarni, *Nanotechnology* **20**, (2009).
16. A. Garcia-Leis, J. V. Garcia-Ramos, S. Sanchez-Cortes, Silver Nanostars with High SERS Performance. *J Phys Chem C* **117**, 7791-7795 (2013).
17. H. B. Li, P. Liu, Y. Liang, J. Xiao, G. W. Yang, Super-SERS-active and highly effective antimicrobial Ag nanodendrites. *Nanoscale* **4**, 5082-5091 (2012).
18. G. Mettela, R. Boya, D. Singh, G. V. P. Kumar, G. U. Kulkarni, *Sci. Rep.* **3**, 1793 (2013).
19. T. Bhuvana, G. V. P. Kumar, G. U. Kulkarni, C. Narayana, *J Phys Chem C* **111**, 6700-6705 (2007).
20. B. K. Jena, B. K. Mishra, S. Bohidar, *J Phys Chem C* **113**, 14753-14758 (2009).
21. J. Li, J. Han, T. Xu, C. Guo, X. Bu, H. Zhang, L. Wang, H. Sun, B. Yang, *Langmuir* **29**, 7102-7110 (2013).
22. P. Xu, N. H. Mack, S.-H. Jeon, S. K. Doorn, X. Han, H.-L. Wang, *Langmuir* **26**, 8882-8886 (2010).
23. Y. Xia, Y. Xiong, B. Lim, S. E. Skrabalak, *Angew Chem Int Edit* **48**, 60-103 (2009).
24. J. Kumar, K. G. Thomas, *J Phys Chem Lett* **2**, 610-615 (2011).
25. Z. Huang, G. Meng, Q. Huang, B. Chen, C. Zhu, Z. Zhang, *J Raman Spectrosc* **44**, 240-246 (2013).
26. T. Bhuvana, G. U. Kulkarni, *Small* **4**, 670-676 (2008).
27. G. V. P. Kumar, C. Narayana, *Curr Sci* **93**, 778-781 (2007).
28. H. Wang, J. Gao, T. Guo, R. Wang, L. Guo, Y. Liu, J. Li, *Chem Commun* **48**, 275-277 (2012).
29. H.-Z. Yu, J. Zhang, H.-L. Zhang, Z.-F. Liu, *Langmuir* **15**, 16-19 (1999).
30. A. Barhoumi, D. Zhang, F. Tam, N. J. Halas, *J Am Chem Soc* **130**, 5523-5529 (2008).
31. W. Leng, A. A. Yasseri, S. Sharma, Z. Li, H. Y. Woo, D. Vak, G. C. Bazan, A. M. Kelley, *Anal Chem* **78**, 6279-6282 (2006).
32. Y. Q. Wang, S. Ma, Q. Q. Yang, X. J. Li, *Appl Surf Sci* **258**, 5881-5885 (2012).

33. Q. Li, Y. Du, X. Wang, P. Cao, T. Sui, Y. Xu, J. Geng, *J Raman Spectrosc* **44**, 1004-1009 (2013).
34. S. Yang, P. J. Hricko, P.-H. Huang, S. Li, Y. Zhao, Y. Xie, F. Guo, L. Wang, T. J. Huang, *J Mater Chem C* **2**, 542-547 (2014).
35. C. Zhu, G. Meng, Q. Huang, Z. Zhang, Q. Xu, G. Liu, Z. Huang, Z. Chu, *Chem Commun* **47**, 2709-2711 (2011).
36. X. Liu, F. Li, Y. Wang, H. Jin, H. Wang, Z. Li, *Mater Lett* **94**, 19-22 (2013).
37. L. Škantárová, A. Oriňák, R. Oriňáková, M. Jerigová, M. Stupavská, D. Velič, *Surf Interface Anal* **45**, 1266-1272 (2013).
38. W. W. Yu, I. M. White, *Analyst* **137**, 1168-1173 (2012).
39. B. Dong, L. Liu, H. Xu, M. Sun, *J Raman Spectrosc* **41**, 719-720 (2010).
40. W. Wei, S. Li, J. E. Millstone, M. J. Banholzer, X. Chen, X. Xu, G. C. Schatz, C. A. Mirkin, *Angew Chem Int Edit* **48**, 4210-4212 (2009).
41. P. H. C. Camargo, L. Au, M. Rycenga, W. Li, Y. Xia, *Chem Phys Lett* **484**, 304-308 (2010).
42. M. H. Harpster, H. Zhang, A. K. Sankara-Warrier, B. H. Ray, T. R. Ward, J. P. Kollmar, K. T. Carron, J. O. Mecham, R. C. Corcoran, W. C. Wilson, P. A. Johnson, *Biosens Bioelectron* **25**, 674-681 (2009).
43. P. R. Sajanlal, T. Pradeep, *Nanoscale* **4**, 3427-3437 (2012).
44. V. Kiran, S. Sampath, *ACS Appl Mater Inter* **4**, 3818-3828 (2012).
45. T. Siegfried, M. Kind, A. Terfort, O. J. F. Martin, M. Zharnikov, N. Ballav, H. Sigg, *J Raman Spectrosc* **44**, 170-175 (2013).
46. C. Xu, Y. Yuan, A. Cui, R. Yuan, *J Mater Sci* **48**, 967-973 (2013).
47. M. A. Maurer-Jones, M. P. S. Mousavi, L. D. Chen, P. Buhlmann, C. L. Haynes, *Chem Sci* **4**, 2564-2572 (2013).
48. G. Baraldi, M. Carrada, J. Toudert, F. J. Ferrer, A. Arbouet, V. Paillard, J. Gonzalo, *J Phys Chem C* **117**, 9431-9439 (2013).
49. J. E. Butler, *J Immunoassay* **21**, 165-209 (2000).

Chapter 8

Summary and outlook

Producing unusual morphologies and crystal structures from single source metal organic precursors is the essence of the thesis. Various Au and Ag micro-structures of unusual shapes have been synthesized and characterized using electron microscope and XRD techniques. The obtained microstructures are found to crystallize into unconventional lattice types exhibiting interesting optical properties.

The chemistry of metal organic complexes is a field by itself. The complexes used in this study to prepare metal nano/microcrystallites may as well be employed for synthesizing semiconducting materials such as nitrides and sulfides. These can also be used as a metal source to fabricate plasmonic structures with the aid of lithography techniques.

Introduction to the thesis is given in **Chapter 1** and details of characterization techniques in **chapter 2**. **Chapter 3** deals with the fabrication of unusual shaped Au microcrystallites covered with roughened surfaces. Due to well defined corrugations, these crystallites can exhibit interesting optical properties such SERS and nano-focusing phenomenon. Besides optical studies, these microstructures are suitable for single particle catalytic studies also. **Chapter 4** discussed the Cu epitaxial deposition on Au microcrystallites. Due to high reactivity, Cu can be galvanically replaced with noble metals such as Au, Ag, Pt and Pd on Au microcrystallites. The single crystalline Au microcrystallites are more ideal systems to create interesting plasmonic structures of various dimensions. The extended Au(111) and Au(100) surfaces are indeed interesting to understand the *herringbone* surface reconstruction. **Chapters 5 and 6** involved the synthesis of penta-twinned Au bipyramids. Interestingly, Au bipyramids prepared at ~ 220 °C host unusual crystal structure such as BCT and BCO. So far, size and shape dependent catalytic, magnetic, electrical and optical properties of FCC Au are known. It is worthy to study the crystal structure dependent properties of Au nano/microcrystallites. Structural changes at high pressures may be interest to pursue. Synthesis of nanocrystalline Ag microflowers is reported in **Chapter 7**. Since these crystallites are free of capping agents, both positive and negative charged analytes could be detected. As these crystallites require low volumes of analytes for the detection,

microflowes can be effectively used in bio applications and also to monitor product formation in synthetic organic chemistry reactions.

1. **Mettela, G.**, Boya, R., Singh, D., Kumar, G.V.P. & Kulkarni, G.U. Highly tapered pentagonal bipyramidal Au microcrystals with high index faceted corrugation: Synthesis and optical properties. *Sci. Rep.*3, 1793; DOI:10.1038/srep01793 (2013).
2. **Mettela, G.**, Siddhanta, S., Narayana. C., & Kulkarni, G.U. Nanocrystalline Ag microflowers as versatile SERS platform. *Nanoscale*, 2014,6, 7480
3. **Mettela, G.**, Bhogra, M., Waghmare, UV., & Kulkarni, G.U. Ambient Stable Tetragonal and Orthorhombic Phases in Penta-Twinned Bipyramidal Au Microcrystals. *J. Am. Chem. Soc.*, 2015, 137, 3024.
4. **Mettela, G.**, & Kulkarni, G.U. Facet Selective Etching of Au Microcrystallites (*Nano Res*, DOI 10.1007/s12274-015-0797-8).
5. **Mettela, G.**, & Kulkarni, G.U. Site selective Cu deposition on Au microcrystallites (under submission).
6. **Mettela, G.**, Kulkarni, G.U. Optimized synthetic conditions to enrich the non-FCC phases; Crystal structure controlled Cu deposition on Au bipyramids (Under Preparation).
7. **Mettela, G.**,* Gupta. R.,* Siddhanta, S.,* Chakraborty. S., Narayana. C., and Kulkarni, G. U. Solution Processed Nanomanufacturing of SERS Substrates with Random Ag Nanoholes Exhibiting Uniformly High Enhancement Factor (Under submission).

* Equally contributed
